Astronomy & Astrophysics manuscript no. dggc-final
April 6, 2018
©ESO 2018

Gaia Data Release 2: The kinematics of globular clusters and dwarf galaxies around the Milky Way

Gaia Collaboration, A. Helmi[1], F. van Leeuwen[2], P.J. McMillan[3], D. Massari[1], T. Antoja[4,5], A.C. Robin[6], L. Lindegren[3], U. Bastian[7], F. Arenou[8], C. Babusiaux[8,9], M. Biermann[7], M.A. Breddels[1], D. Hobbs[3], C. Jordi[5], E. Pancino[10,11], C. Reylé[6], J. Veljanoski[1], A.G.A. Brown[12], A. Vallenari[13], T. Prusti[4], J.H.J. de Bruijne[4], C.A.L. Bailer-Jones[14], D.W. Evans[2], L. Eyer[15], F. Jansen[16], S.A. Klioner[17], U. Lammers[18], X. Luri[5], F. Mignard[19], C. Panem[20], D. Pourbaix[21,22], S. Randich[10], P. Sartoretti[8], H.I. Siddiqui[23], C. Soubiran[24], N.A. Walton[2], M. Cropper[25], R. Drimmel[26], D. Katz[8], M.G. Lattanzi[26], J. Bakker[18], C. Cacciari[27], J. Castañeda[5], L. Chaoul[20], N. Cheek[28], F. De Angeli[2], C. Fabricius[5], R. Guerra[18], B. Holl[15], E. Masana[5], R. Messineo[29], N. Mowlavi[15], K. Nienartowicz[30], P. Panuzzo[8], J. Portell[5], M. Riello[2], G.M. Seabroke[25], P. Tanga[19], F. Thévenin[19], G. Gracia-Abril[31,7], G. Comoretto[23], M. Garcia-Reinaldos[18], D. Teyssier[23], M. Altmann[7,32], R. Andrae[14], M. Audard[15], I. Bellas-Velidis[33], K. Benson[25], J. Berthier[34], R. Blomme[35], P. Burgess[2], G. Busso[2], B. Carry[19,34], A. Cellino[26], G. Clementini[27], M. Clotet[5], O. Creevey[19,36], M. Davidson[37], J. De Ridder[38], L. Delchambre[39], A. Dell'Oro[10], C. Ducourant[24], J. Fernández-Hernández[40], M. Fouesneau[14], Y. Frémat[35], L. Galluccio[19], M. García-Torres[41], J. González-Núñez[28,42], J.J. González-Vidal[5], E. Gosset[39,22], L.P. Guy[30,43], J.-L. Halbwachs[44], N.C. Hambly[37], D.L. Harrison[2,45], J. Hernández[18], D. Hestroffer[34], S.T. Hodgkin[2], A. Hutton[46], G. Jasniewicz[47], A. Jean-Antoine-Piccolo[20], S. Jordan[7], A.J. Korn[48], A. Krone-Martins[49], A.C. Lanzafame[50,51], T. Lebzelter[52], W. Löffler[7], M. Manteiga[53,54], P.M. Marrese[55,11], J.M. Martín-Fleitas[46], A. Moitinho[49], A. Mora[46], K. Muinonen[56,57], J. Osinde[58], T. Pauwels[35], J.-M. Petit[6], A. Recio-Blanco[19], P.J. Richards[59], L. Rimoldini[30], L.M. Sarro[60], C. Siopis[21], M. Smith[25], A. Sozzetti[26], M. Süveges[14], J. Torra[5], W. van Reeven[46], U. Abbas[26], A. Abreu Aramburu[61], S. Accart[62], C. Aerts[38,63], G. Altavilla[55,11,27], M.A. Álvarez[53], R. Alvarez[18], J. Alves[52], R.I. Anderson[64,15], A.H. Andrei[65,66,32], E. Anglada Varela[40], E. Antiche[5], B. Arcay[53], T.L. Astraatmadja[14,67], N. Bach[46], S.G. Baker[25], L. Balaguer-Núñez[5], P. Balm[23], C. Barache[32], C. Barata[49], D. Barbato[68,26], F. Barblan[15], P.S. Barklem[48], D. Barrado[69], M. Barros[49], M.A. Barstow[70], S. Bartholomé Muñoz[5], J.-L. Bassilana[62], U. Becciani[51], M. Bellazzini[27], A. Berihuete[71], S. Bertone[26,32,72], L. Bianchi[73], O. Bienaymé[44], S. Blanco-Cuaresma[15,24,74], T. Boch[44], C. Boeche[13], A. Bombrun[75], R. Borrachero[5], D. Bossini[13], S. Bouquillon[32], G. Bourda[24], A. Bragaglia[27], L. Bramante[29], A. Bressan[76], N. Brouillet[24], T. Brüsemeister[7], E. Brugaletta[51], B. Bucciarelli[26], A. Burlacu[20], D. Busonero[26], A.G. Butkevich[17], R. Buzzi[26], E. Caffau[8], R. Cancelliere[77], G. Cannizzaro[78,63], T. Cantat-Gaudin[13,5], R. Carballo[79], T. Carlucci[32], J.M. Carrasco[5], L. Casamiquela[5], M. Castellani[55], A. Castro-Ginard[5], P. Charlot[24], L. Chemin[80], A. Chiavassa[19], G. Cocozza[27], G. Costigan[12], S. Cowell[2], F. Crifo[8], M. Crosta[26], C. Crowley[75], J. Cuypers[†35], C. Dafonte[53], Y. Damerdji[39,81], A. Dapergolas[33], P. David[34], M. David[82], P. de Laverny[19], F. De Luise[83], R. De March[29], D. de Martino[84], R. de Souza[85], A. de Torres[75], J. Debosscher[38], E. del Pozo[46], M. Delbo[19], A. Delgado[2], H.E. Delgado[60], P. Di Matteo[8], S. Diakite[6], C. Diener[2], E. Distefano[51], C. Dolding[25], P. Drazinos[86], J. Durán[58], B. Edvardsson[48], H. Enke[87], K. Eriksson[48], P. Esquej[88], G. Eynard Bontemps[20], C. Fabre[89], M. Fabrizio[55,11], S. Faigler[90], A.J. Falcão[91], M. Farràs Casas[5], L. Federici[27], G. Fedorets[56], P. Fernique[44], F. Figueras[5], F. Filippi[29], K. Findeisen[8], A. Fonti[29], E. Fraile[88], M. Fraser[2,92], B. Frézouls[20], M. Gai[26], S. Galleti[27], D. Garabato[53], F. García-Sedano[60], A. Garofalo[93,27], N. Garralda[5], A. Gavel[48], P. Gavras[8,33,86], J. Gerssen[87], R. Geyer[17], P. Giacobbe[26], G. Gilmore[2], S. Girona[94], G. Giuffrida[11,55], F. Glass[15], M. Gomes[49], M. Granvik[56,95], A. Gueguen[8,96], A. Guerrier[62], J. Guiraud[20], R. Gutiérrez-Sánchez[23], R. Haigron[8], D. Hatzidimitriou[86,33], M. Hauser[7,14], M. Haywood[8], U. Heiter[48], J. Heu[8], T. Hilger[17], W. Hofmann[7], G. Holland[2], H.E. Huckle[25], A. Hypki[12,97], V. Icardi[29], K. Janßen[87], G. Jevardat de Fombelle[30], P.G. Jonker[78,63], Á.L. Juhász[98,99], F. Julbe[5], A. Karampelas[86,100], A. Kewley[2], J. Klar[87], A. Kochoska[101,102], R. Kohley[18], K. Kolenberg[103,38,74], M. Kontizas[86], E. Kontizas[33], S.E. Koposov[2,104], G. Kordopatis[19], Z. Kostrzewa-Rutkowska[78,63], P. Koubsky[105], S. Lambert[32], A.F. Lanza[51], Y. Lasne[62], J.-B. Lavigne[62], Y. Le Fustec[106], C. Le Poncin-Lafitte[32], Y. Lebreton[8,107], S. Leccia[84], N. Leclerc[8], I. Lecoeur-Taibi[30], H. Lenhardt[7], F. Leroux[62], S. Liao[26,108,109], E. Licata[73], H.E.P. Lindstrøm[110,111], T.A. Lister[112], E. Livanou[86], A. Lobel[35], M. López[69], S. Managau[62], R.G. Mann[37], G. Mantelet[7], O. Marchal[8], J.M. Marchant[113], M. Marconi[84], S. Marinoni[55,11], G. Marschalkó[98,114], D.J. Marshall[115], M. Martino[29], G. Marton[98], N. Mary[62], G. Matijevič[87], T. Mazeh[90], S. Messina[51], D. Michalik[3], N.R. Millar[2], D. Molina[5], R. Molinaro[84], L.

Molnár[98], P. Montegriffo[27], R. Mor[5], R. Morbidelli[26], T. Morel[39], D. Morris[37], A.F. Mulone[29], T. Muraveva[27], I. Musella[84], G. Nelemans[63,38], L. Nicastro[27], L. Noval[62], W. O'Mullane[18,43], C. Ordénovic[19], D. Ordóñez-Blanco[30], P. Osborne[2], C. Pagani[70], I. Pagano[51], F. Pailler[20], H. Palacin[62], L. Palaversa[2,15], A. Panahi[90], M. Pawlak[116,117], A.M. Piersimoni[83], F.-X. Pineau[44], E. Plachy[98], G. Plum[8], E. Poggio[68,26], E. Poujoulet[118], A. Prša[102], L. Pulone[55], E. Racero[28], S. Ragaini[27], N. Rambaux[34], M. Ramos-Lerate[119], S. Regibo[38], F. Riclet[20], V. Ripepi[84], A. Riva[26], A. Rivard[62], G. Rixon[2], T. Roegiers[120], M. Roelens[15], M. Romero-Gómez[5], N. Rowell[37], F. Royer[8], L. Ruiz-Dern[8], G. Sadowski[21], T. Sagristà Sellés[7], J. Sahlmann[18,121], J. Salgado[122], E. Salguero[40], N. Sanna[10], T. Santana-Ros[97], M. Sarasso[26], H. Savietto[123], M. Schultheis[19], E. Sciacca[51], M. Segol[124], J.C. Segovia[28], D. Ségransan[15], I-C. Shih[8], L. Siltala[56,125], A.F. Silva[49], R.L. Smart[26], K.W. Smith[14], E. Solano[69,126], F. Solitro[29], R. Sordo[13], S. Soria Nieto[5], J. Souchay[32], A. Spagna[26], F. Spoto[19,34], U. Stampa[7], I.A. Steele[113], H. Steidelmüller[17], C.A. Stephenson[23], H. Stoev[127], F.F. Suess[2], J. Surdej[39], L. Szabados[98], E. Szegedi-Elek[98], D. Tapiador[128,129], F. Taris[32], G. Tauran[62], M.B. Taylor[130], R. Teixeira[85], D. Terrett[59], P. Teyssandier[32], W. Thuillot[34], A. Titarenko[19], F. Torra Clotet[131], C. Turon[8], A. Ulla[132], E. Utrilla[46], S. Uzzi[29], M. Vaillant[62], G. Valentini[83], V. Valette[20], A. van Elteren[12], E. Van Hemelryck[35], M. van Leeuwen[2], M. Vaschetto[29], A. Vecchiato[26], Y. Viala[8], D. Vicente[94], S. Vogt[120], C. von Essen[133], H. Voss[5], V. Votruba[105], S. Voutsinas[37], G. Walmsley[20], M. Weiler[5], O. Wertz[134], T. Wevers[2,63], Ł. Wyrzykowski[2,116], A. Yoldas[2], M. Žerjal[101,135], H. Ziaeepour[6], J. Zorec[136], S. Zschocke[17], S. Zucker[137], C. Zurbach[47], and T. Zwitter[101]

[1] Kapteyn Astronomical Institute, University of Groningen, Landleven 12, 9747 AD Groningen, The Netherlands
[2] Institute of Astronomy, University of Cambridge, Madingley Road, Cambridge CB3 0HA, United Kingdom
[3] Lund Observatory, Department of Astronomy and Theoretical Physics, Lund University, Box 43, 22100 Lund, Sweden
[4] Science Support Office, Directorate of Science, European Space Research and Technology Centre (ESA/ESTEC), Keplerlaan 1, 2201AZ, Noordwijk, The Netherlands
[5] Institut de Ciències del Cosmos, Universitat de Barcelona (IEEC-UB), Martí i Franquès 1, 08028 Barcelona, Spain
[6] Institut UTINAM UMR6213, CNRS, OSU THETA Franche-Comté Bourgogne, Université Bourgogne Franche-Comté, 25000 Besançon, France
[7] Astronomisches Rechen-Institut, Zentrum für Astronomie der Universität Heidelberg, Mönchhofstr. 12-14, 69120 Heidelberg, Germany
[8] GEPI, Observatoire de Paris, Université PSL, CNRS, 5 Place Jules Janssen, 92190 Meudon, France
[9] Univ. Grenoble Alpes, CNRS, IPAG, 38000 Grenoble, France
[10] INAF - Osservatorio Astrofisico di Arcetri, Largo Enrico Fermi 5, 50125 Firenze, Italy
[11] Space Science Data Center - ASI, Via del Politecnico SNC, 00133 Roma, Italy
[12] Leiden Observatory, Leiden University, Niels Bohrweg 2, 2333 CA Leiden, The Netherlands
[13] INAF - Osservatorio astronomico di Padova, Vicolo Osservatorio 5, 35122 Padova, Italy
[14] Max Planck Institute for Astronomy, Königstuhl 17, 69117 Heidelberg, Germany
[15] Department of Astronomy, University of Geneva, Chemin des Maillettes 51, 1290 Versoix, Switzerland
[16] Mission Operations Division, Operations Department, Directorate of Science, European Space Research and Technology Centre (ESA/ESTEC), Keplerlaan 1, 2201 AZ, Noordwijk, The Netherlands
[17] Lohrmann Observatory, Technische Universität Dresden, Mommsenstraße 13, 01062 Dresden, Germany
[18] European Space Astronomy Centre (ESA/ESAC), Camino bajo del Castillo, s/n, Urbanizacion Villafranca del Castillo, Villanueva de la Cañada, 28692 Madrid, Spain
[19] Université Côte d'Azur, Observatoire de la Côte d'Azur, CNRS, Laboratoire Lagrange, Bd de l'Observatoire, CS 34229, 06304 Nice Cedex 4, France
[20] CNES Centre Spatial de Toulouse, 18 avenue Edouard Belin, 31401 Toulouse Cedex 9, France
[21] Institut d'Astronomie et d'Astrophysique, Université Libre de Bruxelles CP 226, Boulevard du Triomphe, 1050 Brussels, Belgium
[22] F.R.S.-FNRS, Rue d'Egmont 5, 1000 Brussels, Belgium
[23] Telespazio Vega UK Ltd for ESA/ESAC, Camino bajo del Castillo, s/n, Urbanizacion Villafranca del Castillo, Villanueva de la Cañada, 28692 Madrid, Spain
[24] Laboratoire d'astrophysique de Bordeaux, Univ. Bordeaux, CNRS, B18N, allée Geoffroy Saint-Hilaire, 33615 Pessac, France
[25] Mullard Space Science Laboratory, University College London, Holmbury St Mary, Dorking, Surrey RH5 6NT, United Kingdom
[26] INAF - Osservatorio Astrofisico di Torino, via Osservatorio 20, 10025 Pino Torinese (TO), Italy
[27] INAF - Osservatorio di Astrofisica e Scienza dello Spazio di Bologna, via Piero Gobetti 93/3, 40129 Bologna, Italy
[28] Serco Gestión de Negocios for ESA/ESAC, Camino bajo del Castillo, s/n, Urbanizacion Villafranca del Castillo, Villanueva de la Cañada, 28692 Madrid, Spain
[29] ALTEC S.p.a, Corso Marche, 79,10146 Torino, Italy
[30] Department of Astronomy, University of Geneva, Chemin d'Ecogia 16, 1290 Versoix, Switzerland
[31] Gaia DPAC Project Office, ESAC, Camino bajo del Castillo, s/n, Urbanizacion Villafranca del Castillo, Villanueva de la Cañada, 28692 Madrid, Spain
[32] SYRTE, Observatoire de Paris, Université PSL, CNRS, Sorbonne Université, LNE, 61 avenue de l'Observatoire 75014 Paris, France
[33] National Observatory of Athens, I. Metaxa and Vas. Pavlou, Palaia Penteli, 15236 Athens, Greece
[34] IMCCE, Observatoire de Paris, Université PSL, CNRS, Sorbonne Université, Univ. Lille, 77 av. Denfert-Rochereau, 75014 Paris, France
[35] Royal Observatory of Belgium, Ringlaan 3, 1180 Brussels, Belgium
[36] Institut d'Astrophysique Spatiale, Université Paris XI, UMR 8617, CNRS, Bâtiment 121, 91405, Orsay Cedex, France

[37] Institute for Astronomy, University of Edinburgh, Royal Observatory, Blackford Hill, Edinburgh EH9 3HJ, United Kingdom
[38] Instituut voor Sterrenkunde, KU Leuven, Celestijnenlaan 200D, 3001 Leuven, Belgium
[39] Institut d'Astrophysique et de Géophysique, Université de Liège, 19c, Allée du 6 Août, B-4000 Liège, Belgium
[40] ATG Europe for ESA/ESAC, Camino bajo del Castillo, s/n, Urbanizacion Villafranca del Castillo, Villanueva de la Cañada, 28692 Madrid, Spain
[41] Área de Lenguajes y Sistemas Informáticos, Universidad Pablo de Olavide, Ctra. de Utrera, km 1. 41013, Sevilla, Spain
[42] ETSE Telecomunicación, Universidade de Vigo, Campus Lagoas-Marcosende, 36310 Vigo, Galicia, Spain
[43] Large Synoptic Survey Telescope, 950 N. Cherry Avenue, Tucson, AZ 85719, USA
[44] Observatoire Astronomique de Strasbourg, Université de Strasbourg, CNRS, UMR 7550, 11 rue de l'Université, 67000 Strasbourg, France
[45] Kavli Institute for Cosmology, University of Cambridge, Madingley Road, Cambride CB3 0HA, United Kingdom
[46] Aurora Technology for ESA/ESAC, Camino bajo del Castillo, s/n, Urbanizacion Villafranca del Castillo, Villanueva de la Cañada, 28692 Madrid, Spain
[47] Laboratoire Univers et Particules de Montpellier, Université Montpellier, Place Eugène Bataillon, CC72, 34095 Montpellier Cedex 05, France
[48] Department of Physics and Astronomy, Division of Astronomy and Space Physics, Uppsala University, Box 516, 75120 Uppsala, Sweden
[49] CENTRA, Universidade de Lisboa, FCUL, Campo Grande, Edif. C8, 1749-016 Lisboa, Portugal
[50] Università di Catania, Dipartimento di Fisica e Astronomia, Sezione Astrofisica, Via S. Sofia 78, 95123 Catania, Italy
[51] INAF - Osservatorio Astrofisico di Catania, via S. Sofia 78, 95123 Catania, Italy
[52] University of Vienna, Department of Astrophysics, Türkenschanzstraße 17, A1180 Vienna, Austria
[53] CITIC – Department of Computer Science, University of A Coruña, Campus de Elviña S/N, 15071, A Coruña, Spain
[54] CITIC – Astronomy and Astrophysics, University of A Coruña, Campus de Elviña S/N, 15071, A Coruña, Spain
[55] INAF - Osservatorio Astronomico di Roma, Via di Frascati 33, 00078 Monte Porzio Catone (Roma), Italy
[56] University of Helsinki, Department of Physics, P.O. Box 64, 00014 Helsinki, Finland
[57] Finnish Geospatial Research Institute FGI, Geodeetinrinne 2, 02430 Masala, Finland
[58] Isdefe for ESA/ESAC, Camino bajo del Castillo, s/n, Urbanizacion Villafranca del Castillo, Villanueva de la Cañada, 28692 Madrid, Spain
[59] STFC, Rutherford Appleton Laboratory, Harwell, Didcot, OX11 0QX, United Kingdom
[60] Dpto. de Inteligencia Artificial, UNED, c/ Juan del Rosal 16, 28040 Madrid, Spain
[61] Elecnor Deimos Space for ESA/ESAC, Camino bajo del Castillo, s/n, Urbanizacion Villafranca del Castillo, Villanueva de la Cañada, 28692 Madrid, Spain
[62] Thales Services for CNES Centre Spatial de Toulouse, 18 avenue Edouard Belin, 31401 Toulouse Cedex 9, France
[63] Department of Astrophysics/IMAPP, Radboud University, P.O.Box 9010, 6500 GL Nijmegen, The Netherlands
[64] European Southern Observatory, Karl-Schwarzschild-Str. 2, 85748 Garching, Germany
[65] ON/MCTI-BR, Rua Gal. José Cristino 77, Rio de Janeiro, CEP 20921-400, RJ, Brazil
[66] OV/UFRJ-BR, Ladeira Pedro Antônio 43, Rio de Janeiro, CEP 20080-090, RJ, Brazil
[67] Department of Terrestrial Magnetism, Carnegie Institution for Science, 5241 Broad Branch Road, NW, Washington, DC 20015-1305, USA
[68] Università di Torino, Dipartimento di Fisica, via Pietro Giuria 1, 10125 Torino, Italy
[69] Departamento de Astrofísica, Centro de Astrobiología (CSIC-INTA), ESA-ESAC. Camino Bajo del Castillo s/n. 28692 Villanueva de la Cañada, Madrid, Spain
[70] Leicester Institute of Space and Earth Observation and Department of Physics and Astronomy, University of Leicester, University Road, Leicester LE1 7RH, United Kingdom
[71] Departamento de Estadística, Universidad de Cádiz, Calle República Árabe Saharawi s/n. 11510, Puerto Real, Cádiz, Spain
[72] Astronomical Institute Bern University, Sidlerstrasse 5, 3012 Bern, Switzerland (present address)
[73] EURIX S.r.l., Corso Vittorio Emanuele II 61, 10128, Torino, Italy
[74] Harvard-Smithsonian Center for Astrophysics, 60 Garden Street, Cambridge MA 02138, USA
[75] HE Space Operations BV for ESA/ESAC, Camino bajo del Castillo, s/n, Urbanizacion Villafranca del Castillo, Villanueva de la Cañada, 28692 Madrid, Spain
[76] SISSA - Scuola Internazionale Superiore di Studi Avanzati, via Bonomea 265, 34136 Trieste, Italy
[77] University of Turin, Department of Computer Sciences, Corso Svizzera 185, 10149 Torino, Italy
[78] SRON, Netherlands Institute for Space Research, Sorbonnelaan 2, 3584CA, Utrecht, The Netherlands
[79] Dpto. de Matemática Aplicada y Ciencias de la Computación, Univ. de Cantabria, ETS Ingenieros de Caminos, Canales y Puertos, Avda. de los Castros s/n, 39005 Santander, Spain
[80] Unidad de Astronomía, Universidad de Antofagasta, Avenida Angamos 601, Antofagasta 1270300, Chile
[81] CRAAG - Centre de Recherche en Astronomie, Astrophysique et Géophysique, Route de l'Observatoire Bp 63 Bouzareah 16340 Algiers, Algeria
[82] University of Antwerp, Onderzoeksgroep Toegepaste Wiskunde, Middelheimlaan 1, 2020 Antwerp, Belgium
[83] INAF - Osservatorio Astronomico d'Abruzzo, Via Mentore Maggini, 64100 Teramo, Italy
[84] INAF - Osservatorio Astronomico di Capodimonte, Via Moiariello 16, 80131, Napoli, Italy
[85] Instituto de Astronomia, Geofìsica e Ciências Atmosféricas, Universidade de São Paulo, Rua do Matão, 1226, Cidade Universitaria, 05508-900 São Paulo, SP, Brazil
[86] Department of Astrophysics, Astronomy and Mechanics, National and Kapodistrian University of Athens, Panepistimiopolis, Zografos, 15783 Athens, Greece
[87] Leibniz Institute for Astrophysics Potsdam (AIP), An der Sternwarte 16, 14482 Potsdam, Germany
[88] RHEA for ESA/ESAC, Camino bajo del Castillo, s/n, Urbanizacion Villafranca del Castillo, Villanueva de la Cañada, 28692 Madrid, Spain
[89] ATOS for CNES Centre Spatial de Toulouse, 18 avenue Edouard Belin, 31401 Toulouse Cedex 9, France
[90] School of Physics and Astronomy, Tel Aviv University, Tel Aviv 6997801, Israel

[91] UNINOVA - CTS, Campus FCT-UNL, Monte da Caparica, 2829-516 Caparica, Portugal
[92] School of Physics, O'Brien Centre for Science North, University College Dublin, Belfield, Dublin 4, Ireland
[93] Dipartimento di Fisica e Astronomia, Università di Bologna, Via Piero Gobetti 93/2, 40129 Bologna, Italy
[94] Barcelona Supercomputing Center - Centro Nacional de Supercomputación, c/ Jordi Girona 29, Ed. Nexus II, 08034 Barcelona, Spain
[95] Department of Computer Science, Electrical and Space Engineering, Luleå University of Technology, Box 848, S-981 28 Kiruna, Sweden
[96] Max Planck Institute for Extraterrestrial Physics, High Energy Group, Gießenbachstraße, 85741 Garching, Germany
[97] Astronomical Observatory Institute, Faculty of Physics, Adam Mickiewicz University, Słoneczna 36, 60-286 Poznań, Poland
[98] Konkoly Observatory, Research Centre for Astronomy and Earth Sciences, Hungarian Academy of Sciences, Konkoly Thege Miklós út 15-17, 1121 Budapest, Hungary
[99] Eötvös Loránd University, Egyetem tér 1-3, H-1053 Budapest, Hungary
[100] American Community Schools of Athens, 129 Aghias Paraskevis Ave. & Kazantzaki Street, Halandri, 15234 Athens, Greece
[101] Faculty of Mathematics and Physics, University of Ljubljana, Jadranska ulica 19, 1000 Ljubljana, Slovenia
[102] Villanova University, Department of Astrophysics and Planetary Science, 800 E Lancaster Avenue, Villanova PA 19085, USA
[103] Physics Department, University of Antwerp, Groenenborgerlaan 171, 2020 Antwerp, Belgium
[104] McWilliams Center for Cosmology, Department of Physics, Carnegie Mellon University, 5000 Forbes Avenue, Pittsburgh, PA 15213, USA
[105] Astronomical Institute, Academy of Sciences of the Czech Republic, Fričova 298, 25165 Ondřejov, Czech Republic
[106] Telespazio for CNES Centre Spatial de Toulouse, 18 avenue Edouard Belin, 31401 Toulouse Cedex 9, France
[107] Institut de Physique de Rennes, Université de Rennes 1, 35042 Rennes, France
[108] Shanghai Astronomical Observatory, Chinese Academy of Sciences, 80 Nandan Rd, 200030 Shanghai, China
[109] School of Astronomy and Space Science, University of Chinese Academy of Sciences, Beijing 100049, China
[110] Niels Bohr Institute, University of Copenhagen, Juliane Maries Vej 30, 2100 Copenhagen Ø, Denmark
[111] DXC Technology, Retortvej 8, 2500 Valby, Denmark
[112] Las Cumbres Observatory, 6740 Cortona Drive Suite 102, Goleta, CA 93117, USA
[113] Astrophysics Research Institute, Liverpool John Moores University, 146 Brownlow Hill, Liverpool L3 5RF, United Kingdom
[114] Baja Observatory of University of Szeged, Szegedi út III/70, 6500 Baja, Hungary
[115] Laboratoire AIM, IRFU/Service d'Astrophysique - CEA/DSM - CNRS - Université Paris Diderot, Bât 709, CEA-Saclay, 91191 Gif-sur-Yvette Cedex, France
[116] Warsaw University Observatory, Al. Ujazdowskie 4, 00-478 Warszawa, Poland
[117] Institute of Theoretical Physics, Faculty of Mathematics and Physics, Charles University in Prague, Czech Republic
[118] AKKA for CNES Centre Spatial de Toulouse, 18 avenue Edouard Belin, 31401 Toulouse Cedex 9, France
[119] Vitrociset Belgium for ESA/ESAC, Camino bajo del Castillo, s/n, Urbanizacion Villafranca del Castillo, Villanueva de la Cañada, 28692 Madrid, Spain
[120] HE Space Operations BV for ESA/ESTEC, Keplerlaan 1, 2201AZ, Noordwijk, The Netherlands
[121] Space Telescope Science Institute, 3700 San Martin Drive, Baltimore, MD 21218, USA
[122] QUASAR Science Resources for ESA/ESAC, Camino bajo del Castillo, s/n, Urbanizacion Villafranca del Castillo, Villanueva de la Cañada, 28692 Madrid, Spain
[123] Fork Research, Rua do Cruzado Osberno, Lt. 1, 9 esq., Lisboa, Portugal
[124] APAVE SUDEUROPE SAS for CNES Centre Spatial de Toulouse, 18 avenue Edouard Belin, 31401 Toulouse Cedex 9, France
[125] Nordic Optical Telescope, Rambla José Ana Fernández Pérez 7, 38711 Breña Baja, Spain
[126] Spanish Virtual Observatory
[127] Fundación Galileo Galilei - INAF, Rambla José Ana Fernández Pérez 7, 38712 Breña Baja, Santa Cruz de Tenerife, Spain
[128] INSA for ESA/ESAC, Camino bajo del Castillo, s/n, Urbanizacion Villafranca del Castillo, Villanueva de la Cañada, 28692 Madrid, Spain
[129] Dpto. Arquitectura de Computadores y Automática, Facultad de Informática, Universidad Complutense de Madrid, C/ Prof. José García Santesmases s/n, 28040 Madrid, Spain
[130] H H Wills Physics Laboratory, University of Bristol, Tyndall Avenue, Bristol BS8 1TL, United Kingdom
[131] Institut d'Estudis Espacials de Catalunya (IEEC), Gran Capita 2-4, 08034 Barcelona, Spain
[132] Applied Physics Department, Universidade de Vigo, 36310 Vigo, Spain
[133] Stellar Astrophysics Centre, Aarhus University, Department of Physics and Astronomy, 120 Ny Munkegade, Building 1520, DK-8000 Aarhus C, Denmark
[134] Argelander-Institut fü Astronomie, Universität Bonn, Auf dem Hügel 71, 53121 Bonn, Germany
[135] Research School of Astronomy and Astrophysics, Australian National University, Canberra, ACT 2611 Australia
[136] Sorbonne Universités, UPMC Univ. Paris 6 et CNRS, UMR 7095, Institut d'Astrophysique de Paris, 98 bis bd. Arago, 75014 Paris, France
[137] Department of Geosciences, Tel Aviv University, Tel Aviv 6997801, Israel

ABSTRACT

Aims. The goal of this paper is to demonstrate the outstanding quality of the 2nd Data Release of the *Gaia* mission and its power to constrain many different aspects of the dynamics of the satellites of the Milky Way. We focus here on determining the proper motions of 75 Galactic globular clusters, 9 dwarf spheroidal galaxies and one ultra-faint system, and the Large and Small Magellanic Clouds.
Methods. Using data extracted from the *Gaia* archive, we derive the proper motions and parallaxes for these systems, as well as their uncertainties. We demonstrate that the errors, statistical and systematic, are relatively well understood. We have integrated the orbits of these objects in three different Galactic potentials, and characterised their properties. We present the derived proper motions, space velocities and characteristic orbital parameters in various tables to facilitate their use by the astronomical community.

Results. Our limited and straightforward analyses have allowed us for example, to: (*i*) determine absolute and very precise proper motions for globular clusters; (*ii*) detect clear rotation signatures in the proper motions of at least 5 globular clusters; (*iii*) show that the satellites of the Milky Way are all on high inclination orbits, but that they do not share a single plane of motion; (*iv*) derive a lower limit for the mass of the Milky Way of $9.8^{+6.7}_{-2.7} \times 10^{11}$ $M_\odot$ based on the assumption that the Leo I dwarf spheroidal is bound; (*v*) derive a rotation curve for the LMC based solely on proper motions that is competitive with line-of-sight velocity curves, now using many orders of magnitude more sources; and (*vi*) unveil the dynamical effect of the bar on the motions of stars in the LMC.
Conclusions. All these results highlight the incredible power of the *Gaia* astrometric mission, and in particular of its second Data Release.

Key words. Galaxy: kinematics and dynamics – Galaxy: halo, Magellanic Clouds – globular clusters: general – galaxies: dwarf, Local Group – methods: data analysis, astrometry

1. Introduction

The possibility of determining for the first time the absolute proper motions of stars in the satellites of the Milky Way opens up a whole new window for understanding their dynamics, origin and evolution, as well as that of the Milky Way itself. The data presented in the Second *Gaia* Data Release (hereafter DR2, Gaia Collaboration et al. 2018b) allows us to achieve this goal. In this paper we study the proper motions (PM hereafter) of stars in a large sample of globular clusters, in the classical dwarf spheroidal galaxies and one ultra-faint system, and in the Large and Small Magellanic Clouds (LMC and SMC hereafter).

There are a plethora of interesting science questions that can be addressed with this dataset. In this Introduction, we do not aim to be fully comprehensive but we will mention a few topics to set the context, to highlight the power of unprecedentedly accurate absolute PM measurements and also to trigger the readers' curiosity to explore this outstanding dataset themselves.

Proper motion studies of satellite systems, such as the globular clusters and dwarf galaxies of the Milky Way, have a long history starting from the use of photographic plates sometimes taken with a time baseline longer than 100 years (see Meylan & Heggie (1997) and van Leeuwen et al. (2000) for interesting and thorough historical reviews on the determination of PM of stars in globular clusters). More recently, the space missions Hipparcos and the Hubble Space Telescope (HST), and of course the *Gaia* mission in its first data release (Gaia Collaboration et al. 2016) have demonstrated the enormous power of space-based astrometry. Hipparcos data (Perryman et al. 1997) has been used for many purposes, and in particular to study the dynamics of nearby open clusters (e.g. van Leeuwen 1999, 2009), and although Hipparcos did not observe stars in globular clusters, it did provide an absolute reference frame that was used to derive for example the orbits of 15 globular clusters from photographic plates (Odenkirchen et al. 1997). On the other hand, HST has carried out several large (legacy) surveys (e.g. Soto et al. 2017) that have allowed studies of the dynamics of globular clusters and of the Milky Way satellites and has even constrained the motions of our largest neighbouring galaxy M31 (Sohn et al. 2012). In all these cases, relative astrometry is done using background quasars and distant galaxies to define a reference frame, and typically a time baseline of 5 – 10 years is used. This has been a highly successful approach, and has, for example, allowed researchers to put forward the idea that the Magellanic Clouds may be on their first infall (Kallivayalil et al. 2006b; Besla et al. 2007), to put constraints on the mass of the Milky Way from its most distant satellite Leo I (Boylan-Kolchin et al. 2013), and also to argue in support of the conjecture that dwarf galaxy satellites may lie on a vast polar plane based on the first constraints on their orbits (Pawlowski & Kroupa 2013).

This brief overview gives a flavour of the palette of scientific results that can be derived from accurate PM information of the satellites of the Milky Way. In combination with knowledge of the line-of-sight velocities, PM can be used to derive orbits for these systems. This is interesting for a large number of reasons, some of which we highlight below.

The orbits of globular clusters can shed light on their formation and evolution, for example on which may have formed in-situ and which could be accreted (Searle & Zinn 1978; Mackey & Gilmore 2004; Renaud et al. 2017). Furthermore, knowledge of the orbits helps understanding the effect of tides and the interplay with internal processes, such as evaporation, mass segregation and two-body relaxation (Djorgovski & Meylan 1994; Baumgardt & Makino 2003). From the orbits it is also possible to aid the search for extra-tidal stars and streamers, which are very useful for constraining the gravitational potential of the Milky Way because of the coldness of such streams (Küpper et al. 2015).

In the case of the dwarf galaxy satellites of the Milky Way, knowledge of the orbits has also multiple implications that range from the scale of the formation of the smallest galaxies in the Universe to constraints and challenges to the cosmological model. By determining the orbits of dwarf galaxies we can establish the impact of the environment on their evolution, including star formation and chemical enrichment histories (Tolstoy et al. 2009), and also the effect of ram pressure stripping and put constraints on the hot gaseous halo of the Milky Way (Nichols & Bland-Hawthorn 2011). The structure of these small galaxies may also have been strongly affected by tidal interactions with the Milky Way, and to quantify the importance of this process knowledge of the orbits is imperative (Kazantzidis et al. 2011). Furthermore, such knowledge also allows to establish if there is internal rotation and its amplitude (Battaglia et al. 2008), which is relevant for understanding the formation path of dSph galaxies. For the ultra-faint galaxies, whose nature is debated, PM are useful also for the identification of interlopers, which is particularly important for establishing if these systems are (on the verge of being) disrupted or embedded in a dark matter halo.

The orbits of the Milky Way satellites (both globular clusters and dwarf galaxies) also provide information on the Milky Way itself, such as for example, its dynamical mass (e.g. Wilkinson & Evans 1999). It is likely that the internal dynamics of the Milky Way have also been affected by the gravitational influence of, in particular, the Sagittarius dwarf (Gómez et al. 2013) and the LMC (Bekki 2012; Gómez et al. 2015), and improved knowledge of the orbits of these objects will allow us to understand what their effect has been. On the other hand, orbits also allow us to gain insight into how a galaxy acquires its satellite population. For example, it has been argued that the satellites lie preferentially on streams (Lynden-Bell & Lynden-Bell 1995), on a thin plane (Kroupa et al. 2005), or that they have fallen in groups (Li & Helmi 2008), of which the LMC/SMC and their recently discovered satellites are direct proof (Bechtol et al. 2015; Koposov et al. 2015). The *Gaia* DR2 data will allow us to establish how

real and important these associations are, and also whether the orbits found are consistent with the expectations from the concordance cosmological model.

In this paper we will analyse 75 globular clusters in our Galaxy, and we will demonstrate that the *Gaia* DR2 proper motion measurements for these clusters are of outstanding quality, with the formal and systematic uncertainties being effectively negligible. In comparison to previous efforts (e.g. Dinescu et al. 2003; Casetti-Dinescu et al. 2007, 2010, 2013), there is a reduction of nearly two orders of magnitude in the errors. This dramatic improvement will enable also detailed studies of the internal dynamics that could shed light onto how these objects formed and their evolutionary path (Gratton et al. 2012). Some of the questions that could potentially be addressed include for example, have globular clusters formed in mini-halos or are they fully devoid of dark matter (Ibata et al. 2013)? Do they host intermediate mass black holes (Baumgardt 2017)? Are there dynamical differences between the different populations known to be present in many globular clusters (Bellazzini et al. 2012; Bellini et al. 2015; Vesperini et al. 2013)? Has the formation process and evolution for in-situ clusters been the same as for those that have been accreted? Have these processes left an imprint in the internal phase-space distribution of their stars? How many clusters show rotation and what is the link to how they have formed (Hénault-Brunet et al. 2015)? Many of the globular clusters are also being targeted by radial velocity surveys (e.g. Lardo et al. 2015; Kamann et al. 2017), and the combination of *Gaia* DR2 with such datasets will be extremely powerful.

In this paper we will also study the Magellanic Clouds, the 9 classical dSph and include the UFD Bootes I as an example of what can be done with *Gaia* DR2 data. Even though the dwarf galaxies are on average farther away, their mean proper motions can be very well determined using *Gaia* DR2, and they are still above the systematic level. Although for many objects, the uncertainties are comparable to those achievable using HST, the advantage of having a full view of these galaxies and of the proper motions being in an absolute reference frame cannot be over-emphasized. For the dwarf spheroidal galaxies establishing their internal dynamics using this dataset is however not yet feasible, although perhaps the combination of *Gaia* and HST will allow to make progress before the end of the *Gaia* mission (as recently demonstrated by Massari et al. 2018). For the Magellanic Clouds, *Gaia* DR2 gives a clearer, more detailed view of the internal dynamics than has ever been possible before, with measured proper motions for millions of sources.

The paper is structured as follows. The main part introduces the DR2 data, methodology and analysis including orbit integrations, and for the interested reader details are given in the Appendix. The Appendix also contains Tables with the measured PM for the objects studied, as well as a list of the orbital parameters derived. More specifically in Sec. 2 of the main paper we present the *Gaia* DR2 data, with emphasis on the astrometry, the selection procedures and the methodology. Sec. 2.1 focuses on the derivation of the proper motions of the globular clusters and dSph, and in Sec. 2.2 we describe the procedures that are tailored for the LMC and SMC. We then present the various analyses of the datasets that we have carried out and which allow us to show the superb quality of the data. Sec. 3 concentrates on the globular clusters, Sec. 4 on the dSph and Sec. 5 on the Magellanic Clouds. In Sec. 6 we determine the orbits of the satellites using different Galactic potentials, a showcase of the fantastic possibilities that *Gaia* DR2 offers for studies of the dynamics and origin of the satellites of the Milky Way. In Sec. 7 we discuss our findings, provide an example of the use of DR2 astrometry to find tidal debris, present a summary of what lies beyond a straightforward analysis of the data such as that presented here, as well as what will need to wait for later *Gaia* data releases (i.e. what are the limitations of the *Gaia* DR2 dataset). We present our conclusions in Sec. 8.

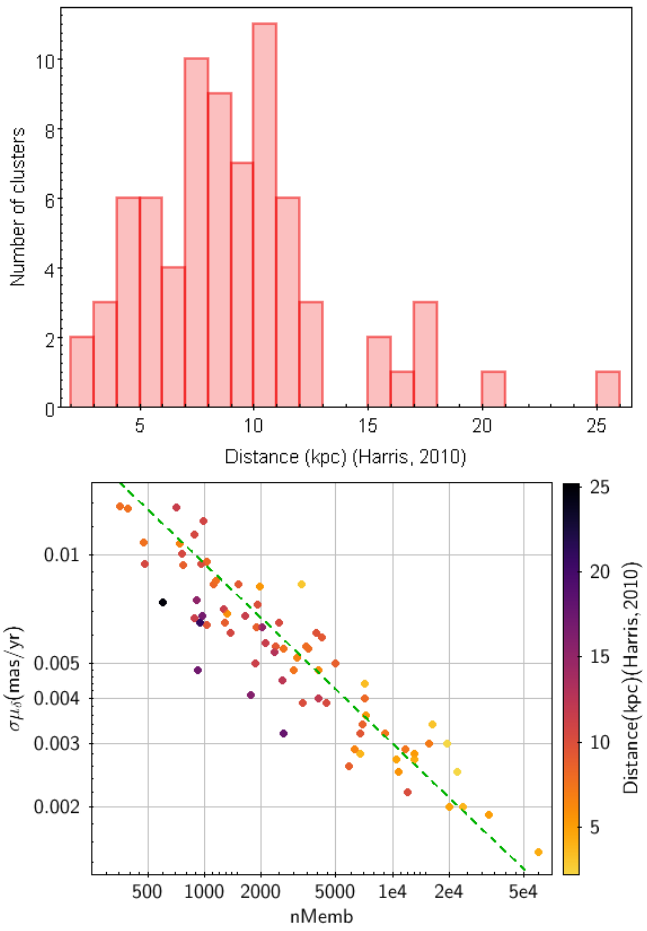


Fig. 1. *Top*: Distance distribution of the 75 globular clusters included in the present study. *Bottom*: the standard uncertainties on the proper motion in declination as a function of number of cluster members *nMemb* used in the solution. The diagonal line represents a fit to the relation $\sigma\mu_\delta = a/\sqrt{nMemb}$ where we find $a = 0.3$. A similar dependence on the number of members is found for the parallax uncertainty (with $a = 0.15$) and for $\sigma\mu_{\alpha*}$ (where $a = 0.25$).

2. Data and methodology

The data used in the present study is the second *Gaia* data release as described in Gaia Collaboration et al. (2018b). Further details on its validation may be found in Arenou et al. (2018). The procedures to derive the *Gaia* astrometric solution (also known as AGIS) are described in detail in Lindegren et al. (2016); Lindegren & et al. (2018). We remind the reader that the astrometric parameters are absolute in the sense that they do not rely on an external reference frame.

2.1. Globular clusters and dwarf galaxies

The sample of globular clusters we analyse in this paper includes half of the whole population of globular clusters in the Milky Way. We focus mostly on those clusters located within a distance limit of 12 to 13 kpc, to achieve a reasonable compromise

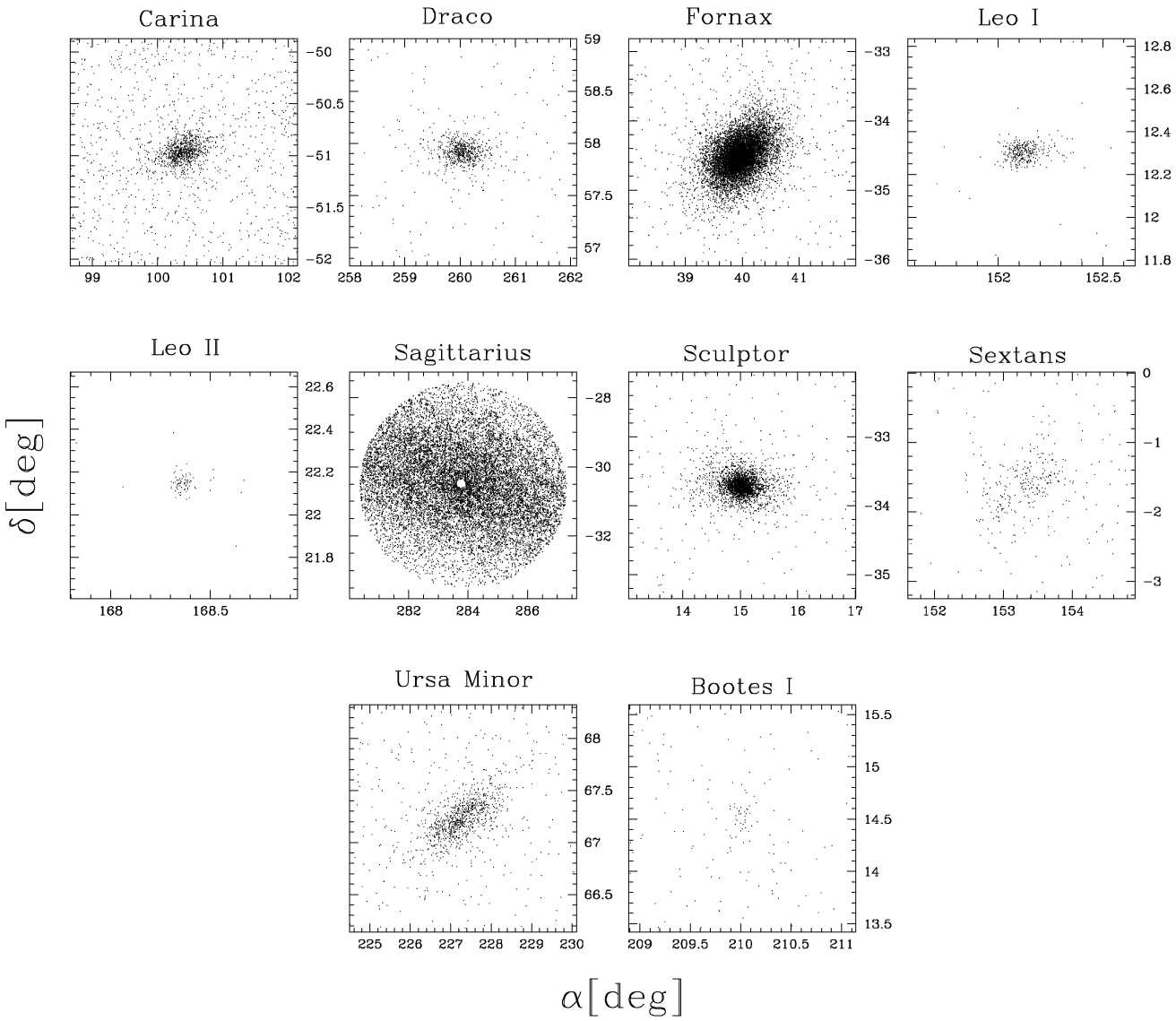


Fig. 2. Field-of-view towards the dwarf spheroidal galaxies (the nine classical and one UFD) in our sample. The stars shown correspond to members according to the photometric selection (on the RGB and BHB) and the astrometric procedure (within 2σ from the mean proper motion of the object). The striping apparent in Sagittarius and Sextans is driven in part by the scanning law. The hole in the centre of Sagittarius corresponds to the location of the globular cluster NGC 6715 (M54).

on the number of stars with reliable astrometric solutions. It is important to bear in mind that the astrometric solutions for stars in areas of high stellar density, such as the cores of the clusters, are more likely to be disturbed due to image blending and onboard image selection. This plays a significant role when observing more distant clusters and affects in particular the fainter stars (see e.g. Pancino et al. 2017). Our selection also takes into account the ability to distinguish (in PM and parallax space) the cluster stars from those in the field both as a function of distance from the cluster centre and of magnitude. Furthermore, clusters at low galactic latitude have also generally been avoided to escape confusion with field stars. The top panel of Figure 1 shows a histogram of the distance distribution for the 75 globular clusters included in the present study. The bottom panel exemplifies how the standard uncertainties on the cluster proper motion in declination vary as a function of the number of cluster members used[1].

As Fig. 2 shows, we also study in this paper the classical dSph and one ultra-faint dwarf galaxy, Bootes I. UFD galaxies are intrinsically very faint as their name indicates, and this implies that there are very few stars on the red giant branch (RGB), and depending on the distance to the system, there may be even fewer because of the somewhat bright faint magnitude limit of *Gaia* (G = 21). Bootes I is in fact the best UFD case for *Gaia* DR2, because its RGB is relatively well-populated (at least in comparison with other UFDs), and it is relatively near (at 60 kpc, Belokurov et al. 2006). These conditions allow us to apply a homogeneous selection and analysis procedures to all

[1] Note the tendency for more distant clusters to show smaller uncertainties at a fixed number of members. This is driven by the fact that for more distant clusters only the brighter and less populated part of the luminosity function is effectively sampled, and this implies a lower crowding impact (Pancino et al. 2017).

the dwarfs in our sample, which we find highly desirable at this point. With external knowledge of e.g. radial velocity members, it might however be possible to derive the PM for more UFDs, but the Bootes I case already illustrates the problems to be faced with *Gaia* DR2 data for this type of systems.

The selection procedure, which is described in detail in Appendix A.1, starts with the extraction of data for each object from the GACS archive. The archive provides us with the astrometric parameters, their standard uncertainties and error correlations, the photometric data with standard uncertainties (flux values and fluxes converted to magnitudes), various statistics relating to the astrometric and photometric solutions, and radial velocities where available for our analysis. Depending on the nature of the object analysed, we set different magnitude limits. For the dwarf galaxies, we first consider stars with $G < 21$. For the globular clusters the limit was generally set at $G = 20$, but in a few cases we took a brighter value to limit the contamination by field stars. This was in particular needed for clusters at low galactic latitude.

The *Gaia* sky coverage can show locally strong variations that can affect the selection of members with good astrometric solutions (Gaia Collaboration et al. 2018b; Arenou et al. 2018). In addition, for many of the globular clusters the central core is often poorly resolved. These conditions will reflect in the standard uncertainties of the derived parameters, but are unlikely to cause a systematic bias in the results. The most seriously affected cluster ω Cen (see Fig. A.6), still shows good astrometric data for large numbers of stars. In the case of the dSph galaxies, the most affected object is Sextans as can be seen from Fig. 2. The inhomogeneous distribution of sources is related to the number of independent scans in the field of view towards the dwarf. To determine the astrometric parameters reliably, a sufficiently high number of truly independent scans are necessary. This is measured by the parameter `visibility-periods-used` which has to reach a value greater than 5 for an object's five-parameter solution (i.e. including the proper motions and parallax) to be considered reliable (Lindegren & et al. 2018), otherwise only its position on the sky is determined. There are other instrumental effects that affect the astrometric parameters, and these are discussed elsewhere in the paper and in Lindegren & et al. (2018).

The first step in our procedure to derive the motions of the satellites is to focus on an area of the sky, centred on the assumed centre of the object of interest and with an assumed maximum radius. For the dwarf galaxies, these radii are fixed at 2 deg, except for the Sagittarius dwarf for which we take 3 deg (and we also exclude stars within one tidal radius of its nuclear globular cluster M54). For the globular clusters, we interactively explore the data using the TopCat software (Taylor 2005), and then make a pre-selection of members based on the concentration of the proper motions, followed by a cutoff in parallax, as well as on inspection of the colour-magnitude diagram (for more details see Appendix A.1).

Because of their low stellar density contrast, and thus of the higher number of contaminants (non-member stars) in the field-of-view, for the dwarf spheroidal galaxies we apply additional selection criteria in order to obtain a more robust estimate of the mean proper motions. First, we only consider stars within 1.5× the tidal radius (r_t) of each dwarf (taken from Irwin & Hatzidimitriou 1995; Roderick et al. 2016, for Bootes), except for Sagittarius where we consider all the stars in the 3 deg radius field-of-view. Then for all dSph, we also perform a cut in relative parallax error to remove foreground sources, as nearby stars will have relatively good parallaxes, especially in comparison to the stars in the dwarf galaxies. The relative error we use is $0 < \sigma_\varpi/\varpi < 0.5$ (which is equivalent to $\varpi - 2\sigma_\varpi > 0$), and corresponds to removing stars within roughly 5 kpc from the Sun. Finally, we use the distribution of sources in the CMD to isolate the giant branch (RGB and HB), as shown in Fig. 3 with the blue lines. In the case of the Sagittarius dwarf, we actually use a slightly different selection and focus on the reddest part of the RGB. The reason for this is the very large foreground which overlaps substantially with the bluer portions of Sagittarius' RGB.

The astrometric solution to derive the proper motions and parallaxes for the globular clusters and the dwarf galaxies follows the procedures described in van Leeuwen (2009); Gaia Collaboration et al. (2017, see also Appendix A.1). A joint solution for the proper motion and parallax is obtained that takes into account the full error correlation matrix as evaluated for each contributing star:

$$\mathcal{N} = \mathcal{N}_a + \mathcal{N}_v + \mathcal{N}_d. \quad (1)$$

The three main contributions to the noise matrix in Eq. (1) come from the astrometric solution $\mathcal{N}_a$, the estimated contributions from the internal velocity dispersion on the proper motion dispersion $\mathcal{N}_v$, and the dispersion of the parallaxes from the depth of the cluster $\mathcal{N}_d$, respectively. For the dwarf galaxies the second and third of these contributions could be ignored, as even the brightest stars in these systems still have standard uncertainties on the astrometric parameters that are relatively large in comparison[2]. Although for most globular clusters the velocity dispersion shows a clear gradient with respect to distance from the cluster centre (see Fig. A.5), we do not take it into account. This would have required a detailed investigation of the actual distribution of the proper motions as a function of radial distance, which is outside the scope of the present paper. The internal velocity dispersion as implemented is an average over the cluster.

The procedure used for determining the astrometric parameters is iterative and requires a first guess for the parallax and proper motions. For the globular clusters, this first guess was obtained using the TopCat software (Taylor 2005) as described above. While iterating, several diagnostics are produced, and in particular we plot the surface density as a function of distance from the centre of the cluster. Often such a diagram shows that the maximum radius initially considered in the data extraction step can be extended farther out (i.e. the background density has not yet been reached). In that case, we retrieve more data from the GACS archive using an increased radius and the latest values found for the proper motion and parallax. We then repeat the procedure again, now with the starting guesses being those given by the latest astrometric solution. This process is repeated until it is clear that the maximum radius has been reached.

The maximum radius for the cluster, i.e. the distance from the centre within which we still detect cluster stars (3σ from the mean PM, where σ is the error on the PM derived using Eq. 1) is compared to the tidal radii r_t extracted from Harris (1996) and its 2010 update (hereafter Harris10, Harris 2010). Fig. 4 shows that for the majority of the clusters this maximum radius is between 1/2 and 2 times the published estimate of the tidal radius. Clusters for which the maximum radius was found to be much smaller than r_t are often affected by a high density field star population, making the detection of cluster members problematic. Note that the r_t typically has been estimated by fitting a King profile to the projected density distribution of stars, and thus does

[2] We chose to set the intrinsic dispersion to the characteristic 10 km s^{-1} value found for the dwarfs from radial velocity data. However we have tested different input values and found the results on the mean proper motion to be robust.

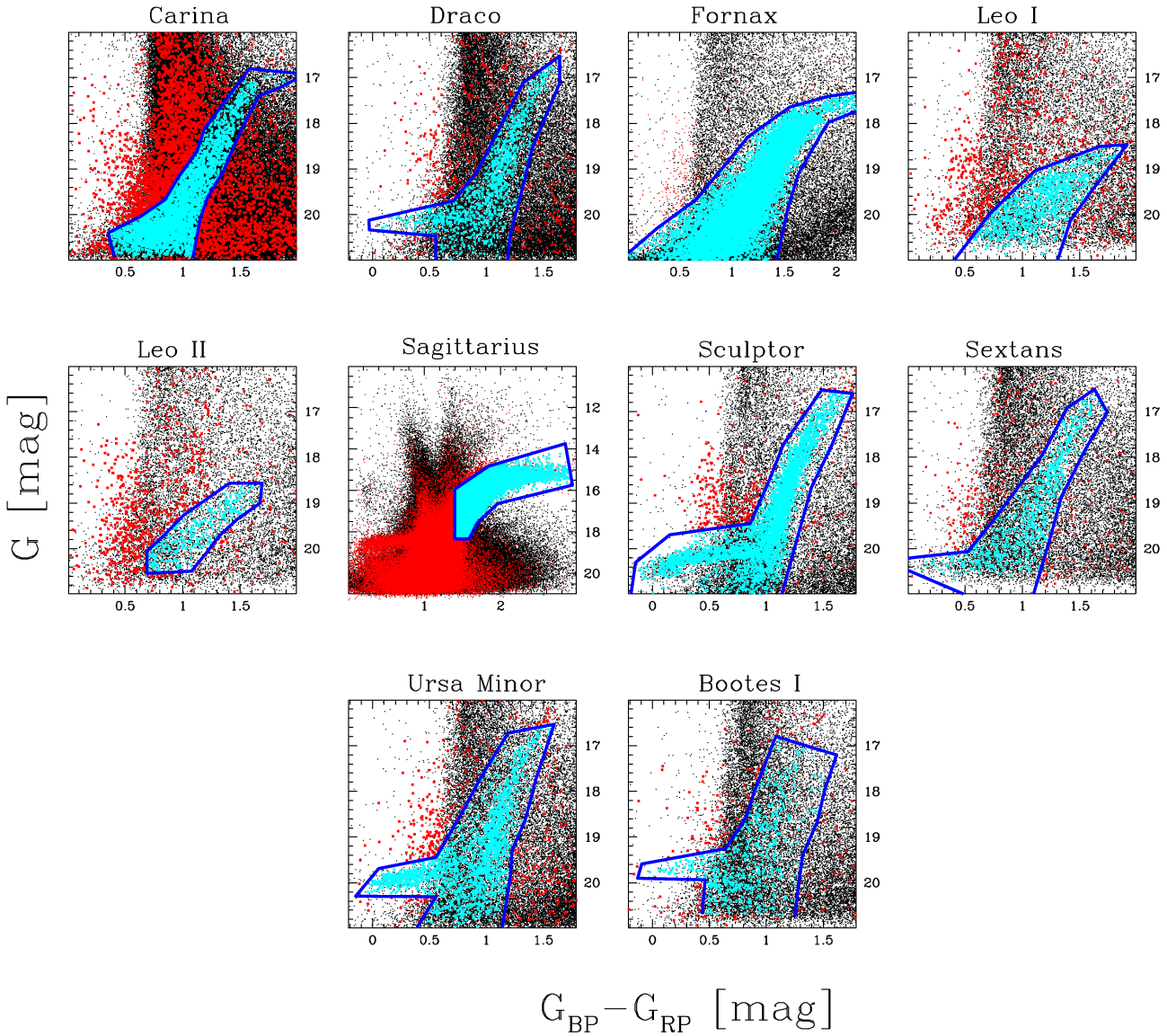


Fig. 3. Colour-magnitude of the stars in the field-of-view towards the dSph galaxies (the eight classical and one UFD) in our sample. The blue lines mark our (relatively tight) pre-selection of tentative members (on the RGB and BHB) that is fed to the pipeline to derive mean proper motions. The coloured points indicate stars within 3σ of our determination of the mean proper motion of the object. Therefore those in cyan satisfy both the PM and CMD selections.

not necessarily nor always reflect the true extent of a cluster (see e.g. Küpper et al. 2010).

In the case of the globular clusters, the contamination by field stars was checked through the dispersion diagrams (see Fig. A.4 for two examples), in which the distribution of proper motion and parallax was plotted against the standard uncertainties of the measurements, and compared with the expected distributions that include all noise contributions. A contaminating source, such as the SMC for 47 Tuc (NGC 104), shows as an offset over-density in one or more of these charts, and is in that case removed by applying a 3σ filter to the residuals in all three observables, i.e. relative proper motions and parallax.

We also note that the parallax reference value used for the data extraction is the *Gaia* parallax for the cluster, which can differ from what is considered the best value for the cluster based on the distance from the literature (see Sec. 3 for more details).

In the case of the dwarf galaxies, the iterative procedures are similar except that further iterations with the GACS archive are not necessary given our choices of initial field sizes. We thus work only with the data extracted in the first step as described earlier in this section. We have found however, that we obtain more reliable mean PM using only stars brighter than a magnitude limit in the range $19.1 < G < 20$. This is the faintest magnitude at which the mean value of the astrometric parameters becomes stable and where the effects of contaminating field stars and the large measurement uncertainties of very faint stars are minimised.

2.2. The Magellanic Clouds

The LMC and SMC present a different analytical challenge to the analysis of dwarfs and globular clusters, because they are very

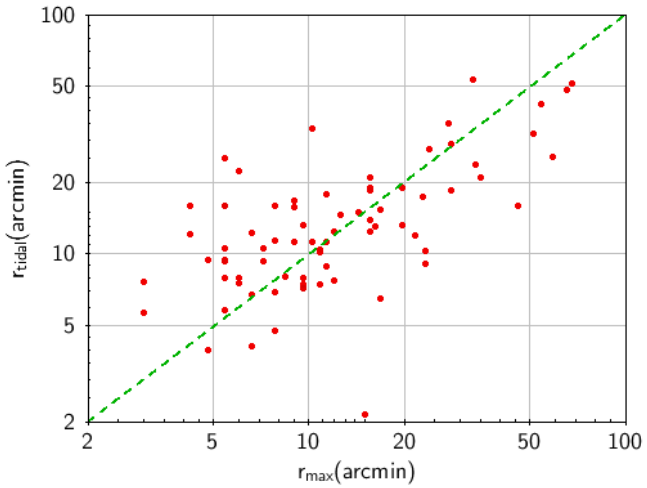


Fig. 4. Comparison between the tidal radii r_t (according to Harris10) of the 75 globular clusters in our sample and the maximum radii at which we have been able to detect cluster members in the present study. The diagonal line represents the one-to-one relation.

.

extended on the sky and contain 2 orders of magnitudes more *Gaia* sources than any of the dwarfs or clusters analysed.

To simplify our analysis, and ensure that the quoted (and plotted) proper motions are relatively easy to interpret in terms of internal velocities, it is particularly helpful to define an orthographic projection of the usual celestial coordinates and proper motions:

$$\begin{aligned} x &= \cos\delta \sin(\alpha - \alpha_C) \\ y &= \sin\delta\cos\delta_C - \cos\delta\sin\delta_C\cos(\alpha-\alpha_C) \\ \mu_x &= \mu_{\alpha*}\cos(\alpha-\alpha_C) - \mu_\delta \sin\delta\sin(\alpha-\alpha_C) \\ \mu_y &= \mu_{\alpha*}\sin\delta_C\sin(\alpha-\alpha_C) \\ &\quad + \mu_\delta(\cos\delta\cos\delta_C + \sin\delta\sin\delta_C\cos(\alpha-\alpha_C)) \end{aligned} \tag{2}$$

The centres of the coordinate systems are chosen to be the dynamical centre of the HI gas, respectively for the LMC and SMC, $(\alpha_{C,\mathrm{LMC}}, \delta_{C,\mathrm{LMC}}) = (78.^\circ77, -69.^\circ01)$ and $(\alpha_{C,\mathrm{SMC}}, \delta_{C,\mathrm{SMC}}) = (16.^\circ26, -72.^\circ42)$ (Luks & Rohlfs 1992; Kim et al. 1998; Stanimirović et al. 2004)[3]. Figure 5 shows the density of stars in this x, y-plane for the LMC and SMC, with these centres assumed.

If we approximate each cloud as being a thin disc, with some bulk motion, rotating about a point with celestial coordinates (α_C, δ_C) with a constant angular velocity ω and no other streaming motion, it can be shown (Appendix B) that these coordinates are, to first order, straightforwardly related to the parameters that describe the position and motion of the disc. These approximations are reasonable towards the centre of the LMC, and will serve as a first approximation for the SMC.

It is convenient to define $\boldsymbol{n}$ to be the unit vector normal to the disc (such that rotation is positive about $\boldsymbol{n}$), with $\boldsymbol{z}$ the unit vector from the observer to the reference centre (α_C, δ_C) at the reference epoch. We then have the mutually orthogonal unit vectors in the plane of the disc $\boldsymbol{l} = \boldsymbol{z}\times\boldsymbol{n}/|\boldsymbol{z}\times\boldsymbol{n}|$ and $\boldsymbol{m} = \boldsymbol{n}\times\boldsymbol{l}$. These have the property that $\boldsymbol{l}$ points in the direction of the receding node (the intersection of the disc with the tangent plane of the celestial sphere).

[3] Following van der Marel & Kallivayalil (2014) we have taken the LMC centre to be the average of the centres determined by Kim et al. (1998) and Luks & Rohlfs (1992).

If we define v_x, v_y to be the centre-of-mass motion of the cloud in the x and y directions, and v_z to be the same along the line of sight (divided by the distance to the cloud, to put it in the same units) then we have, to first order

$$\begin{aligned} \partial\mu_x/\partial x &\approx a v_x - v_z + a l_x m_z \omega \\ \partial\mu_x/\partial y &\approx b v_x - n_z\omega + b l_x m_z \omega \\ \partial\mu_y/\partial x &\approx a v_y + n_z\omega + a l_y m_z \omega \\ \partial\mu_y/\partial y &\approx b v_y - v_z + b l_y m_z \omega \end{aligned} \tag{3}$$

where, with inclination i (the angle between the line-of-sight direction to the cloud centre and the rotation axis of the disc, with $i > 90^\circ$ for retrograde motion)[4], and Ω the position angle of the receding node, measured from $\boldsymbol{y}$ towards $\boldsymbol{x}$, i.e. from North towards East we have the components of $\boldsymbol{l}, \boldsymbol{m}, \boldsymbol{n}$ being

$$\begin{bmatrix} l_x & m_x & n_x \\ l_y & m_y & n_y \\ l_z & m_z & n_z \end{bmatrix} = \begin{bmatrix} \sin\Omega & -\cos i\cos\Omega & \sin i\cos\Omega \\ \cos\Omega & \cos i\sin\Omega & -\sin i\sin\Omega \\ 0 & \sin i & \cos i \end{bmatrix} \tag{4}$$

and

$$a = \tan i\cos\Omega\,, \quad b = -\tan i\sin\Omega\,. \tag{5}$$

This means that, simply by finding a linear fit to the proper motion as a function of position on the sky, yielding the bulk motion perpendicular to the line of sight, and four gradients, we have four equations for four (in principle) free parameters – v_z, i, Ω and ω. The first, v_z, produces a perspective contraction (or expansion) as the clouds appear to shrink as they move away from us (or the opposite). The last three describe the orientation and rotation of the disc, which also leave a signature in the proper motions.

In practise, neither cloud is flat or expected to have perfectly circular streaming motion. The assumption of a constant angular velocity is approximately valid in the central few degrees of the LMC, but breaks down at larger radii. Nonetheless these approximations do allow us to draw tentative conclusions about the orientation and velocity curve of the Cloud from these simple to measure gradients.

We could take some of the 4 'free' parameters from other studies, but in practice we only ever do this for v_z. For the LMC we take the line of sight velocity from van der Marel et al. (2002, $262.2 \pm 3.4\,\mathrm{km\,s^{-1}}$) and the distance from Freedman et al. (2001, $50.1 \pm 2.5\,\mathrm{kpc}$) and for the SMC we take the line of sight velocity from Harris & Zaritsky (2006, $145.6 \pm 0.6\,\mathrm{km\,s^{-1}}$) and the distance from Cioni et al. (2000b, $62.8 \pm 2.4\,\mathrm{kpc}$). This gives us $v_{z,\mathrm{LMC}} = 1.104 \pm 0.057\,\mathrm{mas\,yr^{-1}}$ and $v_{z,\mathrm{SMC}} = 0.489 \pm 0.019\mathrm{mas\,yr^{-1}}$.

To determine the proper motions of the Clouds we select sources using the following procedure:

1. To create a filter, we initially select stars with $\rho = \sqrt{x^2+y^2} < \sin r_{\mathrm{sel}}$ ($r_{\mathrm{sel}} = 5^\circ$ for the LMC, $r_{\mathrm{sel}} = 3^\circ$ for the SMC) and $\varpi/\sigma_\varpi < 10$ (to minimise foreground contamination). We also select only stars with $G < 19$ in this step, to ensure that the spread in proper motion due to uncertainties is small compared to the difference between the the proper motion of the cloud and of the bulk of the foreground.

[4] 'Retrograde' here means negative spin about the LOS ($\omega_z < 0$), which means counter-clockwise as seen by the observer. In our notation the LMC has prograde rotation, i.e. positive spin about the LOS or clock-wise as seen by the observer. According to some conventions (e.g. for binary orbits) this would be regarded as retrograde.

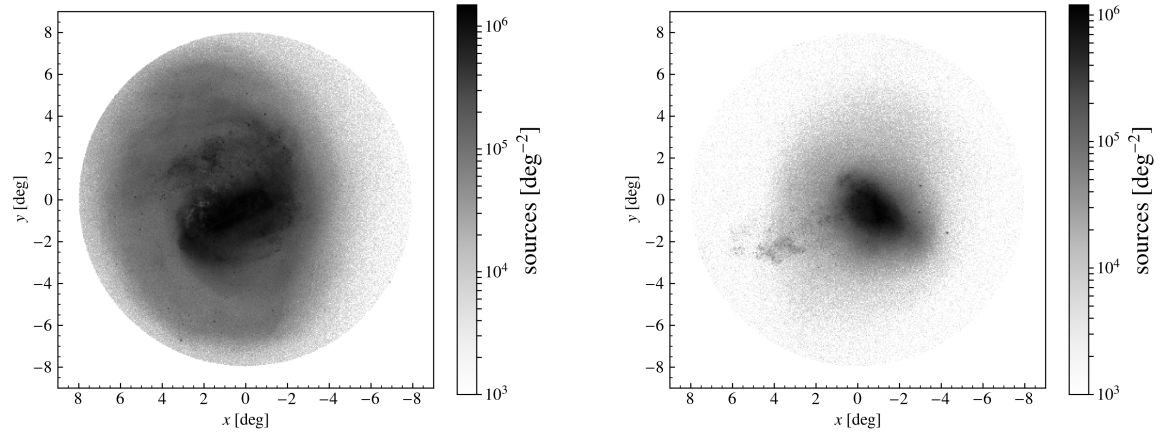


Fig. 5. Density distribution on the sky of the stars selected as members of the LMC (left) and SMC (right). Positions are shown in the (x, y) coordinates described in the text (Eqs. 2). Note that in all figures using this coordinate system the x-axis has been inverted, to correspond to the usual inversion of right ascension.

2. We determine the median proper motion of this sample, and do a preliminary filter on proper motion by removing any source where μ_x or μ_y lies more than 4 times the robust scatter estimate[5] of that proper motion component from the median.
3. We determine the covariance matrix of μ_x, μ_y for these stars, $\boldsymbol{\sigma}$, and use this to define a filter on proper motion, requiring that $\boldsymbol{\mu}^T \boldsymbol{\sigma}^{-1} \boldsymbol{\mu} < 9.21$ to correspond to a 99 percent confidence region.
4. We apply this filter in proper motion, along with that in ϖ, to all stars with $G < 20$ within 8 degrees of the assumed centre of LMC or SMC to get our complete sample.

We do two iterations of this procedure, first using expected μ_x, μ_y given the quoted $\mu_\alpha*$, μ_δ. This gives us a median parallax for the stars in the two Clouds: -19μas for the LMC, and -0.9μas for the SMC (compared to the expected values of $\sim 20\mu$as and $\sim 16\mu$as, respectively). This is consistent with the offset and variation reported in other sections of this paper, and in Arenou et al. (2018). We then repeat the procedure using the values of $\mu_\alpha*$, μ_δ implied by the data, conditional on the source's parallax taking this median value (taking into account the quoted uncertainties and correlations). This procedure leaves us with 8 million sources in the LMC and 1.4 million in the SMC.

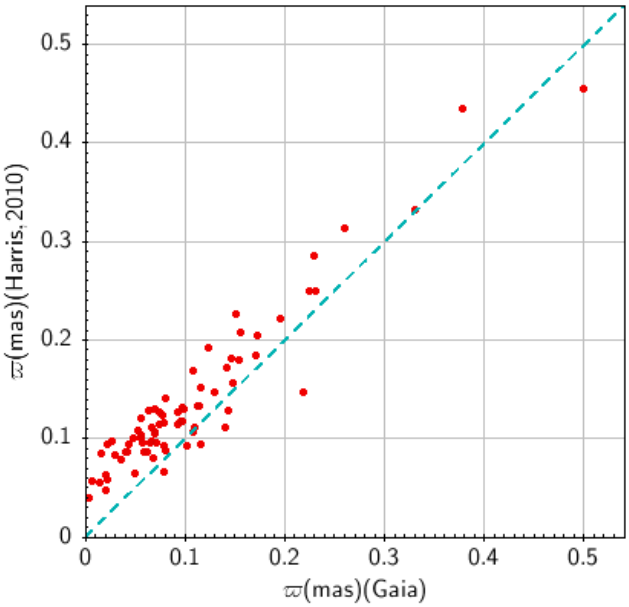


Fig. 6. Comparison between parallaxes as derived from the *Gaia* DR2 data and parallaxes derived from the cluster distances as given in Harris10.

3. Analysis: globular clusters

As described earlier, we have analysed 75 globular clusters, for which the data are presented in Table C.1. For each cluster we have derived the proper motion and parallax, and where data was available, the radial velocity.

3.1. First analysis and comparisons

Fig. 6 compares the parallaxes derived from the *Gaia* data to those from the cluster distances given in Harris10. There is a systematic difference of -0.029 mas (the *Gaia* parallaxes being smaller), originating largely from the *Gaia* data, and a calibration noise level around that relation of 0.025 mas (Arenou et al. 2018; Lindegren & et al. 2018). There is of course also a small contribution possible from the values given by Harris10. However, we have made a provisional check on these distance estimates using the *Gaia* photometric data by superimposing the HR diagrams for all the clusters using the distances and reddening values as presented in Harris10 (see Gaia Collaboration et al. 2018a). We found all the clusters fall neatly on top of each other for the critical elements (mainly the position of the blue horizontal branch). This indicates that, as a group, the distance moduli and colour corrections are confirmed to be in mutual agreement to better than 0.1 magnitude.

The standard uncertainties, which measure the precision rather than the accuracy, of the cluster-parallax determinations are smaller to very much smaller than the overall calibration

[5] The robust scatter estimate (RSE) is defined in terms of the 10th and 90th percentile values, P_{10} and P_{90} as RSE= $C \times (P_{90} - P_{10})$, where $C = \left(2\sqrt{2}\,\mathrm{erf}^{-1}(4/5)\right)^{-1} \approx 0.390152$. For a Gaussian distribution it is equal to the standard deviation.

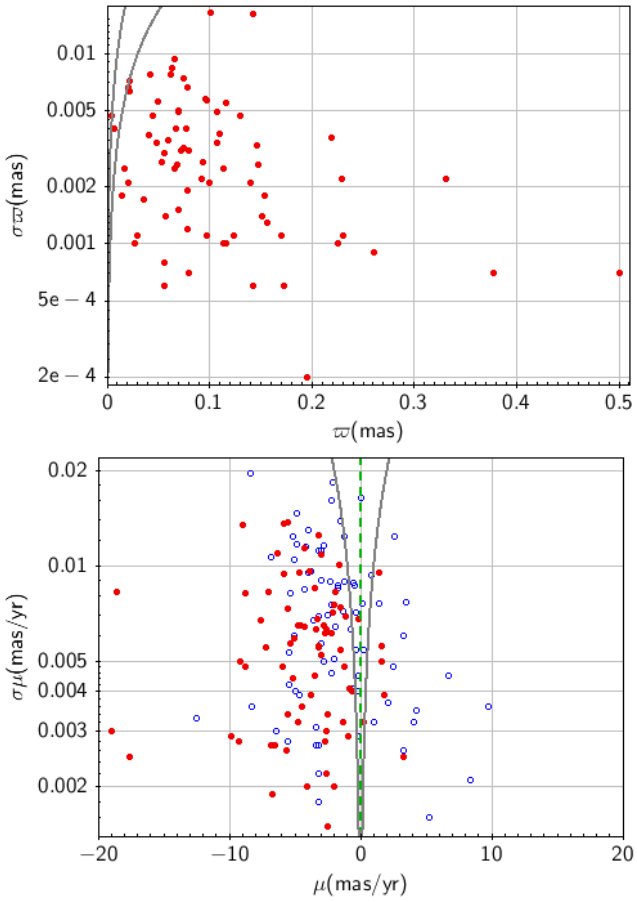


Fig. 7. *Top*: Parallax error against the *Gaia* parallax as determined from the *Gaia* data for 75 globular clusters. The black curves are the 1 and 3σ limits. The vertical dashed line corresponds to 3× our estimate of the systematic error on the parallax. *Bottom*: Proper motion errors against the proper motions in right ascension (open circles) and declination (solid circles) for the clusters in our sample. The curves represent the value of the PM for $100\sigma_{\mu}$. Only for NGC 6453 the PM measurement has significance lower than 10σ, for which $\mu_{\alpha*}/\sigma_{\mu_{\alpha*}} \sim 4$.

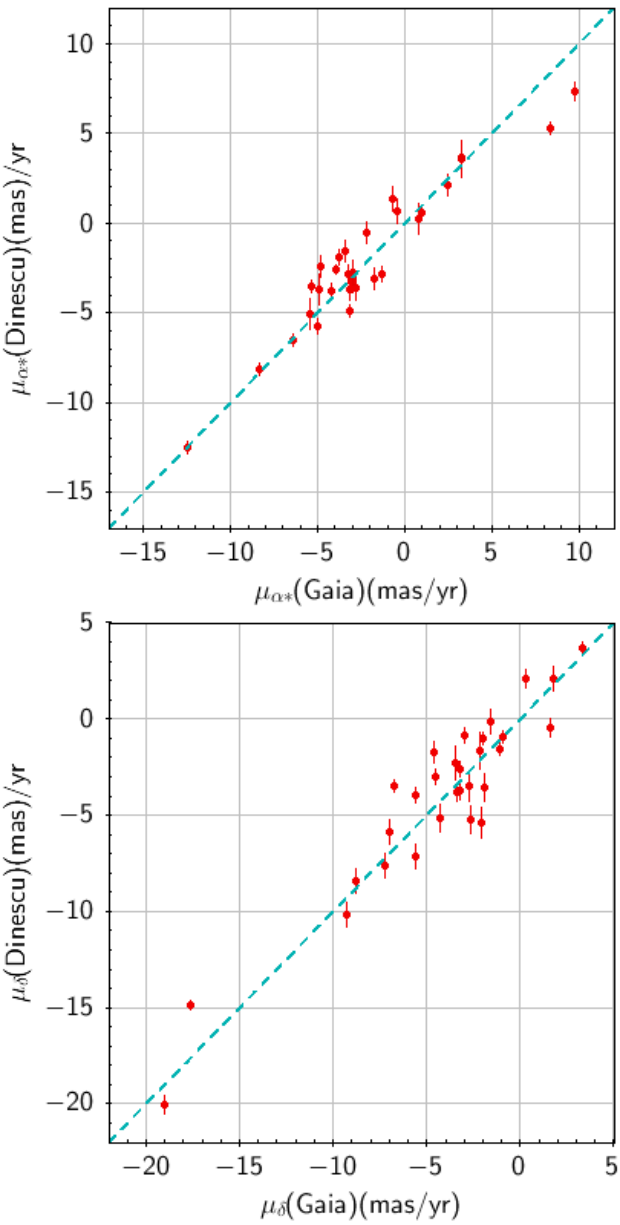


Fig. 8. Comparison of the *Gaia* proper motions (in right ascension: top, and declination: bottom) to measurements reported in Dinescu et al. (1999, 2003); Casetti-Dinescu et al. (2007, 2010, 2013) for 31 globular clusters.

noise level, as shown in the top panel of Fig. 7. The actual errors on those parallax determinations are therefore dominated by the overall *Gaia* calibration noise and offset in the parallax values. As discussed in depth in Lindegren & et al. (2018), these systematic errors are also apparent in the parallax distribution of QSOs (which reveal the same offset), and as we will show in Appendix A.2 also in the parallaxes of stars in the LMC (localised fluctuations) and other dSph, and are due to *Gaia*'s basic angle variation and scanning law. It is therefore expected that their amplitude will be significantly smaller in future *Gaia* data releases. For the time-being, and because the parallax uncertainties derived photometrically are smaller, we use the distances as given by Harris10 in the analyses that follow.

The observed proper motions are mostly about one to two orders of magnitude larger than the parallaxes, and thus the measurements are very robust and significant (see the bottom panel of Fig. 7). A comparison with a series of studies (Dinescu et al. 1999, 2003; Casetti-Dinescu et al. 2007, 2010, 2013) is shown in Fig. 8, and indicates overall good agreement, and most notably that the errors have been reduced by nearly two orders of magnitude. It remains, however, somewhat uncertain if the same calibration noise level can be assumed for the proper motions as for the parallax (but see e.g. Sec. 4.1). Nonetheless this systematic will be much smaller than the amplitude of the proper motions themselves.

Radial velocities as measured by *Gaia* (Cropper et al. 2018) are available for 57 of the 75 clusters, though for only 46 clusters there were 3 or more cluster stars with radial velocities measured. While future Gaia data releases will contain radial velocities for more of these sources, this highlights a need for dedicated high-precision spectroscopy of these clusters to properly complement the Gaia astrometry. Figure 9 shows a comparison between ground-based (from Harris10) and *Gaia* radial velocity measurements, indicating a good relation for clusters for which enough stars have spectroscopic measurements (darker points). The relation between the number of stars and the standard uncertainty on the mean cluster velocity indicates an average internal velocity dispersion of order 4 km s^{-1}. This estimate of the in-

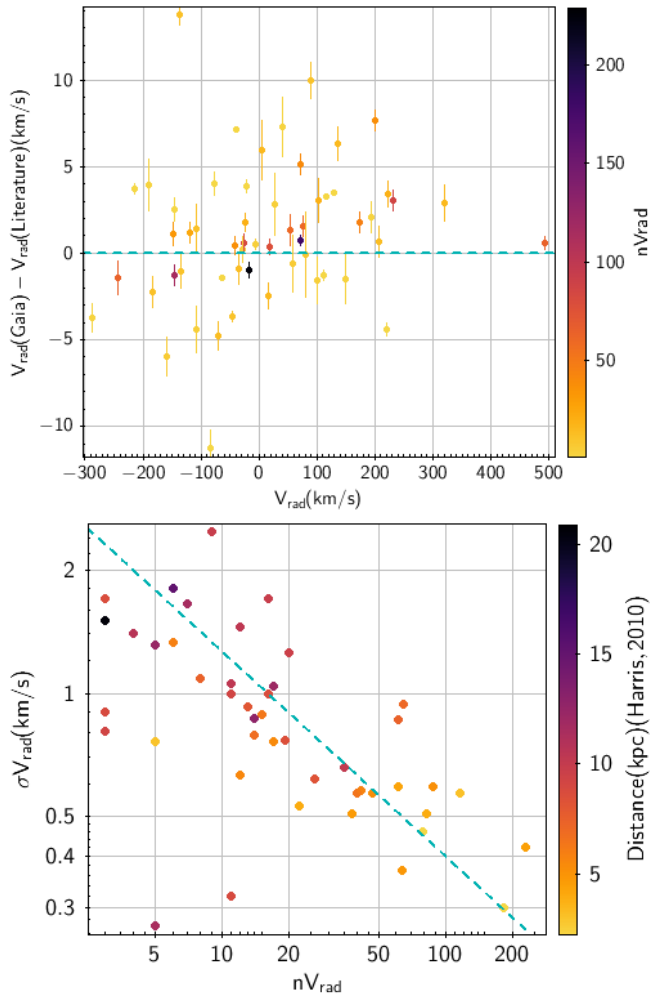


Fig. 9. *Top*: Comparison between the ground-based and *Gaia* radial velocities for 52 clusters with at least 2 measurements. *Bottom*: Standard uncertainties on the mean radial velocities as a function of the number of stars contributing to the mean. The diagonal line shows the effect of an additional contribution of 4 km s^{-1} originating from the internal velocity dispersion.

trinsic velocity dispersions is very similar to what is observed for the proper motions.

Fig. 10 shows the distribution on the sky of the globular clusters in our sample, where the arrows indicate the direction of motion and the colour-coding reflects the amplitude of the tangential velocities. These were derived using the proper motions listed in Table C.1 and the distances from Harris10.

3.2. Further results from the Globular Cluster astrometric data

The outstanding quality of the *Gaia* DR2 data, and the fact that the proper motions are presented within an absolute reference frame (free from expansion and rotation), has also allowed us to clearly detect rotation in 5 of the 75 globular clusters in our sample. For 3 of these clusters (NGC 104, NGC 5139, NGC 7078), this was already known (Bianchini et al. 2013), but we have also detected rotation in NGC 5904 and NGC 6656 (see e.g. the left panel of Fig. 11). An indication of rotation can also be observed in NGC 5272, NGC 6752 and NGC 6809. Similarly, *Gaia* data allows measuring expansion and contraction in globular clusters. For example NGC 3201 (Fig. 11, middle), shows very clear perspective contraction which is due to its very high radial velocity and relatively large parallax. From this we may determine the parallax of this cluster in the same way this used to be done for the nearby Hyades open cluster (see van Leeuwen 2009, and references therein). The *Gaia* data as presented here for the radial velocity and the proper motions thus provide a cluster parallax of 0.221 ± 0.0086 mas, at about 2σ from the value of 0.204 mas given by Harris10. Finally, for NGC 6397, a cluster considered to have been subject to core collapse, we can still see a signal of the expanding halo (Fig. 11, right), clearly different from the expected, very small, perspective contraction signal.

Furthermore, we find that our clusters have velocity dispersion profiles that decline with radius (Fig. A.5), and that several clusters show a slight increase in the outskirts, probably as the result of a halo of more loosely bound stars (as evidenced also by their spatial extent, see e.g. Olszewski et al. 2009; Carballo-Bello et al. 2012; Navin et al. 2016; Kuzma et al. 2018). This increase is found at a distance where contamination by field stars should not yet be important.

4. Analysis: dwarf spheroidal galaxies

The procedures described in Section 2.1 allow us to determine the mean proper motions of the dSph in our sample. As discussed earlier, we focus in this paper on the classical dSph, and have included in our sample one example of an ultra-faint galaxy, Bootes I. The resulting mean μ_α^* and μ_δ, as well as the astrometric parameters and uncertainties are listed in Table C.2.

The efficiency of our selection procedure in removing most of the foreground contamination becomes clear in Fig. 12. Stars surviving the proposed criteria are shown as cyan dots for each of the dwarfs, and they clearly clump in the diagrams much more strongly that the likely non-members (shown as black points). In this figure the blue ellipses indicate the contours corresponding to 3σ dispersion around the mean μ_α^* and μ_δ (σ is computed taking into account the covariances, using the standard error on the mean $\times \sqrt{N_*}$, where N_* is the number of stars used to measure the mean proper motions).

The possibility that the *Gaia* DR2 data provides of selecting members via their proper motion opens a new window for understanding the structure and extent of the dSph. In particular Fig. 2 shows that some of the dwarfs in our sample present spatial asymmetries (e.g. Fornax in the top right, Sculptor's outskirts appear somewhat boxy) while there is a hint of tidal streams in the case of the Carina dSph. A more detailed analysis of these features is beyond the scope of this paper but it is certainly warranted by the dataset.

4.1. Systematics, correlations and dispersion

Table C.2 shows that for several dSph the average parallax is negative[6]. This systematic error, similar to that found for the globular clusters and the Magellanic Clouds (and the QSOs Lindegren & et al. 2018), is present in the different fields, and its amplitude varies from object to object (for more details see Appendix A.2). The average offset, computed as the difference between the expected parallax (based on the distances from Mc-

[6] Since the parallax is a measured, unconstrained quantity with an associated measurement error, as the error increases (and especially for distant objects whose parallax is close to zero) the probability density function for the observed parallax will be increasingly covering negative values. A parallax zero point offset, as found in Gaia DR2, further affects this distribution.

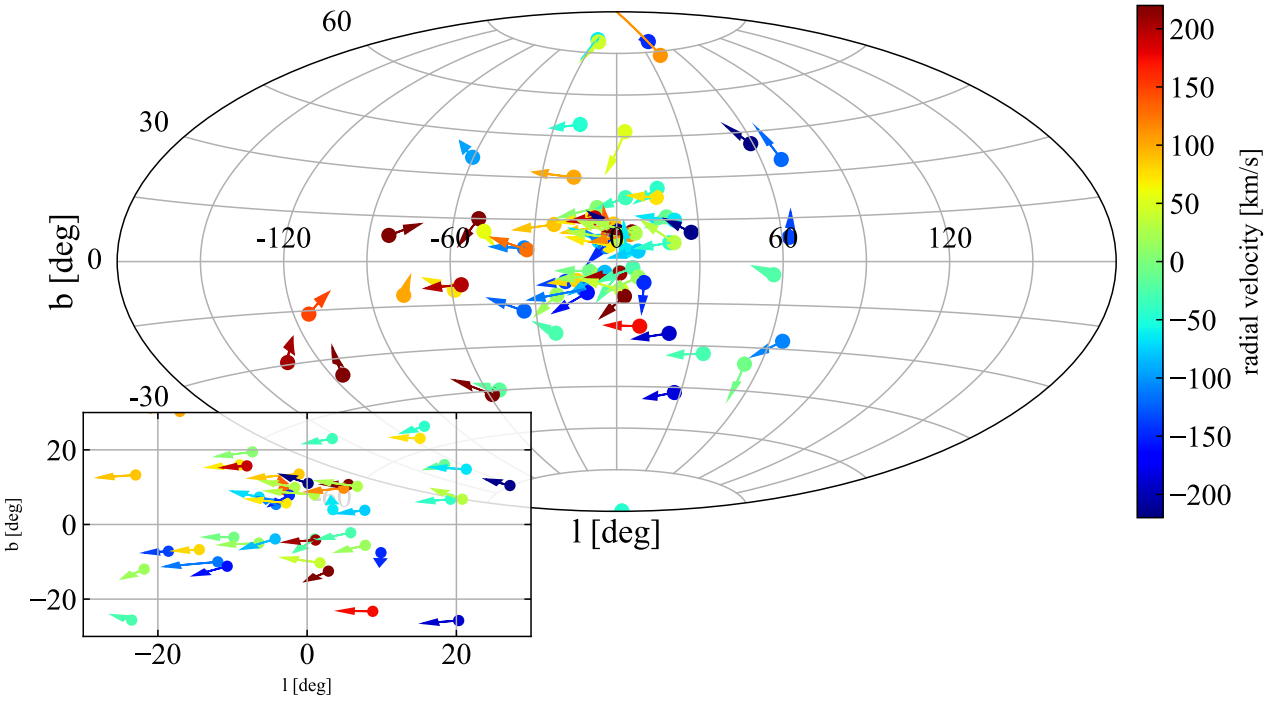


Fig. 10. Sky distribution of the 75 globular clusters in our sample in Galactic coordinates. Their tangential velocities are denoted by the size and direction of the arrows, while the colours indicate their line-of-sight velocities. The inset shows a zoom-in of the central 60×60 deg^2.

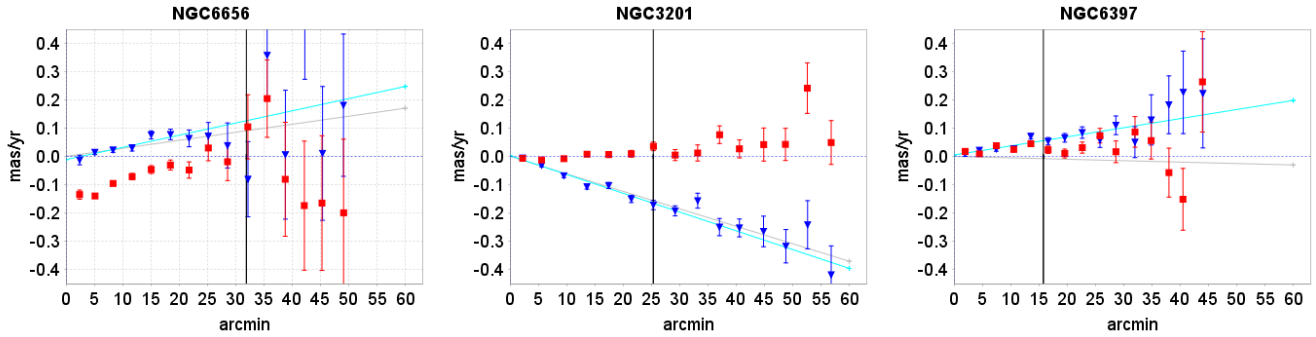


Fig. 11. Proper motion "systematics" in radial (blue triangles) and transverse (red squares) directions, as a function of distance to the cluster centre. The cyan-coloured line is a fit to the variation of the mean radial component of the proper motions as a function of distance, while the grey line is the expected trend resulting from perspective contraction or expansion. From left to right: NGC 6656, shows a strong rotation signal as well as perspective expansion; NGC 3201, shows no rotation but very strong perspective contraction; NGC 6397, shows halo expansion associated with core collapse, clearly different from the signal expected from the small perspective contraction. The vertical line indicates the tidal radius of the cluster reported in Harris10.

Connachie 2012), and the parallax from DR2 for all dSph, is −0.056 mas[7], while if Leo I is excluded it is −0.038 mas (for Leo I the parallax offset is −0.21 mas).

The proper motion maps shown in Fig. 12 reveal that the dwarfs are extended in PM space. The main contributor of this dispersion is not intrinsic but it is due to the uncertainties, which are typically very large. For example, for an object like Sculptor, the individual velocity errors for $G \sim 18$ mag stars are of order 80 km s^{-1}(while for $G \sim 20$, they are > 200 km s^{-1}), compared to the expected internal dispersion of order of 10 km s^{-1}. Therefore, measuring the intrinsic dispersion for these systems does not appear to be feasible with the data provided by DR2. However, it may begin to become feasible with later data releases, and certainly with an extension of the *Gaia* mission.

There is another effect affecting the measurements of the PM, which is related to the scans and varying astrometric incompleteness. These introduce a pattern in the parallax and PM field that is only readily apparent for sufficiently large objects on the sky (see also Arenou et al. 2018; Lindegren & et al. 2018). This is illustrated for the LMC and SMC in Figs. A.9 and 16, and it is also present for example for the Sgr dSph as shown in Figs. 2 and 13.

For sufficiently large objects on the sky, the banding pattern is averaged out, and the mean PM is more robust[8]. The global dispersion is however larger than expected just from random er-

[7] Arenou et al. (2018) report a comparable offset computed using an average over spectroscopically identified member stars of all the dSph simultaneously.

[8] Although there may still be a residual effect of ~0.028 mas yr^{-1} amplitude on scales of 10-20 degrees, as reported for the QSO's in Lindegren & et al. (2018).

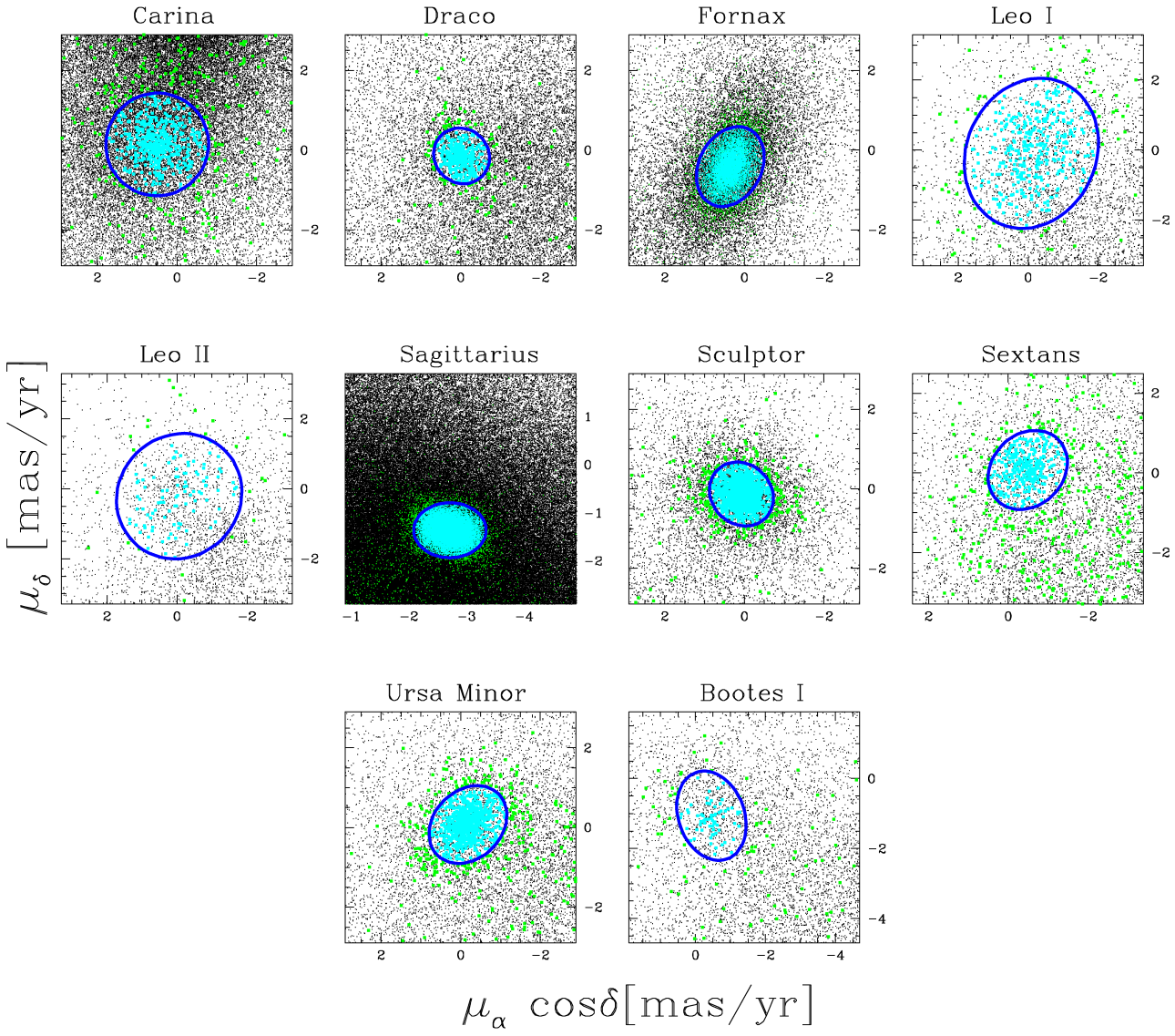


Fig. 12. Proper motions of the stars in the field-of-view towards the different dSph galaxies in our sample. Members, defined as stars within 3σ of the mean measured proper motion and located in the expected region of the CMD are shown in cyan. The green points correspond to stars which also fall in the CMD selected box, but are not within 3σ of the systemic PM. Note that especially for Sculptor and Fornax, it is quite clear that there may be more members, but quite likely the large errors on the proper motions of individual stars place these beyond the 3σ ellipse.

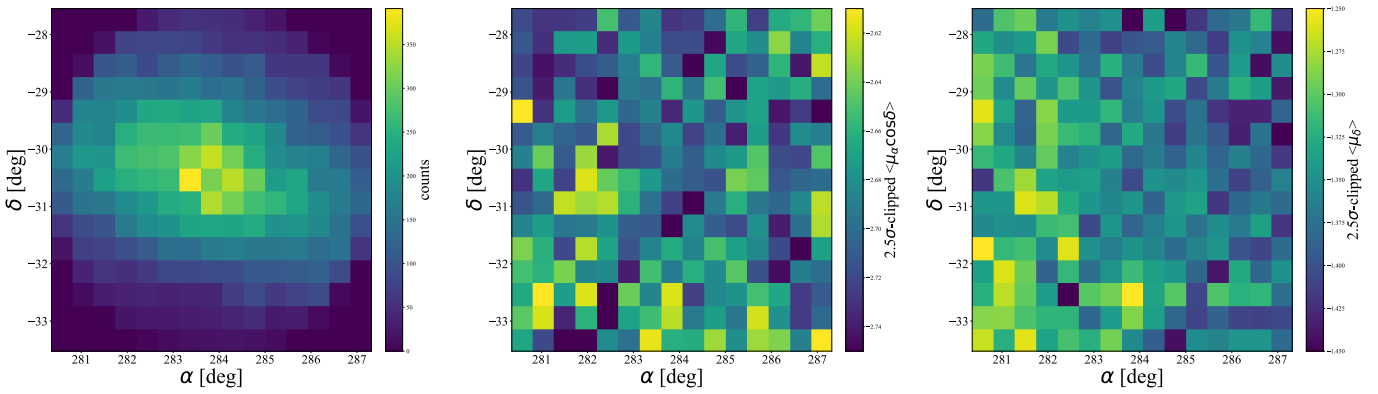


Fig. 13. Counts in 0.2 deg wide bins on the sky with at least 100 stars for stars in the Sagittarius dwarf (left) and the average PM in $\mu_{\alpha*}$ (middle) and μ_δ (right) for each of these bins.

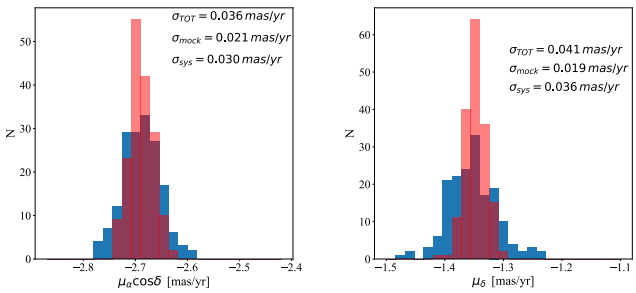


Fig. 14. The blue histograms show the distribution of average PM in the bins shown in Fig. 13 while the red histograms correspond to a model with the derived average PM convolved with the random errors provided by the astrometric solution. The difference shows the amplitude of the systematic on the mean value of the PM for a bin of this size.

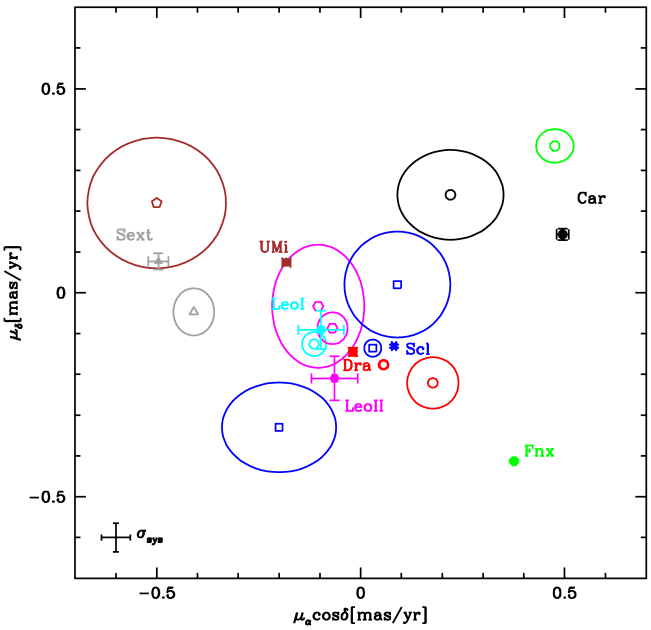


Fig. 15. Comparison to literature values of the proper motions of the dSph. Symbols with the same colour correspond to the same dSph, where filled symbols with error bars are those derived in this paper, and open symbols surrounded by ellipses correspond to the literature values. The error bars have the size of $\epsilon_{\mu_{\alpha*}}$ and ϵ_{μ_δ} as reported in Table C.2. The black cross in the bottom left corner indicates our estimate of the systematic uncertainty on the proper motions.

rors (because of the offset from bin to bin in the pattern). We quantify this effect in Fig. 14, where we show the distribution of the mean PM in α and δ computed in bins of 0.2×0.2 deg^2 size containing at least 100 stars[9] , and after 2.5σ clipping to remove outliers. The fact that the mean value changes from bin to bin is at least partly caused by the finite number of stars in each bin, as well as by the random errors. We try to estimate the residual systematic error by modelling this distribution assuming the mean proper motion derived using all member stars, and assuming the errors are Gaussian. We draw for each star a new PM from this mean and assuming its quoted uncertainty and correlations and recompute the mean using all the stars in the bin (we also assume an intrinsic velocity dispersion of 10 km s^{-1}). This is the red histogram in Fig. 14. Clearly the observed distribution is wider (blue), and the difference between the two can be used to compute the systematic error as: $\sigma^2_{mock} + \sigma^2_{sys} = \sigma^2_{tot}$. We find this to be $\sigma_{sys} \sim 0.030$ mas yr^{-1}and ~ 0.036 mas yr^{-1}in the right ascension and declination directions, respectively. These values are of slightly smaller amplitude than those derived by Lindegren & et al. (2018) from a sample of QSOs.

For systems that are smaller on the sky, and in particular for those that would fall in a single bin, their PM may be offset by this much. Objects like the larger dSph such as Fornax, Sculptor, etc, are likely not affected by this systematic (because it averages out), but for systems such as Leo II, they should be considered. In our subsequent analyses we thus consider the amplitude of the systematic uncertainty to be 0.035 mas yr^{-1}. As can be seen from Table C.2 in many cases this systematic error is larger than the random error on the measurement of the mean proper motion of a dSph.

Table C.2 also shows that there are strong correlations in the different mean astrometric parameters derived for the dSph in our sample. These correlations vary from object to object in amplitude and direction (see Appendix A.2), and it is important to take them into account in the derivation of e.g. the orbital parameters.

4.2. Comparison to the literature

We have compared the PM derived with our selection criteria and those obtained if we were to use only stars identified as members from publicly available radial velocity catalogues (from Armandroff et al. 1995; Kleyna et al. 2002; Muñoz et al. 2006; Battaglia et al. 2006, 2011; Sohn et al. 2007; Mateo et al. 2008; Walker et al. 2009, 2015). We have found very good agreement (i.e. the estimates differ by less than 1σ, see Arenou et al. 2018). The main disadvantage of using external information is its heterogeneous nature. Furthermore this information is not available for all the dSph in our sample, and typically the sample of stars with radial velocities for any given dSph is smaller by a factor $\sim$ 2 than found with our selection and analysis based exclusively on *Gaia* DR2 data, even down to the same magnitude limit.

Figure 15 compares our measurements of the PM of the dSph to astrometrically derived values reported in the literature. These are from Piatek et al. (2003, 2004) for Carina; for Draco: Pryor et al. (2015); Sohn et al. (2017); Piatek et al. (2005) for Ursa Minor; for Sculptor: Piatek et al. (2006); Sohn et al. (2017); Massari et al. (2018); Piatek et al. (2007) for Fornax; for Leo II: Lépine et al. (2011); Piatek et al. (2016); for Leo I, Sohn et al. (2013) and for Sextans, Casetti-Dinescu et al. (2018). Most of these measurements were obtained from space, except for Sextans which is based on Subaru imaging. We have excluded measurements for Sgr and Bootes I for visualisation purposes (as their proper motions are much larger than for the other, more distant dSph).

A striking difference between previous estimates of the dSph PM and those obtained using *Gaia* DR2 data is the extent of the error bars, particularly for the objects where more than 400 (and upto several thousands) astrometric members have been identified, such as for Carina, Ursa Minor, Fornax, Sculptor and Draco. In many cases, our measured proper motions are consistent with the literature values at the 2σ level (given the large error bars of the latter). For the most recent astrometric measurements with HST (and hence typically based on a larger baseline), the values appear to be closer and consistent with each other (e.g. Leo I), especially if the systematic uncertainties are taken into account (e.g. Sculptor, Draco). Fornax is a notable exception, as we find

[9] We consider 0.2 deg bins because this is the smallest angular size of a dSph in our sample.

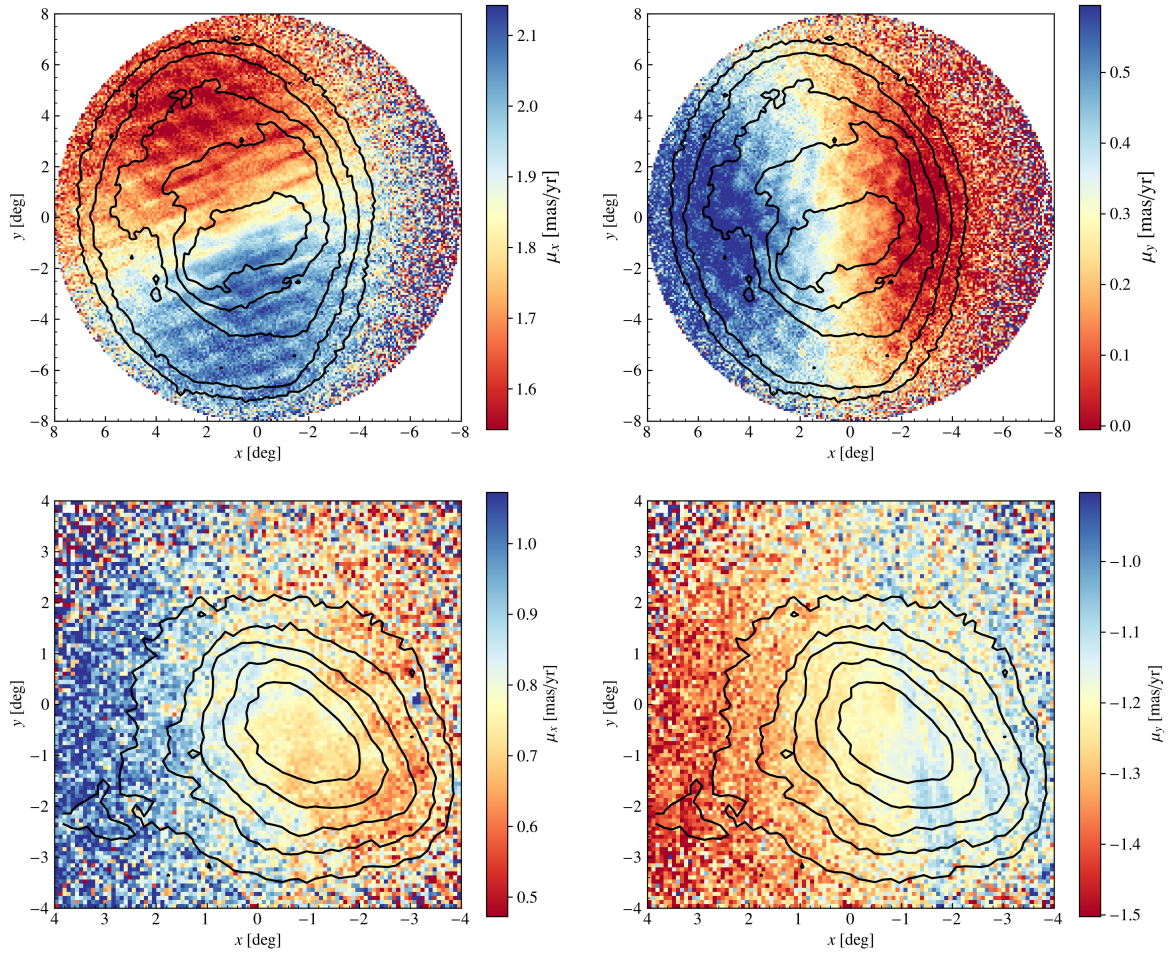


Fig. 16. Proper motions of stars in the LMC (upper) and SMC (lower) showing the components μ_x (left) and μ_y (right) components, which are as described in the text (Eqs 3). The colour shows the median proper motion in each pixel (after filtering). The black density contours are logarithmically spaced, such that the outermost contour is at a source density 100 times smaller than the highest density. Note that the centre of each colour bar is chosen to be the median proper motion of all sources. This is not the same as the proper motion derived for the clouds below, because the sources are not distributed symmetrically around the assumed dynamical centre – the photometric and dynamical (from the HI disc) centres are offset from one another. Trends in proper motion, particularly that associated with rotation in the LMC are clearly visible. The banding associated with *Gaia* 's scanning law, and as seen in the parallaxes, can also be seen.

a very different PM than reported before. In the case of Sgr, we find that the *Gaia* DR2 PM is consistent with that of Massari et al. (2013) although it is now much more accurate. Note that we present here the first measurement of the PM of the UFD Bootes I.

5. Analysis: LMC and SMC

5.1. Basic analysis

In Figure 16 we show the median proper motion, in the x, y coordinate system defined in Section 2.2, of sources that meet our membership criteria for the LMC and SMC, binned by position on the sky. This is a demonstration of the extraordinary precision of the *Gaia* proper motion measurements (see also Figure 24). The signature of rotation is clearly visible in the LMC, and trends in the proper motions of stars in the SMC can also be seen. Figure 16 serves as a demonstration of the shortcomings of this data release as well. The 'banding' or striping of the proper motions that we have discussed before, associated with different scans and investigated by Lindegren & et al. (2018), is also clearly visible. This can also be seen in the parallaxes (Figure A.9).

We can characterise the trends seen in Figure 16, to first order, by the central values and gradients. We calculate these either directly as a least squares fit to the data, or as a least squares fit to the median proper motions calculated in 0.°04-by-0.°04 bins in x,y plane. This latter fit is performed to reflect the fact that the most important errors in this analysis are systematic, and depend on position on the sky, but it does become less appropriate towards larger radii as Poisson noise becomes more important. The differences between the values derived using these two methods give a sense of the scale of the uncertainty associated with the position-dependant systematic errors.

In Tables B.1 & B.2 we show the central values and gradients (Eqs. 3) for the proper motions. We provide values for all sources within various angular radii (i.e. $\rho = \sin^{-1}(x^2 + y^2)^{1/2} < \rho_{\rm max}$), and for annuli. For both the LMC and SMC we show the values of i, Ω, ω found when we perform a least-squares fit to the derived gradients under the assumption that v_z takes the value implied by the known values of the line-of-sight velocity and distance to the Clouds. The results are reasonably consistent with

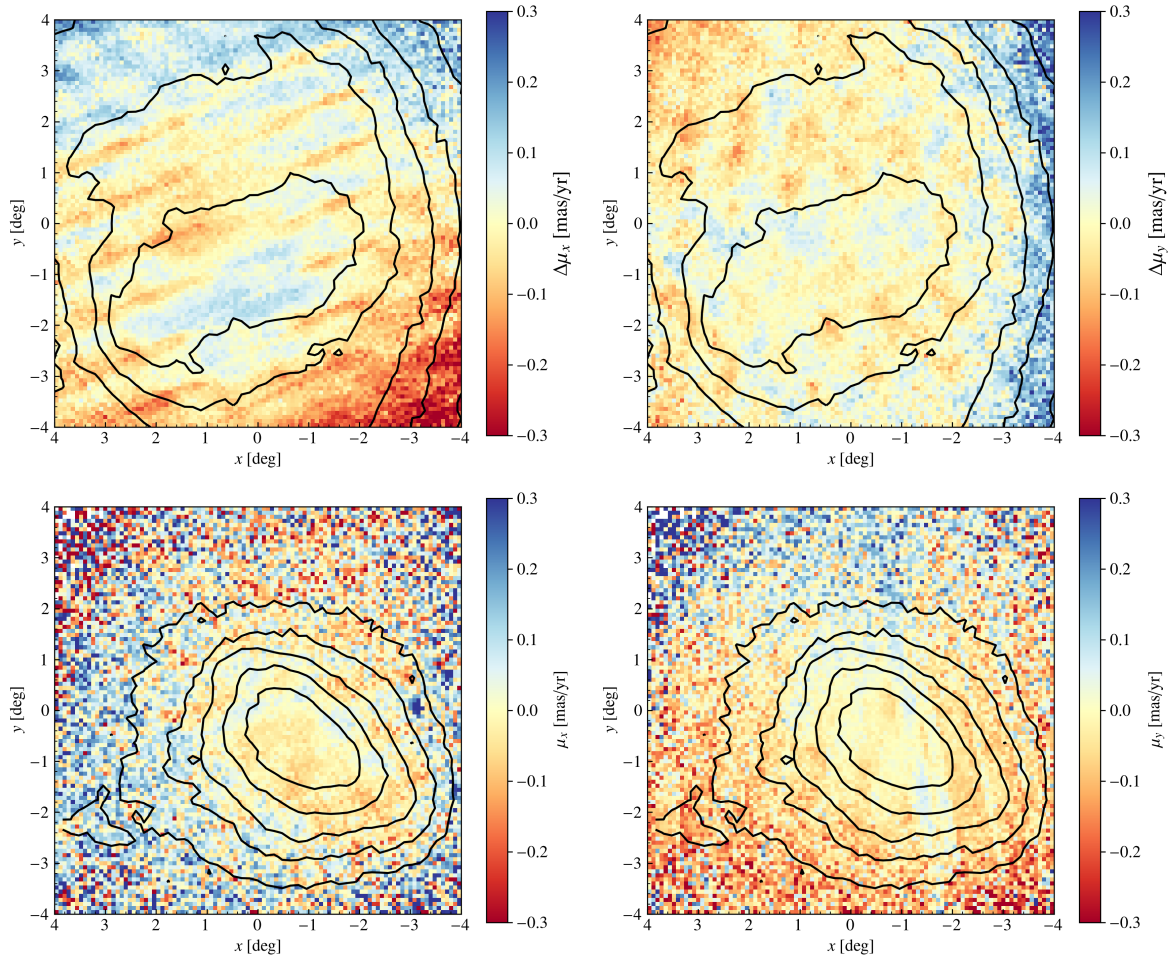


Fig. 17. Residual proper motion, after subtraction of a model proper motion field. In both cases the majority of the variation disappears, and the banding in proper motion is more clearly visible. Black density contours are spaced as in Figure 16. For the LMC, the imprint of orbits in the bar can be seen as the bluer area on the lower side of the bar (as it appears in the plot) and the redder area on the upper side of the bar. The model that is subtracted off is fit from sources within angular radii $\rho_{\rm max} = 3^\circ$ of the centre for the LMC, and $\rho_{\rm max} = 2^\circ$ of the centre for the SMC.

one another (allowing for the fact that we expect ω to decrease as we look farther out).

For the LMC we also give the implied values of v_z, i, Ω, ω if we place no constraint on the line-of-sight velocity. The value of v_z that this implies is of the order 1.3-2.0 mas yr^{-1}, which is similar to (but somewhat larger than) the value 1.104±0.057 mas yr^{-1} that is expected given the measured line-of-sight velocity and distance of the LMC. The effect of the line-of-sight velocity of the Clouds is to produce a perspective shrinking of the Cloud on the sky (a negative contribution to both $\partial\mu_x/\partial x$ and $\partial\mu_y/\partial y$ in Eq. 3), akin to the effect seen in NGC6656 or NGC3201 (Figure 11). It may be that the mismatch between the value derived from *Gaia* astrometry and that found from spectroscopy is related to an actual contraction of the LMC disc (akin to the apparent expansion of NGC6397 in Figure 11). However the orientation of the LMC disc also plays an important role in these values, and the values of i derived when v_z for the LMC is fixed lie closer to those found in photometric studies, which tend to be in the range $25 - 40^\circ$.

For the SMC, directly inverting Eqs. 3 gives line-of-sight velocities which are completely inconsistent with those measured by from spectroscopy (~ -0.8 mas yr^{-1} as opposed to 0.489 ± 0.019 mas yr^{-1}). This may be due to the inadequacy of modelling the SMC as a flat disc, or a real expansion of the SMC (which, again, is degenerate with line-of-sight motion). However, forcing v_z to take the value expected from the measured distance to the SMC and its line-of-sight velocity gives us a model which has a disc inclination $\sim 74^\circ$, which is broadly similar to that measured for the Cepheid population ($64\overset{\circ}{.}4 \pm 0\overset{\circ}{.}7$: Subramanian & Subramaniam 2015).

In Figure 17 we show the residual proper motions after we subtract off a gradient in proper motion corresponding to our first order approximation with the parameters v_z, i, Ω, ω found for sources within angular radii $\rho_{\rm max} = 3^\circ$ of the centre for the LMC, and $\rho_{\rm max} = 2^\circ$ of the centre for the SMC. This shows more clearly the scale of the spatially correlated errors in proper motion, and in Figure A.10 we show the variation in 1D-stripes across the LMC (as well as the variation of the parallaxes), to allow for easier quantification. The residuals are comparable to those found in Section 4.1. The residuals in the centre are rather small, but become larger far from the centre for the LMC, in the opposite sense to the variation from the median shown in Figure 16. This is because of our assumption of constant ω, which breaks down badly at large radii, as the rotation curve becomes flat.

Figure 17 shows hints of the impact of the LMC's bar on the kinematics of the disc. The residual proper motion near the upper (as we see it) side of the bar tend to be negative while those on the lower side tend to be positive. This indicates that the stars are moving at faster-than-circular velocities at these points – this

is consistent with stars belonging to the x1 orbit family which is elongated along the bar (Contopoulos & Papayannopoulos 1980).

5.1.1. Uncertainties and comparison to the literature

The uncertainties on the measurement of the centre-of-mass motion of the LMC and SMC using *Gaia* data are completely dominated by systematic, rather than random, uncertainties. The estimates of these quantities that we show in Tables B.1 & B.2 are consistent to around the 10 μas level. This is smaller than the systematic uncertainty on proper motions calculated in section 4 or that on a large scale (of a few tens of degrees) derived from the proper motions of quasars observed by *Gaia* (Lindegren & et al. 2018), which is $\sim$ 28 μas yr^{-1} in each component. There is no clear choice of the 'right' values to take from Tables B.1 & B.2. However we can note that the approximation of constant angular velocity becomes poor for the LMC beyond about 3°, and that the density of stars in the SMC is small beyond a similar radius, so this appears to be a sensible choice. We therefore adopt the values found using all stars within these radii as our best estimates. These are $(\mu_{\alpha*,0,\mathrm{LMC}}, \mu_{\delta,0,\mathrm{LMC}}) = (1.850\pm0.030, 0.234\pm0.030)$ mas yr^{-1} and $(\mu_{\alpha*,0,\mathrm{SMC}}, \mu_{\delta,0,\mathrm{SMC}}) = (0.797 \pm 0.030, -1.220 \pm 0.030)$ mas yr^{-1}, where our uncertainty is estimated from the $\sim$ 10 μas yr^{-1} variation seen in Tables B.1 & B.2 and the $\sim$ 28 μas yr^{-1} large scale systematic uncertainty.

Kallivayalil et al. (2013) give an overview of recent estimates of the proper motions of the LMC and SMC, including their own, found using HST 3-epoch astrometry. Our estimates are consistent with theirs and with almost all of the values they cite, as well as the values found by van der Marel & Sahlmann (2016) using proper motions found from the Tycho-*Gaia* Astrometric Solution (Gaia Collaboration et al. 2016; Lindegren et al. 2016), which were $(1.872 \pm 0.045, 0.224 \pm 0.054)$ mas yr^{-1} and $(0.874 \pm 0.066, -1.229 \pm 0.047)$ mas yr^{-1} for the LMC and SMC respectively.

It is worth noting that the measured centre-of-mass proper motion is dependant on the chosen (or derived) centre of the Clouds. The centre of the HI gas disc of the LMC, which we assume to be the dynamical centre of the Cloud, is close to, but not exactly the same as, the centre that was derived from HST proper motions by van der Marel & Kallivayalil (2014), which was that assumed by Kallivayalil et al. (2013) and van der Marel & Sahlmann (2016).

We could, instead of assuming the stars' dynamical centres lie at the dynamical centre of the HI gas disc in each case, assume they lie at the photometric centres of the Clouds at, respectively, $(\alpha_{C,LMC,\mathrm{phot}}, \delta_{C,LMC,\mathrm{phot}}) = (81.^\circ28, -69.^\circ78)$ (van der Marel 2001) and $(\alpha_{C,SMC,\mathrm{phot}}, \delta_{C,SMC,\mathrm{phot}}) = (12.^\circ80, -73.^\circ15)$ (Cioni et al. 2000a). If we do so we derive mean proper motions $(\mu_{\alpha*,0,\mathrm{phot,LMC}}, \mu_{\delta,0,\mathrm{phot,LMC}}) = (1.890, 0.314)$ mas yr^{-1} and $(\mu_{\alpha*,0,\mathrm{phot,SMC}}, \mu_{\delta,0,\mathrm{phot,SMC}}) = (0.685, -1.230)$ mas yr^{-1}. This is, therefore, a larger variation than that due to the large scale systematic uncertainties.

Our uncertainties, including systematics, are comparable with those of previous studies. It is the sheer number of sources, spread across the Clouds, for which *Gaia* provides accurate proper motions that is so extraordinary, and this will allow astronomers using DR2 to make a detailed mapping of the dynamics of the Magellanic Clouds.

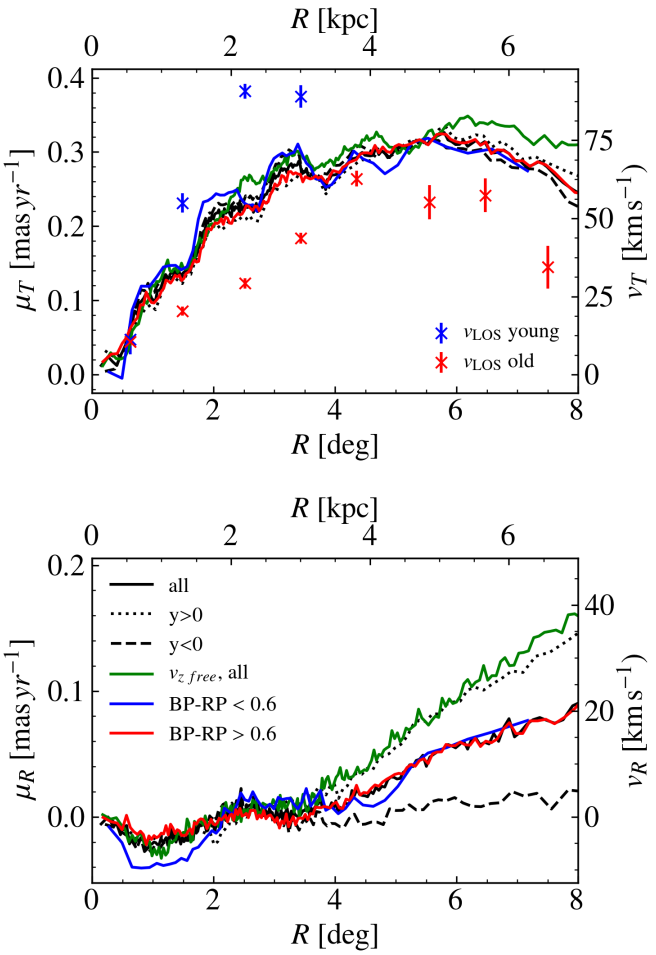


Fig. 18. Rotation curve (top) and median v_R (bottom) of the LMC. The assumed values for the centre-of-mass velocity and orientation of the disc (i and Ω) are taken from a fit to all stars within angular radii $\rho < 3^\circ$ of the LMC's centre. Angular distances and velocities given on the lower and left axes have been converted to real-space values on the upper and right axes assuming a distance to the LMC of 50.1kpc (Freedman et al. 2001). The points shown in the upper panel are derived from observed line-of-sight velocities of old and young stars by van der Marel & Kallivayalil (2014, their table 4)

5.2. Rotation curve

If we assume that we know the orientation of the LMC (or SMC), and that the motions we see are confined to the plane, it is possible to de-project the observed motions (minus the bulk motion) on to that plane. In appendix B we give the mathematical details of how this is performed. The SMC is less suitable for approximation as a simple flat rotating disc than the LMC, so we do not attempt that here. Tentative evidence that there is some sense of rotation of the SMC's stars is provided by the consistent, but small, measurement of ω for different annuli of stars shown in Table B.2.

In Figure 18 we show the resulting median tangential velocity, v_T (the rotation curve) and median v_R as a function of de-projected radius R for the LMC (note that R, v_R and v_T are de-projected position and velocity, i.e. in the plane of the LMC), with v_x, v_y, i, Ω as determined from a least-squares fit to the filtered data for angular radii $\rho < 3^\circ$, holding v_z fixed. The figures show the median value of v_T (or v_R) as we increase R, in non-overlapping bins of 40 000 sources. In both cases we also

divide the sample into sources with $y > 0$ and $y < 0$ as a consistency check. We also show the velocity curve derived from line-of-sight velocities by van der Marel & Kallivayalil (2014), separately for young and old stars. This shows that the precision of the proper motion rotation curve from *Gaia* is competitive with those in line-of-sight velocity curves (and are derived from many orders of magnitudes more sources). The *Gaia* data contains both old and young stars, so it is unsurprising that the *Gaia* rotation curve lies between the two from the old and the young populations.

The rotation curve for the LMC rises approximately linearly for $R \lesssim 3°$ (which provides post-hoc motivation for us choosing stars within projected angular radius ρ of 3° to determine the other parameters of the disc – it is over this radius that the assumption of constant ω is reasonable). The dense coverage of the LMC provided by *Gaia* allows us to resolve this rise in the rotation curve in a way that was not possible with the relatively sparse coverage provided by HST (van der Marel & Kallivayalil 2014). The scale over which the rise occurs is closer to that found for the old stellar population using line-of-sight velocities by van der Marel & Kallivayalil (2014). We also show the rotation curve that we derive when we allow v_z to vary freely, which is broadly similar.

As a further sanity check we divide the sources into blue and red bins, with the division at $G_{\rm BP} - G_{\rm RP} = 0.6$, and plot the rotation curve in each case. As one would expect, the blue stars tend to have a higher rotation velocity out to about 4°, by about $5 - 10\,{\rm km\,s^{-1}}$, reflecting lower asymmetric drift.

The v_R plot is rather harder to interpret. It is pleasingly close to 0 km s^{-1} in the inner regions, and the variation we see at projected radii $< 2°$ may well be related to the effect of the bar. In the outer regions there is a significant difference between the trends seen at positive and negative y-values, which is not seen in the rotation curve. It may be that this is due to non-equilibrium effects, possibly due to the past interaction of the LMC and SMC (e.g. Besla et al. 2016), but further interpretation goes beyond the scope of this paper.

6. Orbital Integrations

In this section we present the results of the orbital integrations for the globular clusters in our sample and for the dSph. For the Magellanic Clouds we do not perform integrations as this would require consideration of dynamical friction which introduces extra degrees of freedom such as for example, the total mass of each Cloud (e.g. Kallivayalil et al. 2013). For each object we integrate an ensemble of 1000 orbits whose initial conditions are drawn via Monte Carlo sampling the measurements and their uncertainties given in Tables C.1 and C.2 (i.e. we use the full covariance matrix and assume Gaussian errors). We produce two sets of Monte Carlo samples, considering only the random error on the observables, and considering in addition a systematic error of amplitude 0.035 mas yr^{-1}(as estimated in Sec. 4.1) for each proper motion component. We then transform these coordinates into Cartesian positions and velocities. Because currently our *Gaia* parallaxes (or distances) have larger (systematic) uncertainties than measurements available in the literature (see Sec. 3 and 4), we use published values from Harris10 and McConnachie (2012), for the globular clusters and the dSph respectively. The radial velocities used are also from these databases. For the distance errors, we assume an uncertainty in the distance modulus of ~ 0.05 mag, that corresponds to a relative distance error of ~ 0.023.

The initial conditions for the orbit integrations are listed in Tables C.3 and C.4 for the globular clusters and the dwarfs respectively. Note that in these Tables we give the uncertainty of the positions and velocities derived from the 16th and and 84th quantiles (which would be a 1σ deviation if the distributions were Gaussian), and which were obtained by marginalising over the other coordinates. However, as started earlier, in the orbit integrations we take into account the full covariance matrix. We consider three different Galactic potentials (labelled Model-1, -2 and -3) for the orbital integrations, and each of these potentials corresponds to a model previously published in the literature. Our goal is to understand how different their predictions are, as well as how robust are the conclusions. In the near future, it will be possible to use the data to constrain the model parameters and to understand which model performs best, for example by imposing self-consistency, but this exercise is beyond the scope of this paper.

Because each potential has its own set of characteristic parameters whose values have been derived by fitting different observables, they each assume different values for the position of the Sun and its peculiar velocity as well as for the motion of the Local Standard of Rest. That implies for example, that the angular momentum of the dwarf galaxies and globular clusters can be slightly different for the various potentials considered.

6.1. Description of the Galactic potentials used

The gravitational potential in Model-1 is axisymmetric, consisting of a stellar bulge and discs (which have a combined stellar mass of $5.4 \times 10^{10}\,{\rm M}_\odot$), two gas discs (with a combined mass of $1.2 \times 10^{10}\,{\rm M}_\odot$) and a Navarro, Frenk, & White (1996) dark matter halo. The virial mass is $1.37 \times 10^{12}\,{\rm M}_\odot$. The model is that found using a Bayesian analysis of kinematic tracers by McMillan (2017, c.f. their table 3).

The Model-2 gravitational potential is axisymmetric, consists of a stellar bulge and disc modelled as Miyamoto-Nagai potentials (which have a combined stellar mass of $7.55 \times 10^{10}\,{\rm M}_\odot$), and a spherical dark matter halo. The mass at $R < 200$ kpc is $1.9 \times 10^{12}\,{\rm M}_\odot$. The model is the one of Allen & Santillan (1991) but with revised parameters from Irrgang et al. (2013, their Table 1).

The third potential we consider (Model-3) is the non-axisymmetric mass model described in Robin et al. (2003, 2012). The properties of the axisymmetric components (thin and thick stellar discs, stellar halo, interstellar matter disc, dark matter halo) are described in Robin et al. (2003), while those of the rotating non-axisymmetric bar, renormalized to have a total mass of $6.7 \times 10^9\,{\rm M}_\odot$, are described in Robin et al. (2012). The mass of the Galaxy for $R < 100$ kpc is $\sim 1.2 \times 10^{12}\,{\rm M}_\odot$. The computation of the potential is described in Bienayme et al. (1987) for the axisymmetric components and in Fernandez et al. (2018, in prep) for the bar and halo components.

The three potentials have very similar mass distributions between ~ 3 and 40 kpc as measured by the circular velocity curves (shown in Figure D.1 of the Appendix). However the potentials differ substantially both in the inner as well as in the outer regions. This will lead to some differences in the orbits and their characteristics as we will see below.

6.2. Results for the globular clusters

Fig. 19 shows some examples of orbits for the globular clusters integrated backward in time for 0.25 Gyr. We have plot-

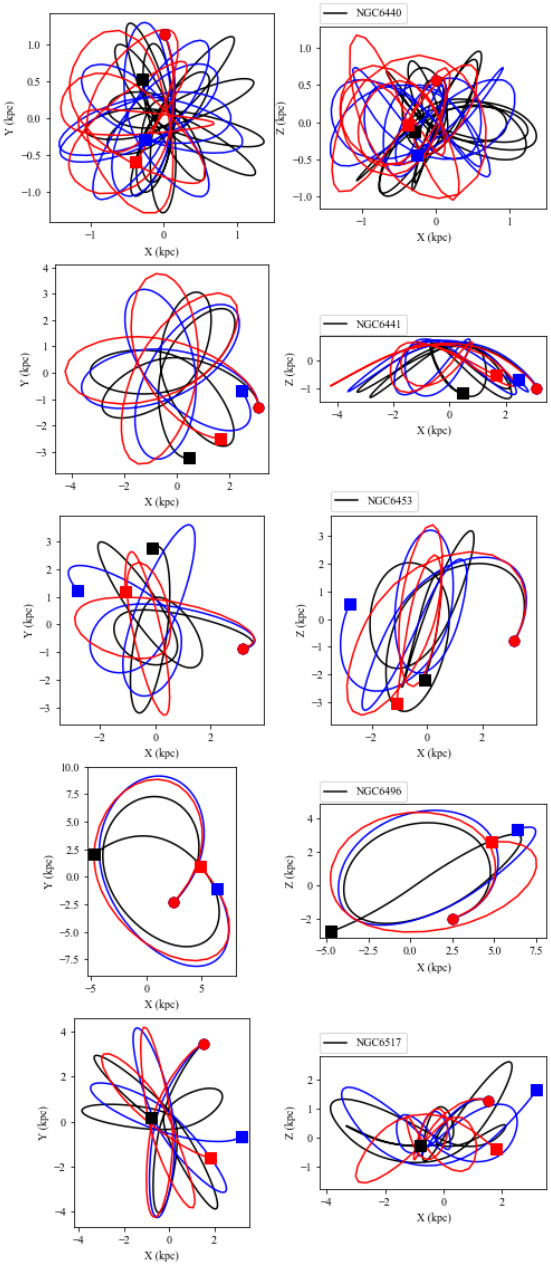


Fig. 19. Examples of the orbits of some of the globular clusters in our sample. The different colours correspond to the different potentials: Model-1 (based on McMillan 2017, in blue), Model-2 (based on Allen & Santillan 1991, in black), and Model-3 (based on Robin et al. 2003, 2012, in red). The orbits of clusters that remain in the inner few kpc are quite different for the various potentials, while as expected, the differences are much smaller for those that have pericentres greater than ∼ 2 kpc (e.g. NGC6496, 4th row). In such cases the location of streams, if present, can be predicted much more robustly.

ted in different colours the results obtained using the different Galactic potentials: Model-1 (blue), -2 (black) and -3 (red). For all the clusters, the orbits are very similar initially (at least for one orbital period), but they then begin to diverge reflecting the differences in the Galactic potentials used (see also Fig. D.2). Particularly large are the differences for clusters that penetrate the regions dominated by the bar, which is modelled as a non-axisymmetric component in Model-3 but not in Models 1 and 2. Furthermore, some clusters appear to be on resonant orbits, and interestingly as shown in the second panel of Fig. 19 for NGC 6441, this is true for the three potentials. A quick exploration reveals that several other clusters appear to be on similar types of resonant orbits. Some clusters, on the other hand, seem to be on chaotic orbits but further analysis is required to establish this robustly.

The distribution of some of the orbital parameters for the globular clusters in our sample is shown in Fig. 20 and summarised in Table D.1. In these plots, the solid circles show the median value of the time-averages over 10 Gyr of integration, while the error bars correspond to the 16th and 84th percentiles derived using only the statistical (and not the systematic) errors on the observables. These figures show that the orbits of globular clusters in our sample are very centrally concentrated as most have their orbital apocentres within 10 kpc. Most of our clusters are on prograde orbits, and a small fraction are retrograde. Recall this is a sample focused on the inner 20 kpc, so we cannot establish with this dataset whether this is also the case for the outer halo clusters. The clusters with the highest L_z are NGC 3201 (retrograde) and NGC 4590 (prograde) are not shown in this figure, nor is NCG 5466 because of its large apocentre (∼ 50 kpc).

In Fig. 20 the eccentricity is defined as the time-average of $(r_{apo} - r_{peri})/(r_{apo} + r_{peri})$. The eccentricity distribution is extended and rather uniform with many clusters on relatively radial orbits. The apparent trend that clusters with larger apocentres are on more radial orbits may be due to our sample selection (presently located within ∼ 20 kpc from the Sun). A cluster with a large apocentre will nearly only make it to our sample if it has a relatively radial orbit. It will be possible to draw more robust conclusions about the distribution of orbital parameters once the whole globular cluster population has been analysed. Nonetheless, Fig. 20 already highlights that the bigger differences in the orbital properties for the various potentials considered are for clusters with apocentres in the inner 5 kpc or so. And that these differences are in many cases, larger than the error bars. This implies that there is room for improvement by performing a self-consistent dynamical model of the globular cluster population and the mass distribution in our Galaxy (e.g. Binney & Wong 2017).

6.3. Results for the dwarf galaxies

In Fig. 21 we plot the orbits of the different dwarf (spheroidal) galaxies. This figure reveals for example that the orbits of Draco and Ursa Minor look alike, and that the orbital planes of most dSph are different, with e.g. Sagittarius' orbit being orthogonal to that of Draco and Ursa Minor.

Fig. 22 shows the distribution of orbital parameters for the dSph (and listed in Table D.2). We have plotted here the median values (over 10 Gyr of integration) and the 16th and 84th percentiles' range as the symbols with solid error bars (derived from the 1000 Monte Carlo realizations of the observables and their uncertainties). Using the same symbols but now with dotted lines, we have plotted the orbital parameters derived including the effect of the 0.035 mas yr^{-1} systematic uncertainty on each of the proper motion components. In general, we see that the effects of the systematic errors on the characteristic properties of the orbits are relatively small. We note however, that in both cases these error bars do not always properly reflect the uncertainties on the orbital parameters because of degeneracies. We include examples of the Monte Carlo realizations in the Appendix (Figure D.3) to give a flavour of these degeneracies.

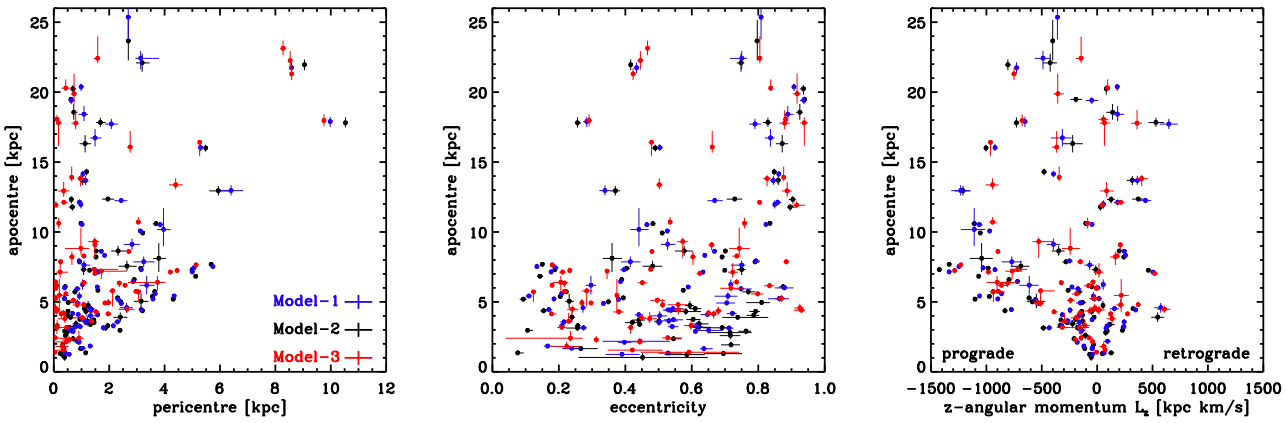


Fig. 20. Distribution of orbital parameters for the globular clusters in our sample. Three globular clusters are not shown in these plots: NGC 3201 and NGC 4590 which have apocentre $\sim$ 30 kpc and large retrograde and prograde motion (respectively, $|L_z| > 2000$ kpc km s^{-1}), and NGC 5466 which has an apocentre $\sim$ 50 kpc (and given its orbital parameters was likely associated to the Sagittarius dwarf, as proposed by Bellazzini et al. 2003). Note the concentration of clusters with small pericentre and apocentre around $L_z \sim 0$ for Model-3. Such clusters are on box orbits in the barred potential of Model-3, and hence do not conserve L_z, whose time average over the 10 Gyr of integration, is approximately zero. The error bars correspond to the 16th and 84th quantiles obtained from the orbit integration using the statistical errors. The effect of the systematic error on the orbits of the globular clusters is found to be negligible, and hence not shown here.

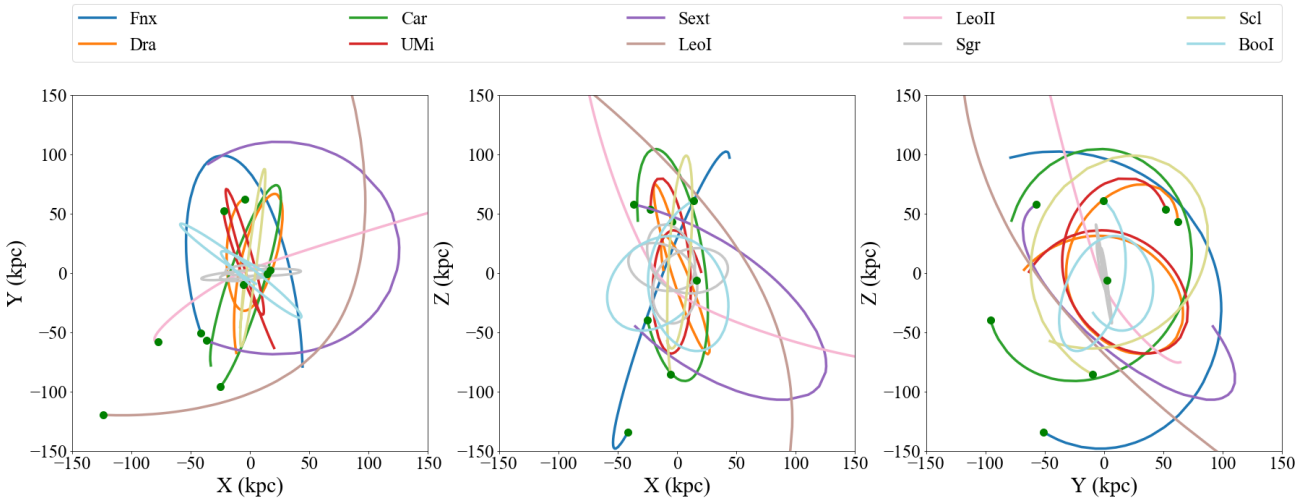


Fig. 21. Orbits integrated backward in time for 2.5 Gyr for the different dwarfs shown in different colours using the potential of Model-2.

Fig. 22 reveals that most satellites are on (slightly) prograde orbits, while Fornax is retrograde (and possibly also Leo II, although it is also consistent with prograde at the 1σ level) as can be seen from the rightmost panel. This is qualitatively similar to what we found for the globular clusters studied. However, the orbital eccentricity distribution for the dSph (middle panel) is very different from that of the clusters. Fewer dwarfs have very elongated orbits as their eccentricity is typically smaller than 0.6. Carina even has a median eccentricity $\lesssim 0.2$ for Models 1 and 2.

This finding leads to two interesting preliminary conclusions. Firstly that there is at most a weak link between the globular clusters in our sample and the dSph (although this is partly driven by our selection of the globular cluster sample). Secondly, the eccentricity distribution of the dwarfs is inconsistent with the predictions of cosmological simulations, where satellites are expected to be on rather radial orbits (e.g. Barber et al. 2014).

Fig. 22 also confirms that Draco and Ursa Minor have very similar orbital properties, and hence possibly constitute a physically connected group. Bootes I appears close to these objects in all panels of this figure, but as we will see below the orientation of its angular momentum differs by $\sim$ 140 deg.

In Fig. 22 we have not plotted Leo I. This is because Leo I has extreme orbital characteristics, and for example, it is unbound in roughly 20% of the realizations for Model-1[10]. In the

[10] This is because of this model's lower dark matter halo mass. For example the escape velocity from the location of the Sun for Model-2 is 812 km s^{-1}, which may be compared to the value of $\sim$ 533 km s^{-1}derived by Piffl et al. (2014) from RAVE data and consistent with that of Model-1.

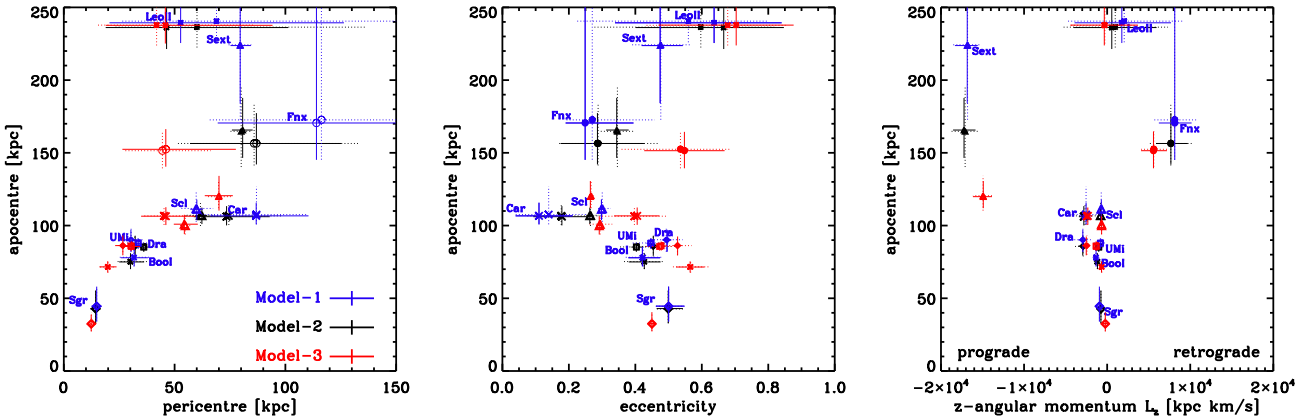


Fig. 22. Distribution of orbital parameters for the dSph. The different colours indicate computations with different potentials. The agreement is generally good, with Model-3 systematically leading to smaller pericentres as a result of its higher mass at the radii probed by the systems. Larger differences are found for the more distant objects, revealing the sensitivity of their orbits to variations in the Galaxy's mass distributions assumed. Note how the dSph eccentricity distribution differs from that shown in Fig. 20 for the globular clusters in our sample. The symbols with solid error bars correspond, respectively, to the median and uncertainties derived using the Monte Carlo realizations, and those with dotted error bars take also into account a systematic error of 0.035 mas yr^{-1}on each of the proper motion components.

cases in which a bound orbit is found, the predicted median apocentres are 819, 429 and 388, for Models 1, 2, and 3 respectively. Evidently the apocentre of Leo I is beyond the likely virial radius of the Milky Way (estimated to be smaller than 300 kpc, see Bland-Hawthorn & Gerhard 2016, and references therein). The orbit of Leo I is quite eccentric, with medians in the range 0.6 to 0.8. The radial period is greater than 5 Gyr and its estimate varies by a factor two for the various potentials, but a robust prediction is that the last pericentric passage (at a distance of $\sim$ 100 kpc) took place approximately 1 Gyr ago.

The orientations of the orbital planes of the dwarfs, now including the LMC and SMC[11], and averaged over the 10 Gyr of integration, are shown in the top panel of Fig. 23. It has been suggested that the Milky Way dwarf galaxy satellites lie on a plane (Kroupa et al. 2005). We find that their orbits tend to be perpendicular to the Galactic disk (the majority cluster at an inclination of $\sim 90\pm20$ deg) but they span a broad range of orientations. This implies that even though the orientation of the average plane of motion may be similar, they may rotate in the opposite sense as for example Scl and UMi/Dra/LMC/SMC (in the YZ plane), or if we compare Scl and Sgr, they move in planes that are nearly perpendicular to each other (and to the Galactic disk). This ordered complexity could indicate (group) infall from a preferential direction (from a cosmic web filament aligned with z-axis), but does seem not favour one single event giving rise to these configurations.

For the globular clusters we have plotted only the distribution of the current, instantaneous orbital plane inclination, defined as $\cos\theta = L_z/|\mathbf{L}|$, since angular momentum $|\mathbf{L}|$ is not conserved for the majority of the clusters in our sample (for the barred potential of Model-3 also L_z changes). Notice from the bottom panel of Fig. 23 that the globular clusters in our sample show a much broader distribution of inclinations than the dwarf galaxies. This behaviour however could again reflect a bias in the selection of the sample of globular clusters we have analysed in this paper, for example in the sense that there are fewer of the outer clusters that could potentially have been associated to dwarf galaxies.

[11] We include the Magellanic Clouds here because the orientation of their angular momenta has likely been less affected by dynamical friction than the other orbital parameters.

7. Discussion

7.1. Brief summary on systematics

The analysis performed in this paper has served to highlight the excellent quality of the *Gaia* DR2, and also to pinpoint its limitations. On this second aspect we have in particular, confirmed a systematic offset in the parallax of sources (see Arenou et al. 2018; Lindegren & et al. 2018), which we find has an amplitude of ~ -0.049 mas when averaged over all dSph, while averaged over the globular clusters it is ~ -0.025 mas. This offset varies in amplitude from location to location on the sky, which explains the difference found between our samples of dSph and globular clusters. Such an offset has not been found in the proper motions, for example when studying open clusters (Arenou et al. 2018), from which we conclude that if such a systematic is present, it is of small amplitude. However, we do find that because of local variations (driven by the non-uniform scanning of the sky), the proper motions might have an additional systematic uncertainty of ~ 0.035 mas yr^{-1} in each direction.

7.2. Exemplifying the quality of the data

7.2.1. Galactic satellites

We have been able to determine robustly the proper motions of all 75 globular clusters in our sample (with significance much greater than 10σ). The effect of a systematic floor noise level (see Arenou et al. 2018; Lindegren & et al. 2018) is negligible for the clusters in our sample. This is also the case for the majority of the dwarf galaxies we have analysed, possibly with the exception of Leo I (because of its large distance), and Leo II (because it is small on the sky). Nonetheless, even this systematic uncertainty is typically smaller than the uncertainties of previously reported measurements of the PM of globular clusters and dSph in the Milky Way halo.

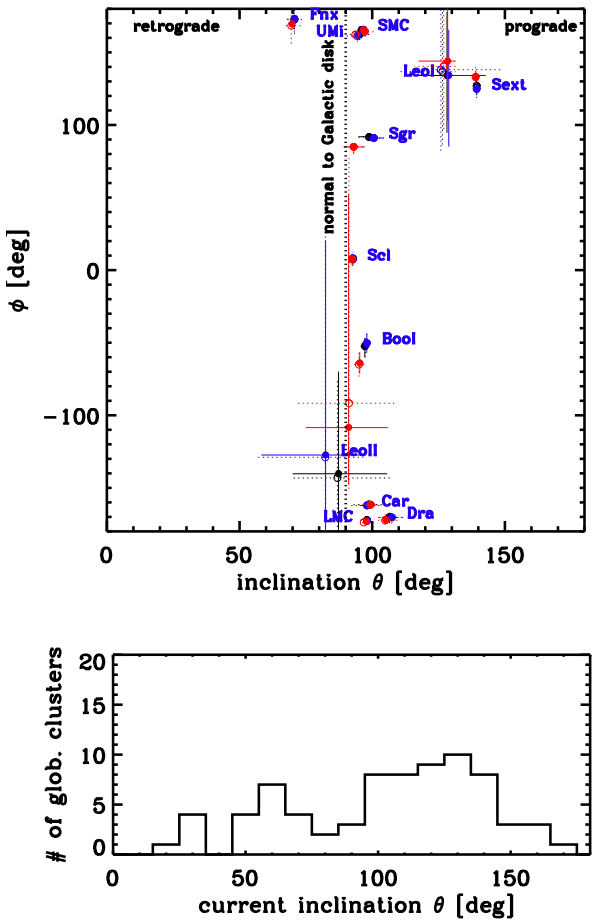


Fig. 23. *Top*: Orientation of the time-averaged orbital plane, defined by the angular momentum angles (ϕ, θ) for the different dwarfs, for the various potentials explored. The colours and the error bars are as in Fig. 22, and open and solid circles are the median values obtained by considering or not our estimate of the systematic error on the proper motions. Most dwarfs have highly inclined orbits with respect to the Galactic plane (i.e. $\theta \sim 90^{o}$). Their variation in orientation (angle ϕ) over the 10 Gyr of integration is much smaller than the size of the error bars. *Bottom*: Histogram showing the present-day inclination of the orbits for the globular clusters.

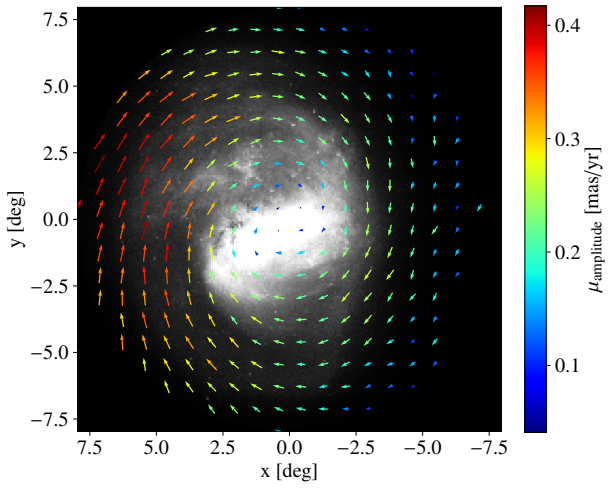


Fig. 24. Proper motions of stars in the LMC, represented as vectors, overlaid on a representation of the source density. This figure shows the clear consistent rotation measured by *Gaia* around the centre of the LMC.

In the case of the dSph, the possibility of selecting members now via PM has revealed (and confirmed previous hints of) important spatial asymmetries, and possibly also tidal features in several systems. We have not analysed the significance of these features nor have we attempted to establish the presence of tidal tails beyond the field of view of 2 deg that we have chosen to measure their mean PM in this study. This is an area that we expect the community to explore with *Gaia* DR2, especially now that the proper motions are so accurate that reliable predictions can be made for the orbits of these systems and hence also give an indication on where one might expect streams if present.

The improved proper motions for millions of stars in the Magellanic Clouds offer a unique dataset for understanding the internal dynamics of these systems. For example, Fig. 24 shows the velocity map obtained for LMC, and reveals a high degree of order in the rotational motion of this system. This has allowed us to derive a rotation curve based on tangential velocities that is competitive to that obtained using radial velocity information. However, we also find indications in the proper motion residuals (after subtraction of a model rotating inclined disc), of streaming motion along the bar. Not only do we learn about internal structure and mass distribution of the Clouds, but this dataset will also help us in understanding how and when the two galaxies interacted, and whether and how this is related to the Magellanic stream (e.g. Kallivayalil et al. 2006a). It is likely it will even be possible to find stars stripped from the Clouds at much larger distances than previously attempted.

This brief discussion on the impressive astrometric quality of the *Gaia* DR2 datasets for the Galactic satellites, calls for need of high-precision radial velocity measurements and abundances follow-up for as many as possible of the members identified by *Gaia* (as planned for example, by the WEAVE and 4MOST projects, see e.g. Feltzing et al. 2017). Lists of possible members according to our analyses are given in Table D.3, for the globular clusters, dSph and UFD galaxies, and for the Magellanic Clouds.

7.2.2. Substructure and debris

The methodology used in this paper thus far has relied on the objects of interest being concentrated on a specific location on the sky. Tidally torn satellites and streams, on the other hand may extend across significant parts of the celestial sphere. Here we briefly demonstrate the capacity of *Gaia* DR2 to also investigate this kind of structures in the Milky Way using astrometric data only. Further and deeper analysis is left to the general users of *Gaia* DR2.

One known substructure in the halo near the Sun that presumably originated in a disrupted satellite was discovered by Helmi et al. (1999), defining a clump in the L_z versus $|L_\perp| = \sqrt{L_x^2 + L_y^2}$ space. The physical reality of this structure – sometimes called Helmi's stream – was later independently confirmed by e.g. Chiba & Beers (2000); Smith et al. (2009), but no significant additional members have been identified since then. *Gaia* DR2 will likely reveal a very large number of new members, but

measuring L_z and $L_\perp$ without radial velocity can only be done exactly in two small areas on the sky: in the directions of the Galactic centre and anticentre. In this case, μ_l and μ_b translate directly into the space velocities v_z and v_ϕ with knowledge of the distance D. The angular-momentum components are then simply $L_z = xv_\phi$ and $L_\perp = L_y \sim -xv_z$, where $x = D + R_\odot$, and $R_\odot$ is the Galactocentric distance of the Sun.

We show the distribution of stars within a circle of 15 degrees radius around the Galactic anticentre in the L_z vs. L_y space in Fig. 25. We consider here only stars with $\varpi/\sigma_\varpi/ > 5$. Besides the dominant disk centred on $(-1800, 0)$ kpc km s^{-1}, and the more diffuse halo centred on (0,0), there is a distinct concentration of stars around $(-1100, -2400)$ kpc km s^{-1}, corresponding to the expected location of the Helmi stream. A tight cut around the centre of this clump gives 32 candidate members (with distances from 260 pc to about 2 kpc), more than tripling the original number reported in Helmi et al. (1999). An HR diagram of these 32 members – using *Gaia* DR2 G magnitudes, parallaxes and $G_{\rm BP}$–$G_{\rm RP}$ colours – is shown in Fig. 26. Despite the patchy extinction in this area of the sky, the HR diagram reveals an old, metal-poor main sequence, offset from a corresponding disk sequence by about 0.2 mag towards the blue. As can be seen from this figure, four probable binaries among the 32 new members are present, and the three subgiants indicate a turnoff at an absolute magnitude $M_G \sim 4.5$. A straight extrapolation of the 32 new members from the 15-degree circle to the whole sky would give close to 2000 members in all of DR2. These can in principle be identified using also radial velocity information.

Fig. 25 shows a clear over-density only for $L_y \propto v_z < 0$, and not for $v_z > 0$ (at fixed L_z). This stronger asymmetry in the direction of the anticentre than originally reported by Helmi et al. (1999) (where the ratio was 3:1), may be used to put constraints on the accretion time and suggests that the merger may have taken place even more recently than argued by e.g. Kepley et al. (2007).

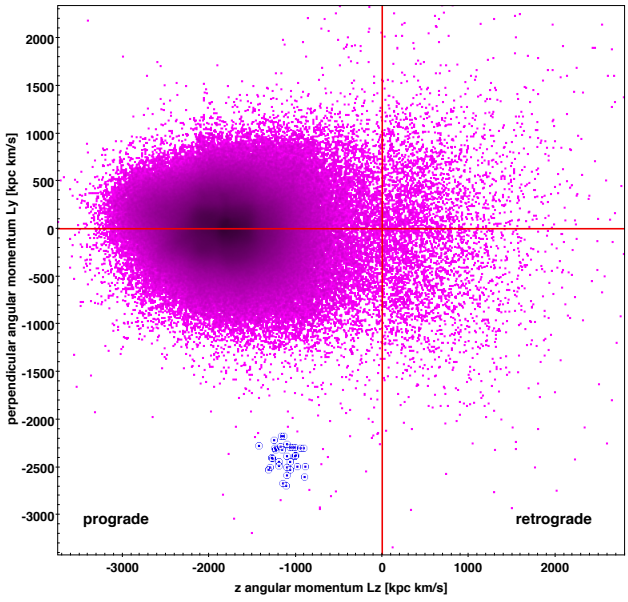


Fig. 25. Distribution of DR2 stars in a circle of 15 degrees radius around the Galactic anticentre direction in the $L_\perp = L_y$ vs L_z space. The Helmi stream is the distinct density enhancement near the bottom of the plot (in blue). We have assumed here $v_{rot} = 220$ km s^{-1}for the LSR velocity, $v_{z,\odot}$=5 km s^{-1}, and $v_{\phi,\odot}$=7 km s^{-1}for the peculiar motion of the Sun, and $R_\odot = 8.1$ kpc.

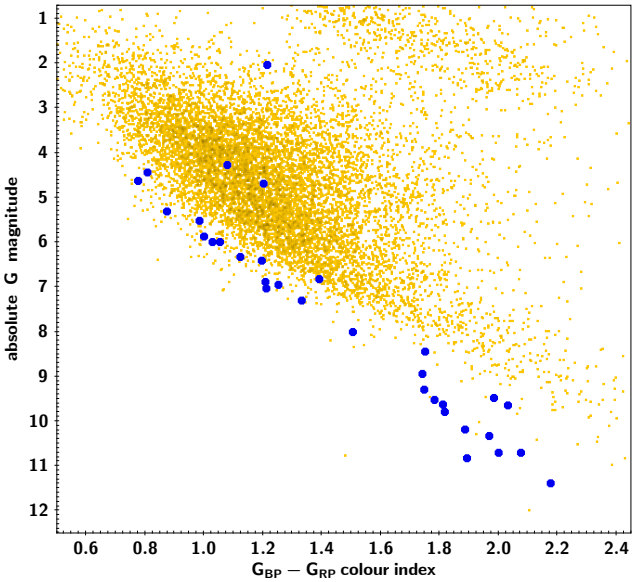


Fig. 26. Hertzprung-Russell Diagram using *Gaia* DR2 G magnitudes, colours and parallaxes in the direction of the Galactic anticentre. The yellowish cloud represents a random sample of disk stars, selected on the basis of their disk-like L_z and $L_\perp$, while the blue dots are the 32 new members of the Helmi stream.

7.3. Implications for the formation and dynamics

The unprecedentedly accurate proper motions derived for the Galactic satellites from the *Gaia* DR2 data will allow determining the mass distribution of the Milky Way well into the realms of the dark matter halo. They will enable breaking the degeneracy between the slope of the mass density profile and the orbital anisotropy (Wilkinson & Evans 1999; Watkins et al. 2010), the latter being the limiting factor thus far and which *Gaia* DR2 has turned into an observable. Interestingly our measurements indicate that the orbits of the dSph are not very radial, and this appears to be in tension with expectations derived from cosmological simulations in the ΛCDM framework (e.g. Lux et al. 2010; Cautun & Frenk 2017). Their relatively low eccentricity ($r_{apo}/r_{peri} < 4$) and non-penetrating orbits ($r_{peri} > 30$ kpc) may also disfavour models for the transition of dwarf irregulars to dSph via a tidal-stirring mechanism (Kazantzidis et al. 2017).

We have found, when integrated over short timescales, relatively small differences in the orbits in three different realistic Galactic potentials we have explored (and which are based on Allen & Santillan 1991; Robin et al. 2003; McMillan 2017). This is the case for those globular clusters that do not probe the inner few kpc of the Milky Way and for the dwarf galaxies. This implies that the orbits forecasting power is high and thus could potentially be used to search for tidal tails particularly for the globular clusters, both through their predicted location on the sky but also using proper motion information that is now available thanks to *Gaia* DR2. This is a particularly interesting avenue because of the very high constraining power of streams on the mass distribution in our Galaxy (see Johnston & Carlberg 2016, and references therein).

Another interesting constraint comes from the most distant satellite Leo I. This object has been most recently used to derive a limit on the mass of the dark matter halo of the Milky Way on the basis of the so-called timing argument by Sohn et al. (2013). From our own measurements of the proper motion of Leo I we find that it is barely bound, with its orbit going well beyond re-

cent estimates of the virial radius of our Galaxy. Although it is very unlikely Leo I is unbound (Boylan-Kolchin et al. 2013), we may use it to derive a lower limit to the mass of the Milky Way if we assume it has the escape velocity. Neglecting the contribution of the disk(s) and bulge, for a (non-truncated) NFW halo

$$M_{MW} = \frac{2v_{LeoI}^2 r_{LeoI}}{G} \frac{\log(1+c) - c/(1+c)}{\log(1 + r_{LeoI}/r_s)}. \quad (6)$$

Using our estimates of $v_{LeoI} \sim 217.3^{+62.6}_{-48.9}$ km s^{-1}and $r_{LeoI} \sim 257.8^{+16.8}_{-35.1}$ kpc, this implies a lower limit for the virial mass of the Milky Way of $M_{MW} = 9.8^{+6.7}_{-2.7} \times 10^{11}$ M$_\odot$ assuming $c = 16$ and $r_s = 18.6$ kpc as in McMillan (2017), and where the error bars indicate the 16th and 84th percentiles. If we let these parameters vary in the ranges $10 \leq c \leq 20$ and $10 \leq r_s \leq 30$ kpc, the estimate of the lower limit to the virial mass varies by $\sim 15\%$, i.e. within the uncertainties bracketed by the measurement errors. This value is in line with previous work (see review by Bland-Hawthorn & Gerhard 2016, and references therein), and does not preclude a light dark matter halo for our Galaxy (of $\sim 10^{12}$M$_\odot$, e.g. Battaglia et al. 2005; Gibbons et al. 2014).

Leo I is an intriguing object because it is very distant and its velocity indicates it is receding from us. A possible explanation for the presence of a system like Leo I is that it has experienced a 3-body interaction with the Magellanic Clouds (Sales et al. 2007). Although we do not explore this possibility here, we do find that the dwarf galaxies' phase-space distribution is not homogeneous. These satellites tend to have orbits with angular momenta perpendicular to the Galactic disk, i.e. their orbits take place in planes with varying orientations but always with high inclination. This supports the idea of filamentary infall (see Libeskind et al. 2005), and could also imply that some of the dSph in our sample have fallen in together as a group (Lynden-Bell & Lynden-Bell 1995; Li & Helmi 2008). For example, the relative distances of Ursa Minor and Draco remain relatively small when computed over our 10 Gyr long orbital integrations, thus favouring some amount of group infall.

Our measurements rule out that the dwarf galaxies are on one single narrow "disk", an idea that has led to an important debate in the literature. Furthermore, although some objects are on the same plane, they rotate in a different sense around the Galaxy, making it less likely they formed in single event such as e.g. a major merger (Yang et al. 2014, such a scenario would also require that their eccentricities be relatively large, contrary to what we find from *Gaia* DR2 data). On the other hand, our measurements will finally make it possible to explore how the satellite population was put in place and how this relates to the environment of the Milky Way on a firm basis (Libeskind et al. 2015).

Future studies of the orbital properties of the more distant globular clusters will allow us to establish their relation to the present-day dwarf galaxies population (and further test the ideas put forward in Lynden-Bell & Lynden-Bell 1995). On the other hand, some of the globular clusters in our sample may have been associated with long-gone accreted galaxies, whose debris we might expect will be discovered and characterised using *Gaia* DR2 data. Together this will shed light on the build up of the globular cluster population and its link to former and current satellite galaxies.

8. Conclusions

The second data release from the *Gaia* mission has delivered its promise of new and accurate proper motion measurements for a billion stars across the full Galaxy and its nearest neighbours. Our analysis of the proper motions of stars in roughly half of the Galactic globular clusters, in all the known dSph galaxies and in the Magellanic Clouds has allowed us to derive their mean motions as they orbit around the Galaxy, much more precisely than ever before despite systematics clearly present in this data release. The simple analyses carried out in this paper have confirmed, and also revealed for many globular clusters, earlier reported internal dynamical complexity (such as rotation and the presence of extended halos). The proper motions, and hence the orbits, of the dSph have finally been pinned-down, and this has uncovered their relatively coherent phase-space distribution which however, is not consistent with a single "disk of satellites". The astounding dynamical maps of the Magellanic clouds contain such richness that is has even been possible for the Large Magellanic Cloud to derive for the first time a high quality rotation curve based on tangential velocities only and to unveil the dynamical imprint of the bar.

There is a great deal to be understood and be discovered from the proper motions that have become available with *Gaia* DR2. This dataset will undoubtedly keep the Galactic astronomy community busy for many years to come.

Acknowledgements

We are very grateful to the referee, dr. Mario Mateo, for his prompt, very positive and constructive report. This work presents results from the European Space Agency (ESA) space mission *Gaia*. *Gaia* data are being processed by the *Gaia* Data Processing and Analysis Consortium (DPAC). Funding for the DPAC is provided by national institutions, in particular the institutions participating in the *Gaia* MultiLateral Agreement (MLA). The *Gaia* mission website is `https://www.cosmos.esa.int/gaia`. The *Gaia* archive website is `https://archives.esac.esa.int/gaia`.

The *Gaia* mission and data processing have financially been supported by, in alphabetical order by country:

- the Algerian Centre de Recherche en Astronomie, Astrophysique et Géophysique of Bouzareah Observatory;
- the Austrian Fonds zur Förderung der wissenschaftlichen Forschung (FWF) Hertha Firnberg Programme through grants T359, P20046, and P23737;
- the BELgian federal Science Policy Office (BELSPO) through various PROgramme de Développement d'Expériences scientifiques (PRODEX) grants and the Polish Academy of Sciences - Fonds Wetenschappelijk Onderzoek through grant VS.091.16N;
- the Brazil-France exchange programmes Fundação de Amparo à Pesquisa do Estado de São Paulo (FAPESP) and Coordenação de Aperfeicoamento de Pessoal de Nível Superior (CAPES)-Comité Français d'Evaluation de la Coopération Universitaire et Scientifique avec le Brésil (COFECUB);
- the Chilean Dirección de Gestión de la Investigación (DGI) at the University of Antofagasta and the Comité Mixto ESO-Chile;
- the National Science Foundation of China (NSFC) through grants 11573054 and 11703065;
- the Czech-Republic Ministry of Education, Youth, and Sports through grant LG 15010, the Czech Space Office through ESA PECS contract 98058, and Charles University Prague through grant PRIMUS/SCI/17;
- the Danish Ministry of Science;
- the Estonian Ministry of Education and Research through grant IUT40-1;

– the European Commission's Sixth Framework Programme through the European Leadership in Space Astrometry (https://www.cosmos.esa.int/web/gaia/elsa-rtn-programme, ELSA) Marie Curie Research Training Network (MRTN-CT-2006-033481), through Marie Curie project PIOF-GA-2009-255267 (Space AsteroSeismology & RR Lyrae stars, SAS-RRL), and through a Marie Curie Transfer-of-Knowledge (ToK) fellowship (MTKD-CT-2004-014188); the European Commission's Seventh Framework Programme through grant FP7-606740 (FP7-SPACE-2013-1) for the *Gaia* European Network for Improved data User Services (http://genius-euproject.eu/, GENIUS) and through grant 264895 for the *Gaia* Research for European Astronomy Training (https://www.cosmos.esa.int/web/gaia/great-programme, GREAT-ITN) network;
– the European Research Council (ERC) through grants 320360 and 647208 and through the European Union's Horizon 2020 research and innovation programme through grants 670519 (Mixing and Angular Momentum tranSport of massIvE stars – MAMSIE) and 687378 (Small Bodies: Near and Far);
– the European Science Foundation (ESF), in the framework of the *Gaia* Research for European Astronomy Training Research Network Programme (https://www.cosmos.esa.int/web/gaia/great-programme, GREAT-ESF);
– the European Space Agency (ESA) in the framework of the *Gaia* project, through the Plan for European Cooperating States (PECS) programme through grants for Slovenia, through contracts C98090 and 4000106398/12/NL/KML for Hungary, and through contract 4000115263/15/NL/IB for Germany;
– the European Union (EU) through a European Regional Development Fund (ERDF) for Galicia, Spain;
– the Academy of Finland and the Magnus Ehrnrooth Foundation;
– the French Centre National de la Recherche Scientifique (CNRS) through action 'Défi MASTODONS', the Centre National d'Etudes Spatiales (CNES), the L'Agence Nationale de la Recherche (ANR) 'Investissements d'avenir' Initiatives D'EXcellence (IDEX) programme Paris Sciences et Lettres (PSL$*$) through grant ANR-10-IDEX-0001-02, the ANR 'Défi de tous les savoirs' (DS10) programme through grant ANR-15-CE31-0007 for project 'Modelling the Milky Way in the Gaia era' (MOD4Gaia), the Région Aquitaine, the Université de Bordeaux, and the Utinam Institute of the Université de Franche-Comté, supported by the Région de Franche-Comté and the Institut des Sciences de l'Univers (INSU);
– the German Aerospace Agency (Deutsches Zentrum für Luft- und Raumfahrt e.V., DLR) through grants 50QG0501, 50QG0601, 50QG0602, 50QG0701, 50QG0901, 50QG1001, 50QG1101, 50QG1401, 50QG1402, 50QG1403, and 50QG1404 and the Centre for Information Services and High Performance Computing (ZIH) at the Technische Universität (TU) Dresden for generous allocations of computer time;
– the Hungarian Academy of Sciences through the Lendület Programme LP2014-17 and the János Bolyai Research Scholarship (L. Molnár and E. Plachy) and the Hungarian National Research, Development, and Innovation Office through grants NKFIH K-115709, PD-116175, and PD-121203;
– the Science Foundation Ireland (SFI) through a Royal Society - SFI University Research Fellowship (M. Fraser);
– the Israel Science Foundation (ISF) through grant 848/16;
– the Agenzia Spaziale Italiana (ASI) through contracts I/037/08/0, I/058/10/0, 2014-025-R.0, and 2014-025-R.1.2015 to the Italian Istituto Nazionale di Astrofisica (INAF), contract 2014-049-R.0/1/2 to INAF dedicated to the Space Science Data Centre (SSDC, formerly known as the ASI Sciece Data Centre, ASDC), and contracts I/008/10/0, 2013/030/I.0, 2013-030-I.0.1-2015, and 2016-17-I.0 to the Aerospace Logistics Technology Engineering Company (ALTEC S.p.A.), and INAF;
– the Netherlands Organisation for Scientific Research (NWO) through grant NWO-M-614.061.414 and through a VICI grant (A. Helmi) and the Netherlands Research School for Astronomy (NOVA);
– the Polish National Science Centre through HARMONIA grant 2015/18/M/ST9/00544 and ETIUDA grants 2016/20/S/ST9/00162 and 2016/20/T/ST9/00170;
– the Portugese Fundação para a Ciência e a Tecnologia (FCT) through grant SFRH/BPD/74697/2010; the Strategic Programmes UID/FIS/00099/2013 for CENTRA and UID/EEA/00066/2013 for UNINOVA;
– the Slovenian Research Agency through grant P1-0188;
– the Spanish Ministry of Economy (MINECO/FEDER, UE) through grants ESP2014-55996-C2-1-R, ESP2014-55996-C2-2-R, ESP2016-80079-C2-1-R, and ESP2016-80079-C2-2-R, the Spanish Ministerio de Economía, Industria y Competitividad through grant AyA2014-55216, the Spanish Ministerio de Educación, Cultura y Deporte (MECD) through grant FPU16/03827, the Institute of Cosmos Sciences University of Barcelona (ICCUB, Unidad de Excelencia 'María de Maeztu') through grant MDM-2014-0369, the Xunta de Galicia and the Centros Singulares de Investigación de Galicia for the period 2016-2019 through the Centro de Investigación en Tecnologías de la Información y las Comunicaciones (CITIC), the Red Española de Supercomputación (RES) computer resources at MareNostrum, and the Barcelona Supercomputing Centre - Centro Nacional de Supercomputación (BSC-CNS) through activities AECT-2016-1-0006, AECT-2016-2-0013, AECT-2016-3-0011, and AECT-2017-1-0020;
– the Swedish National Space Board (SNSB/Rymdstyrelsen);
– the Swiss State Secretariat for Education, Research, and Innovation through the ESA PRODEX programme, the Mesures d'Accompagnement, the Swiss Activités Nationales Complémentaires, and the Swiss National Science Foundation;
– the United Kingdom Rutherford Appleton Laboratory, the United Kingdom Science and Technology Facilities Council (STFC) through grant ST/L006553/1, the United Kingdom Space Agency (UKSA) through grant ST/N000641/1 and ST/N001117/1, as well as a Particle Physics and Astronomy Research Council Grant PP/C503703/1.

References

Allen, C. & Santillan, A. 1991, Rev. Mexicana Astron. Astrofis., 22, 255
Arenou, F., et al., & . 2018, A&A, (DPACP-39)
Armandroff, T. E., Olszewski, E. W., & Pryor, C. 1995, AJ, 110, 2131
Barber, C., Starkenburg, E., Navarro, J. F., McConnachie, A. W., & Fattahi, A. 2014, MNRAS, 437, 959
Battaglia, G., Helmi, A., Morrison, H., et al. 2005, MNRAS, 364, 433
Battaglia, G., Helmi, A., Tolstoy, E., et al. 2008, ApJ, 681, L13
Battaglia, G., Tolstoy, E., Helmi, A., et al. 2011, MNRAS, 411, 1013
Battaglia, G., Tolstoy, E., Helmi, A., et al. 2006, A&A, 459, 423

Baumgardt, H. 2017, MNRAS, 464, 2174
Baumgardt, H. & Makino, J. 2003, MNRAS, 340, 227
Bechtol, K., Drlica-Wagner, A., Balbinot, E., et al. 2015, ApJ, 807, 50
Bekki, K. 2012, MNRAS, 422, 1957
Bellazzini, M., Bragaglia, A., Carretta, E., et al. 2012, A&A, 538, A18
Bellazzini, M., Ferraro, F. R., & Ibata, R. 2003, AJ, 125, 188
Bellini, A., Vesperini, E., Piotto, G., et al. 2015, ApJ, 810, L13
Belokurov, V., Zucker, D. B., Evans, N. W., et al. 2006, ApJ, 647, L111
Besla, G., Kallivayalil, N., Hernquist, L., et al. 2007, ApJ, 668, 949
Besla, G., Martínez-Delgado, D., van der Marel, R. P., et al. 2016, ApJ, 825, 20
Bianchini, P., Varri, A. L., Bertin, G., & Zocchi, A. 2013, ApJ, 772, 67
Bienayme, O., Robin, A. C., & Creze, M. 1987, A&A, 180, 94
Binney, J. & Wong, L. K. 2017, MNRAS, 467, 2446
Bland-Hawthorn, J. & Gerhard, O. 2016, ARA&A, 54, 529
Boylan-Kolchin, M., Bullock, J. S., Sohn, S. T., Besla, G., & van der Marel, R. P. 2013, ApJ, 768, 140
Carballo-Bello, J. A., Gieles, M., Sollima, A., et al. 2012, MNRAS, 419, 14
Casetti-Dinescu, D. I., Girard, T. M., Herrera, D., et al. 2007, AJ, 134, 195
Casetti-Dinescu, D. I., Girard, T. M., Jílková, L., et al. 2013, AJ, 146, 33
Casetti-Dinescu, D. I., Girard, T. M., Korchagin, V. I., van Altena, W. F., & López, C. E. 2010, AJ, 140, 1282
Casetti-Dinescu, D. I., Girard, T. M., & Schriefer, M. 2018, MNRAS, 473, 4064
Cautun, M. & Frenk, C. S. 2017, MNRAS, 468, L41
Chiba, M. & Beers, T. C. 2000, AJ, 119, 2843
Cioni, M.-R. L., Habing, H. J., & Israel, F. P. 2000a, A&A, 358, L9
Cioni, M.-R. L., van der Marel, R. P., Loup, C., & Habing, H. J. 2000b, A&A, 359, 601
Contopoulos, G. & Papayannopoulos, T. 1980, A&A, 92, 33
Cropper, M., et al., & . 2018, A&A, (DPACP-46)
Dinescu, D. I., Girard, T. M., van Altena, W. F., & López, C. E. 2003, AJ, 125, 1373
Dinescu, D. I., van Altena, W. F., Girard, T. M., & López, C. E. 1999, AJ, 117, 277
Djorgovski, S. & Meylan, G. 1994, AJ, 108, 1292
Feltzing, S., Bensby, T., Bergemann, M., et al. 2017, ArXiv e-prints
Freedman, W. L., Madore, B. F., Gibson, B. K., et al. 2001, ApJ, 553, 47
Gaia Collaboration, Babusiaux, C., & et al. 2018a, A&A, (DPACP-31)
Gaia Collaboration, Brown, A., & et al. 2018b, A&A, (DPACP-36)
Gaia Collaboration, Brown, A. G. A., Vallenari, A., et al. 2016, A&A, 595, A2
Gaia Collaboration, van Leeuwen, F., Vallenari, A., et al. 2017, A&A, 601, A19
Gibbons, S. L. J., Belokurov, V., & Evans, N. W. 2014, MNRAS, 445, 3788
Gómez, F. A., Besla, G., Carpintero, D. D., et al. 2015, ApJ, 802, 128
Gómez, F. A., Minchev, I., O'Shea, B. W., et al. 2013, MNRAS, 429, 159
Gratton, R. G., Carretta, E., & Bragaglia, A. 2012, A&A Rev., 20, 50
Harris, J. & Zaritsky, D. 2006, AJ, 131, 2514
Harris, W. E. 1996, AJ, 112, 1487
Harris, W. E. 2010, http://physwww.mcmaster.ca/~harris/mwgc.dat, (Harris10)
Helmi, A., White, S. D. M., de Zeeuw, P. T., & Zhao, H. 1999, Nature, 402, 53
Hénault-Brunet, V., Gieles, M., Agertz, O., & Read, J. I. 2015, MNRAS, 450, 1164
Ibata, R., Nipoti, C., Sollima, A., et al. 2013, MNRAS, 428, 3648
Irrgang, A., Wilcox, B., Tucker, E., & Schiefelbein, L. 2013, A&A, 549, A137
Irwin, M. & Hatzidimitriou, D. 1995, MNRAS, 277, 1354
Johnston, K. V. & Carlberg, R. G. 2016, in Astrophysics and Space Science Library, Vol. 420, Tidal Streams in the Local Group and Beyond, ed. H. J. Newberg & J. L. Carlin, 169
Kallivayalil, N., van der Marel, R. P., & Alcock, C. 2006a, ApJ, 652, 1213
Kallivayalil, N., van der Marel, R. P., Alcock, C., et al. 2006b, ApJ, 638, 772
Kallivayalil, N., van der Marel, R. P., Besla, G., Anderson, J., & Alcock, C. 2013, ApJ, 764, 161
Kamann, S., Husser, T.-O., Dreizler, S., et al. 2017, ArXiv e-prints
Kazantzidis, S., Łokas, E. L., Callegari, S., Mayer, L., & Moustakas, L. A. 2011, ApJ, 726, 98
Kazantzidis, S., Mayer, L., Callegari, S., Dotti, M., & Moustakas, L. A. 2017, ApJ, 836, L13
Kepley, A. A., Morrison, H. L., Helmi, A., et al. 2007, AJ, 134, 1579
Kim, S., Staveley-Smith, L., Dopita, M. A., et al. 1998, ApJ, 503, 674
Kleyna, J., Wilkinson, M. I., Evans, N. W., Gilmore, G., & Frayn, C. 2002, MNRAS, 330, 792
Koposov, S. E., Belokurov, V., Torrealba, G., & Evans, N. W. 2015, ApJ, 805, 130
Kroupa, P., Theis, C., & Boily, C. M. 2005, A&A, 431, 517
Küpper, A. H. W., Balbinot, E., Bonaca, A., et al. 2015, ApJ, 803, 80
Küpper, A. H. W., Kroupa, P., Baumgardt, H., & Heggie, D. C. 2010, MNRAS, 407, 2241
Kuzma, P. B., Da Costa, G. S., & Mackey, A. D. 2018, MNRAS, 473, 2881
Lardo, C., Pancino, E., Bellazzini, M., et al. 2015, A&A, 573, A115
Lépine, S., Koch, A., Rich, R. M., & Kuijken, K. 2011, ApJ, 741, 100
Li, Y.-S. & Helmi, A. 2008, MNRAS, 385, 1365
Libeskind, N. I., Frenk, C. S., Cole, S., et al. 2005, MNRAS, 363, 146
Libeskind, N. I., Hoffman, Y., Tully, R. B., et al. 2015, MNRAS, 452, 1052
Lindegren, L. & et al. 2018, A&A, (DPACP-51)
Lindegren, L., Lammers, U., Bastian, U., et al. 2016, A&A, 595, A4
Luks, T. & Rohlfs, K. 1992, A&A, 263, 41
Lux, H., Read, J. I., & Lake, G. 2010, MNRAS, 406, 2312
Lynden-Bell, D. & Lynden-Bell, R. M. 1995, MNRAS, 275, 429
Mackey, A. D. & Gilmore, G. F. 2004, MNRAS, 355, 504
Massari, D., Bellini, A., Ferraro, F. R., et al. 2013, ApJ, 779, 81
Massari, D., Breddels, M. A., Helmi, A., et al. 2018, Nature Astronomy, 2, 156
Mateo, M., Olszewski, E. W., & Walker, M. G. 2008, ApJ, 675, 201
McConnachie, A. W. 2012, AJ, 144, 4
McMillan, P. J. 2017, MNRAS, 465, 76
Meylan, G. & Heggie, D. C. 1997, A&A Rev., 8, 1
Muñoz, R. R., Majewski, S. R., Zaggia, S., et al. 2006, ApJ, 649, 201
Navarro, J. F., Frenk, C. S., & White, S. D. M. 1996, ApJ, 462, 563
Navin, C. A., Martell, S. L., & Zucker, D. B. 2016, ApJ, 829, 123
Nichols, M. & Bland-Hawthorn, J. 2011, ApJ, 732, 17
Odenkirchen, M., Brosche, P., Geffert, M., & Tucholke, H.-J. 1997, New A, 2, 477
Olszewski, E. W., Saha, A., Knezek, P., et al. 2009, AJ, 138, 1570
Pancino, E., Bellazzini, M., Giuffrida, G., & Marinoni, S. 2017, MNRAS, 467, 412
Pawlowski, M. S. & Kroupa, P. 2013, MNRAS, 435, 2116
Perryman, M. A. C., Lindegren, L., Kovalevsky, J., et al. 1997, A&A, 323, L49
Piatek, S., Pryor, C., Bristow, P., et al. 2005, AJ, 130, 95
Piatek, S., Pryor, C., Bristow, P., et al. 2006, AJ, 131, 1445
Piatek, S., Pryor, C., Bristow, P., et al. 2007, AJ, 133, 818
Piatek, S., Pryor, C., & Olszewski, E. W. 2016, AJ, 152, 166
Piatek, S., Pryor, C., Olszewski, E. W., et al. 2003, AJ, 126, 2346
Piatek, S., Pryor, C., Olszewski, E. W., et al. 2004, AJ, 128, 951
Piffl, T., Scannapieco, C., Binney, J., et al. 2014, A&A, 562, A91
Pryor, C., Piatek, S., & Olszewski, E. W. 2015, AJ, 149, 42
Renaud, F., Agertz, O., & Gieles, M. 2017, MNRAS, 465, 3622
Robin, A. C., Marshall, D. J., Schultheis, M., & Reylé, C. 2012, A&A, 538, A106
Robin, A. C., Reylé, C., Derrière, S., & Picaud, S. 2003, A&A, 409, 523
Roderick, T. A., Mackey, A. D., Jerjen, H., & Da Costa, G. S. 2016, MNRAS, 461, 3702
Sales, L. V., Navarro, J. F., Abadi, M. G., & Steinmetz, M. 2007, MNRAS, 379, 1475
Searle, L. & Zinn, R. 1978, ApJ, 225, 357
Smith, M. C., Evans, N. W., Belokurov, V., et al. 2009, MNRAS, 399, 1223
Sohn, S. T., Anderson, J., & van der Marel, R. P. 2012, ApJ, 753, 7
Sohn, S. T., Besla, G., van der Marel, R. P., et al. 2013, ApJ, 768, 139
Sohn, S. T., Majewski, S. R., Muñoz, R. R., et al. 2007, ApJ, 663, 960
Sohn, S. T., Patel, E., Besla, G., et al. 2017, ApJ, 849, 93
Soto, M., Bellini, A., Anderson, J., et al. 2017, AJ, 153, 19
Stanimirović, S., Staveley-Smith, L., & Jones, P. A. 2004, ApJ, 604, 176
Subramanian, S. & Subramaniam, A. 2015, A&A, 573, A135
Taylor, M. B. 2005, in Astronomical Society of the Pacific Conference Series, Vol. 347, Astronomical Data Analysis Software and Systems XIV, ed. P. Shopbell, M. Britton, & R. Ebert, 29
Tolstoy, E., Hill, V., & Tosi, M. 2009, ARA&A, 47, 371
van der Marel, R. P. 2001, AJ, 122, 1827
van der Marel, R. P., Alves, D. R., Hardy, E., & Suntzeff, N. B. 2002, AJ, 124, 2639
van der Marel, R. P. & Kallivayalil, N. 2014, ApJ, 781, 121
van der Marel, R. P. & Sahlmann, J. 2016, ApJ, 832, L23
van Leeuwen, F. 1999, A&A, 341, L71
van Leeuwen, F. 2009, A&A, 497, 209
van Leeuwen, F., Le Poole, R. S., Reijns, R. A., Freeman, K. C., & de Zeeuw, P. T. 2000, A&A, 360, 472
Vesperini, E., McMillan, S. L. W., D'Antona, F., & D'Ercole, A. 2013, MNRAS, 429, 1913
Walker, M. G., Mateo, M., & Olszewski, E. W. 2009, AJ, 137, 3100
Walker, M. G., Olszewski, E. W., & Mateo, M. 2015, MNRAS, 448, 2717
Watkins, L. L., Evans, N. W., & An, J. H. 2010, MNRAS, 406, 264
Wilkinson, M. I. & Evans, N. W. 1999, MNRAS, 310, 645
Yang, Y., Hammer, F., Fouquet, S., et al. 2014, MNRAS, 442, 2419

Appendix A: Additional descriptions

Appendix A.1: Example of data extraction

To illustrate the different stages of the data extraction, we show here an example following the procedure used for the globular cluster NGC 2298.

A first selection was made in a field with a radius of about 1 degree around the cluster centre as given in Harris10. The proper motions for ∼ 259000 stars in that field are shown in the left panel of Fig. A.1. A zoom-in on the diagram (middle panel) shows a small concentration in the proper motion field near position $(3.2, -2.2)$ mas yr^{-1}, which is likely to be the cluster. No other such concentrations are apparent in the same field. A further zoom-in on the concentration (right panel of Fig. A.1) shows it to be real. The data in this field are selected as a new subset, for which the distribution of positions on the sky are shown in the left panel of Fig. A.2, which reveals the cluster more clearly now. The proper motion distribution for this new coverage is also improved, showing much reduced field star contamination (middle panel). Also the distribution over parallaxes now clearly shows the cluster with little contamination (right panel). Finally, for the pre-selection procedure, the colour-magnitude diagram is created for the selection (Fig. A.3), which now contains about 1500 stars. The selected data thus obtained is saved as a CSV file for further analysis through the cluster analysis software.

The analysis software iterates over an astrometric solution for the cluster, in which the parallax and proper motion of the cluster are solved for. The cluster centre is determined based on the mean position of all selected members, without any weighting being applied. First the cluster stars positions are projected on a tangential plane with the assumed cluster centre as zero point. The mean of the cartesian positions is determined, which then is de-projected to provide the new cluster centre on the sky. The relevant equations have been presented in Gaia Collaboration et al. (2017) .

The astrometric solution is based on the parallax and proper motion determinations for the individual member stars. For each star the contribution to the solution is normalized by the covariance matrix (for more details, see Appendix A.1 in Gaia Collaboration et al. 2017). This creates for each star three uncorrelated contributions with unit-weight error variance, contributing to the cluster astrometric parameter solution. Outlier rejection is done on the basis of the normalized residuals, except in a few cases where there is significant disturbance from field stars in the astrometric parameters. In those cases, which are mainly found at lower galactic latitudes, a 3σ cut has been applied to the individual parallaxes and proper motions as based on their standard uncertainties and the estimate of the cluster proper motion and parallax (see also Fig. A.4). The astrometric solution removes a large fraction, but not all, of the remaining field stars as can be seen from the HR diagram shown on the right panel of Fig. A.3. In case this residual population of field stars still causes a significant disturbance to the HR diagram, we perform a final cleanup in TopCat on the basis of that diagram.

Two criteria are set in the iterations over the astrometric solution, one of which could require an extended extract from the archive. The first criterion concerns the internal proper motion dispersion. This could be detected from the dispersion in the proper motions of the brightest cluster members. This is, however, not an unambiguous process, as the observed internal velocity dispersion is often observed to be strongly dependent on distance from the cluster centre. The dispersions were examined in the radial and transverse directions, and three examples are shown in Fig. A.5. The modelling of these dependencies is, however, beyond the scope of the present paper, and an average dispersion was used in all cases for the whole cluster. The values found were generally between 2 and 8 km s^{-1}.

Strong variations in coverage of stars with 5-parameter solutions in the astrometry (Lindegren & et al. 2018) also show in the relation between standard uncertainties on the astrometric parameters and the brightness of the stars. With relatively homogeneous coverage there is a narrow distribution, while, as is the case for ω Cen, a multi-layered set of relations is observed for poorly covered objects (see Fig. A.6). An additional feature appears to be the increased noise on the astrometric data for variable stars with large amplitudes, such as the RR Lyrae stars in globular clusters, as shown in Figure A.7. The exact reason for this is still unclear.

Appendix A.2: Exemplifying some systematics in Gaia DR2 using dwarf galaxies

Figure A.8 shows the parallax zero-point offset for the stars in Carina and demonstrates that it is very robustly measured, and independent of the magnitude of the stars used. This indicates a systematic effect present in the parallax measurements of the DR2 data, which for Carina is of the order of $\varpi_{DR2} - \varpi_{lit} = -0.015 - 0.0095 \sim -0.024$ mas.

Figure A.9 shows the gridding pattern present in the parallaxes, in this case for stars in the LMC and the SMC (see also Lindegren & et al. 2018). This pattern has an amplitude of ∼ 0.03 mas (see bottom panel of Fig. A.10), and is clearly apparent when analysing sufficiently large objects on the sky, but it is likely to be present over the full sky (see e.g. Arenou et al. 2018).

Figure A.10 shows the variation in proper motion and parallax along stripes of width 0.2° in the LMC, after a model for the proper motion field has been subtracted. The variation seen is produced by both the systematic errors in *Gaia* DR2 and the shortcomings of the simple model.

The correlation between the proper motions of individual stars in the field of view towards the dSph in our sample is is illustrated in Fig. A.11 where we have plotted the individual stars with different colours indicating the amount of correlation (from large negative, to none, to large positive) between μ^*_α and μ_δ. Fornax in particular shows a strong correlation in the PM components of the individual stars, and these are of course, then reflected in the PM correlation coefficient given in the table. The amplitude and orientation of the correlation differs from dwarf galaxy to dwarf galaxy, indicating that the correlations are localised on the sky, and do not have the same amplitude everywhere. Furthermore, there are regions where these correlations are negligible, when averaged out, as in the case of Carina, Draco, Sculptor and even the Sagittarius dSph. Note as well that all the stars in the field of view towards these dwarfs are affected in a similar way, and not only the members.

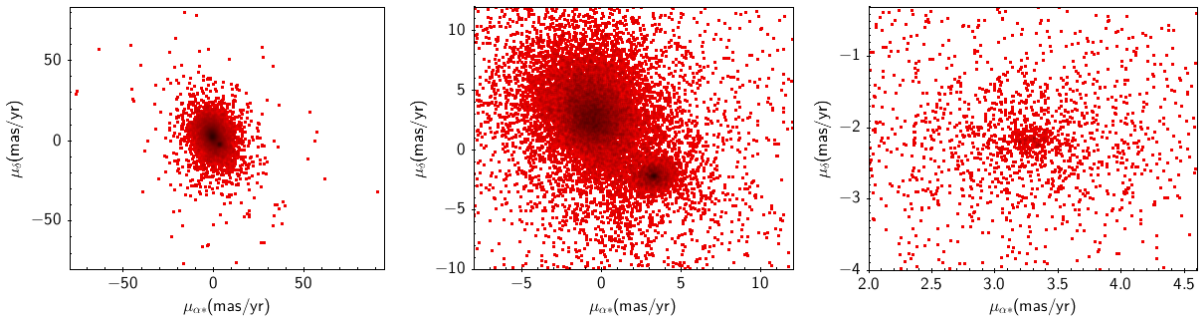


Fig. A.1. The proper motion of stars within 0.5 deg. of the centre of NGC2298 as extracted from the GACS archive. *Left:* All ∼ 259000 stars; *Middle:* A zoom-in on the proper motion field which shows a concentration of the stars near position (3.2, −2.2) mas yr^{-1} corresponding to cluster members. *Right:* A further zoom-in on the proper motion field for the cluster.

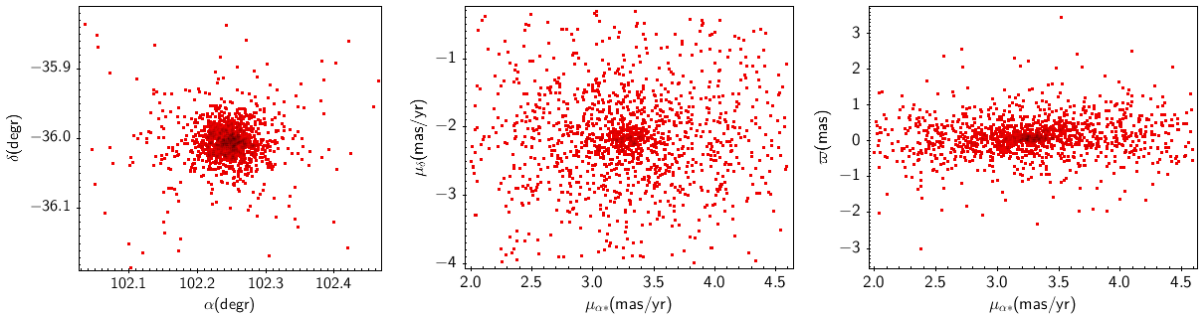


Fig. A.2. From left to right: Distribution of positions on the sky for the first selection on cluster star proper motions, showing the cluster in the centre; distribution of the proper motions for the cluster field; distribution of parallax vs proper motion in RA.

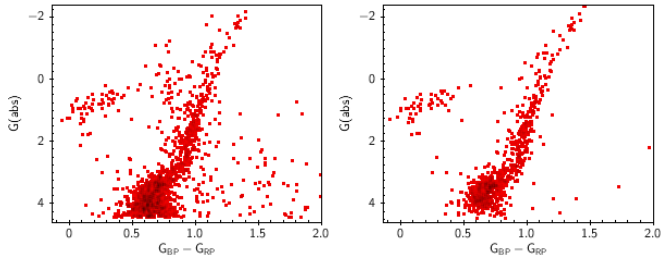


Fig. A.3. The HR diagram for the cluster field before (left) and after (right) the astrometric solution.

Appendix B: Details of the LMC and SMC modelling

In this appendix we provide a rigorous description of the coordinate system used in Sections 2.2 and 5, and the modelling assumptions used to derive Eqs. 3, and the deprojection of the proper motions shown in Figure 18. We will refer to the centre of the Cloud as C, the observer as O and a source in the Cloud as S.

The vectors $[\boldsymbol{x}\ \boldsymbol{y}\ \boldsymbol{z}]$ form an inertially fixed right-handed orthogonal triad with $\boldsymbol{z}$ the unit vector from observer to C, at the reference epoch; $\boldsymbol{x}$ the unit vector in the direction of increasing α at C and $\boldsymbol{y}$ the unit vector in the direction of increasing δ at C.

Appendix B.1: Position and proper motion in the xyz system

In terms of the celestial position (α, δ) and proper motion components $(\mu_{\alpha*}, \mu_\delta)$, we have the unit vector from the observer to a source, $\boldsymbol{u}$, given by:

$$\boldsymbol{u} = \boldsymbol{r}\,, \quad \dot{\boldsymbol{u}} = \boldsymbol{p}\mu_{\alpha*} + \boldsymbol{q}\mu_\delta\,, \tag{B.1}$$

where $[\boldsymbol{p}\ \boldsymbol{q}\ \boldsymbol{r}]$ is the local normal triad at (α, δ):

$$\boldsymbol{p} = \begin{bmatrix} -\sin\alpha \\ \cos\alpha \\ 0 \end{bmatrix}, \quad \boldsymbol{q} = \begin{bmatrix} -\sin\delta\cos\alpha \\ -\sin\delta\sin\alpha \\ \cos\delta \end{bmatrix}, \quad \boldsymbol{r} = \begin{bmatrix} \cos\delta\cos\alpha \\ \cos\delta\sin\alpha \\ \sin\delta \end{bmatrix}. \tag{B.2}$$

The xyz system coincides with the local normal triad at (α_C, δ_C):

$$\boldsymbol{x} = \begin{bmatrix} -\sin\alpha_C \\ \cos\alpha_C \\ 0 \end{bmatrix}, \quad \boldsymbol{y} = \begin{bmatrix} -\sin\delta_C\cos\alpha_C \\ -\sin\delta_C\sin\alpha_C \\ \cos\delta_C \end{bmatrix}, \quad \boldsymbol{z} = \begin{bmatrix} \cos\delta_C\cos\alpha_C \\ \cos\delta_C\sin\alpha_C \\ \sin\delta_C \end{bmatrix}. \tag{B.3}$$

The components of $\boldsymbol{u}, \dot{\boldsymbol{u}}$ in the xyz system are obtained as scalar products (e.g. $x = \boldsymbol{x}\cdot\boldsymbol{u}$, $\dot{x} = \boldsymbol{x}\cdot\dot{\boldsymbol{u}}$) from which we can derive Eqs. 2, where we refer to $\dot{x}, \dot{y}$ as μ_x, μ_y (they are not strictly speaking proper motions, but it is convenient to give them this notation).

Using (α_C, δ_C) as a fixed reference point, the Cartesian coordinates $(x, y, z, \dot{x}, \dot{y}, \dot{z})$ provide a useful substitute for $(\alpha, \delta, \mu_{\alpha*}, \mu_\delta)$. The six components are a redundant set, and when working in a limited area around C (in principle as long as $z > 0$, i.e. within 90° from C) it is possible to use the non-redundant set $(x, y, \dot{x}, \dot{y})$, with

$$z = \sqrt{1 - x^2 - y^2}\,, \quad \dot{z} = -(x\dot{x} + y\dot{y})/z\,. \tag{B.4}$$

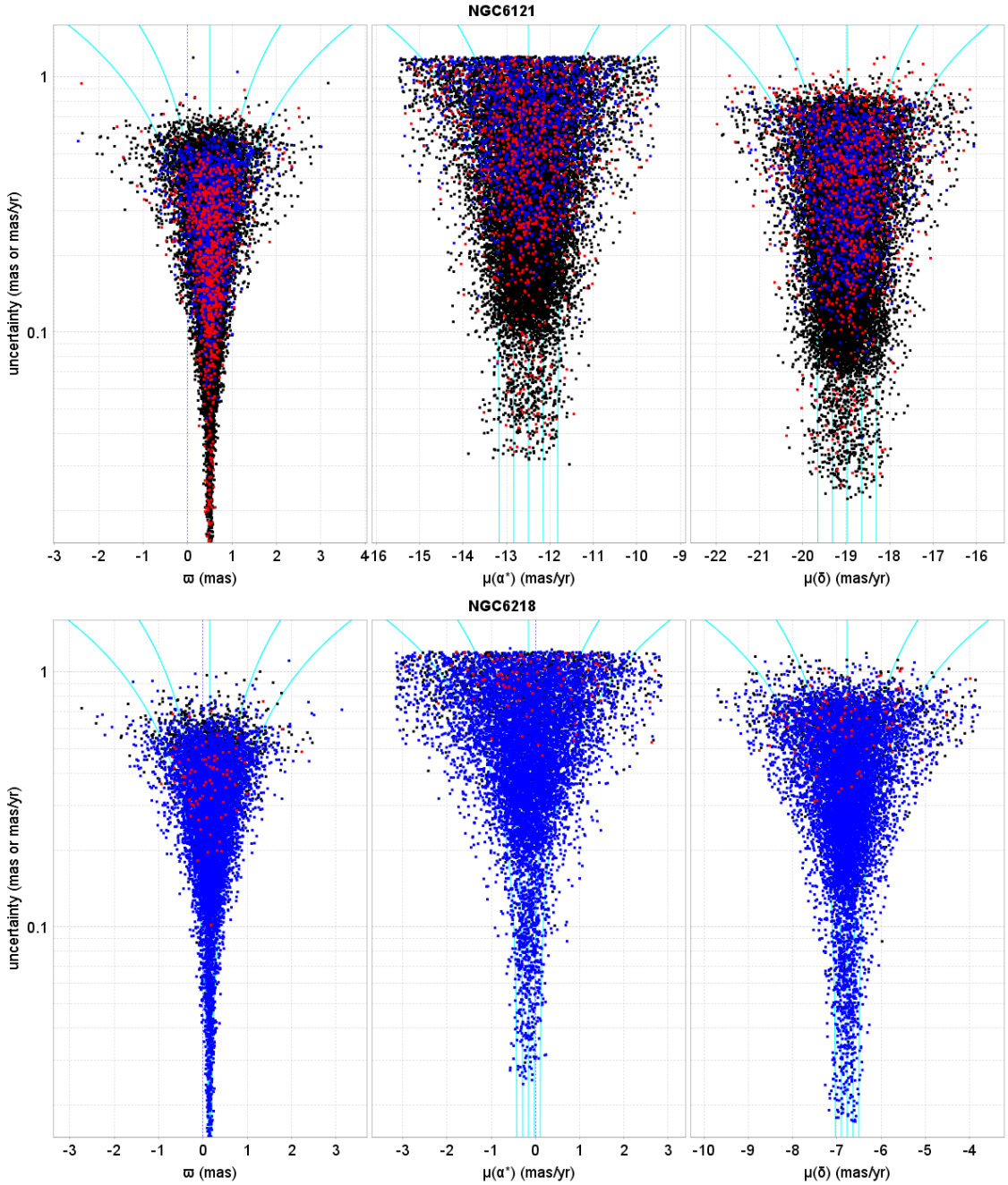


Fig. A.4. Two examples of the parallax and proper motion dispersion diagrams, for clusters at approximately 2 (top) and 5 (bottom) kpc distance. The parallax and proper motions are plotted against the standard uncertainties. The blue lines show the expected uncertainty levels, relative to the mean value, at -2, -1 0 1 and 2 σ, including noise contributions from the internal velocity dispersion and the dispersion of the parallaxes form the depth of the cluster. At low levels of standard uncertainty the contributions from the internal dispersion are easily detected. The colouring of the data points reflects the error correlations, red:strongly negative, blue: strongly positive, black: low.

.

(x, y) is equivalent to the orthographic projection in cartography.[12]

[12] The gnomonic projection $(x/z, y/z)$ is more common in astrometry, where they are known as standard coordinates. For the present problem they do not seem to provide any particular advantage, and the expressions for the time derivatives become much more complicated.

Appendix B.2: Kinematic model

Assuming a flat disc, the vector $\boldsymbol{R}$ from C to S must be in the plane of the disc, which gives the condition

$$\boldsymbol{n} \cdot \boldsymbol{R} = 0\,, \tag{B.5}$$

where we have reintroduced the vector $\boldsymbol{n}$, the normal to the disc plane (such that rotation about $\boldsymbol{n}$ is positive), and we also reintroduce the two normal unit vectors $\boldsymbol{l}$ and $\boldsymbol{m}$ which form a right handed triad with $\boldsymbol{n}$ (e.g. Eqs. 4). A source in the plane of the disc

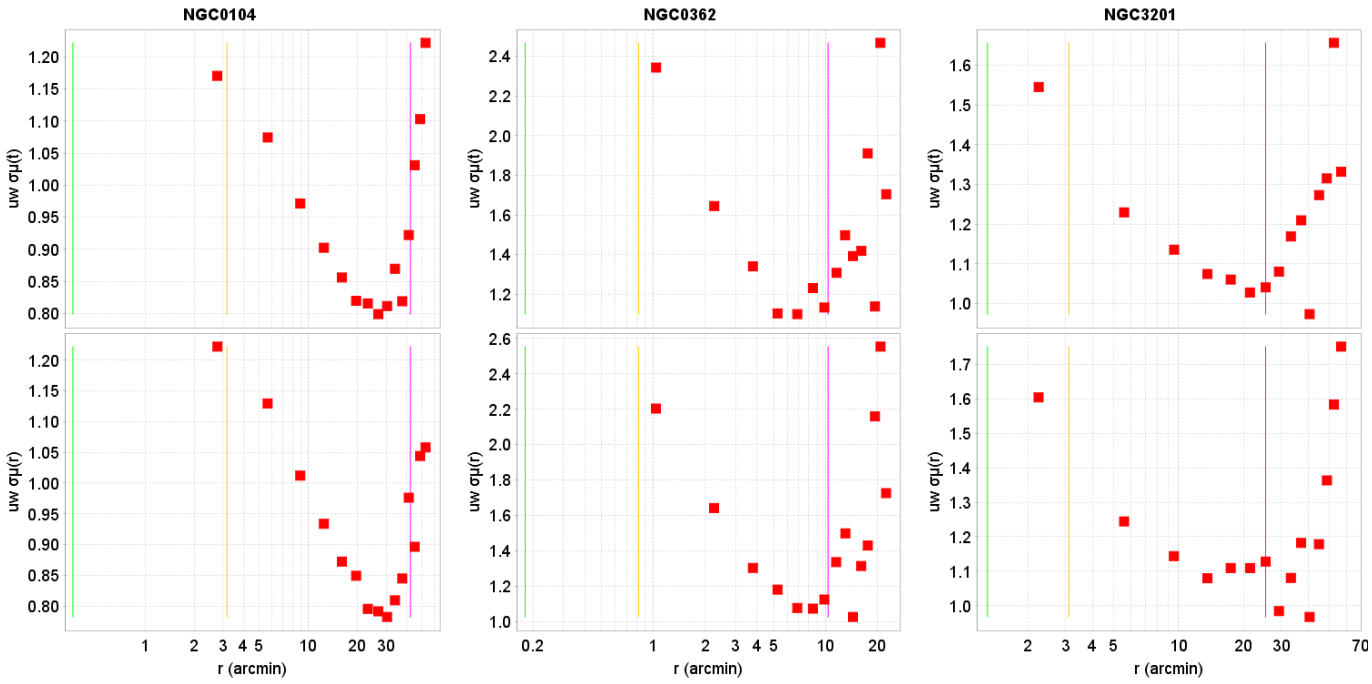


Fig. A.5. Three examples of the proper motion dispersion in the radial and transverse directions as a function of distance to the cluster centre. The three vertical lines indicate, from left to right, the core radius, the half-light radius and the tidal radius following Harris10.

.

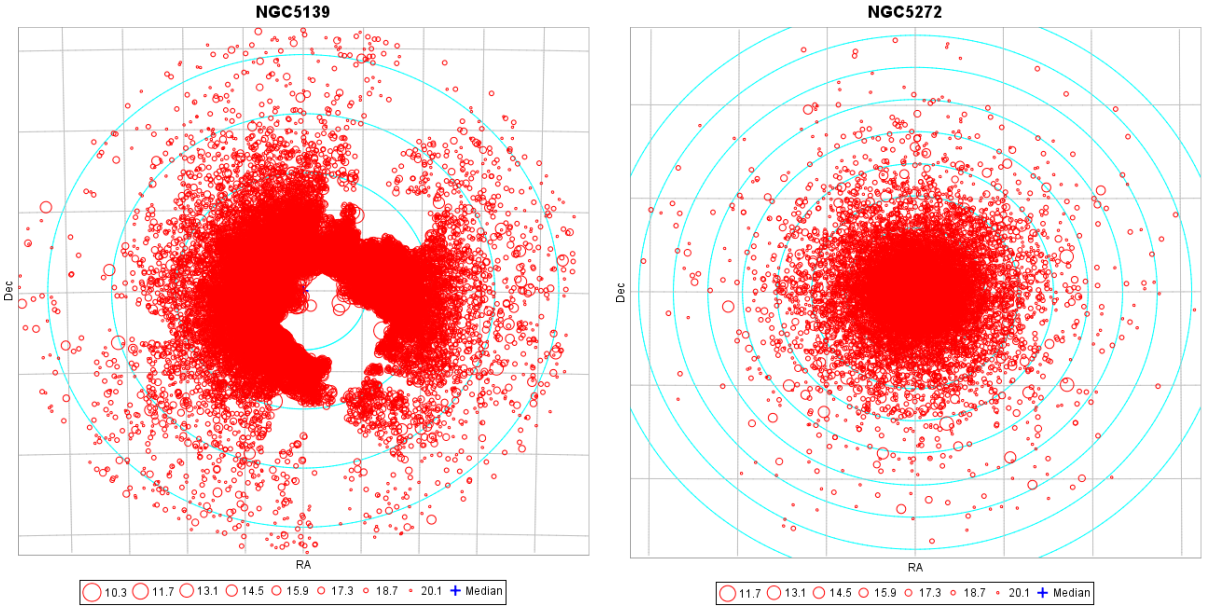


Fig. A.6. Two examples of astrometric data coverage with 5-parameter solutions. On the left, ω Cen, the worst case, on the right NGC 5272, a more average example of coverage. The gaps in the coverage for ω Cen are the result of the filters that have been applied to the astrometric data. The cyan-coloured circles are at intervals of 35 pc in ω Cen and 10 pc in NGC 5272.

can be described in terms of rectangular coordinates ξ, η where

$$\boldsymbol{R} = \boldsymbol{l}\xi + \boldsymbol{m}\eta\,. \tag{B.6}$$

The motion of S is the vectorial sum of the bulk motion (of C) and the peculiar motion of S with respect to C. If we assume that the peculiar motion is circular with angular velocity $\omega(R)$ we have

$$\boldsymbol{v}_S = \boldsymbol{v}_C + (\boldsymbol{m}\xi - \boldsymbol{l}\eta)\,\omega(R)\,, \tag{B.7}$$

where $\boldsymbol{v}_C$ is the bulk motion and $R = \sqrt{\xi^2 + \eta^2}$.

At the reference epoch we can write $\boldsymbol{R}$ in terms of the position of the source $\boldsymbol{s}$ and the centre $\boldsymbol{c}$ as $\boldsymbol{R} = \boldsymbol{s} - \boldsymbol{c} = \boldsymbol{u}s - z$, where s is the distance to the source. Introducing the inverse distance factor $f = s^{-1}$ and inserting in Eq. B.5 gives

$$f = (\boldsymbol{n}\cdot\boldsymbol{u})/n_z = ax + by + z = (1 - x^2 - y^2)^{1/2} + ax + by\,, \tag{B.8}$$

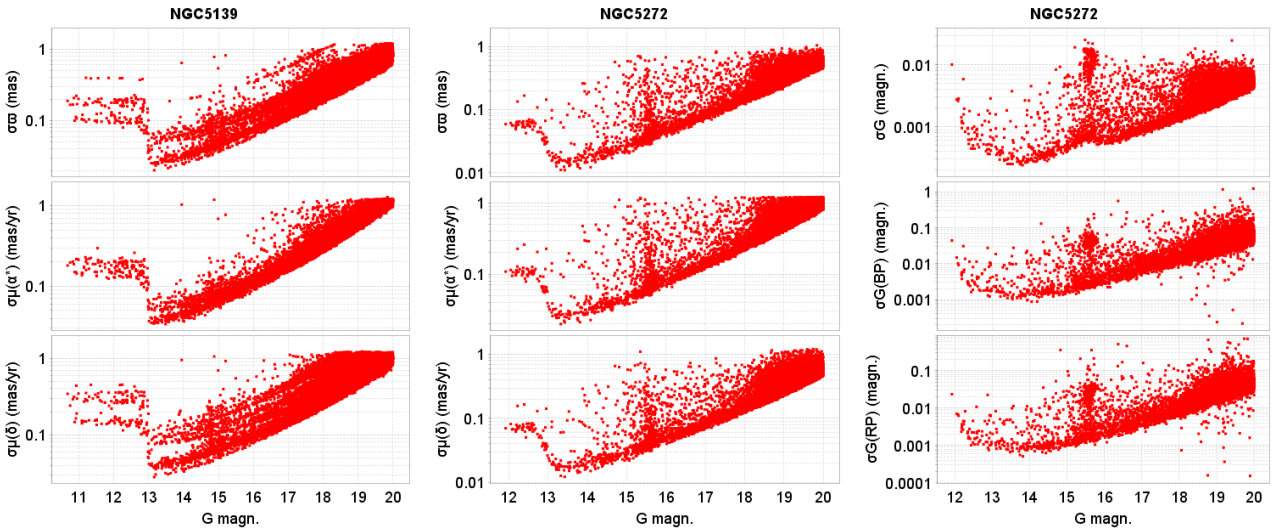


Fig. A.7. From left to right: The standard uncertainties on the astrometric parameters of individual stars as a function of magnitude in ω Cen and NGC 5272, and the standard uncertainties on the photometric data for NGC 5272. The photometric data clearly show the variability of the RR Lyrae stars (around $G = 15.3$), while the astrometric data also show locally much increased uncertainties at the same brightness.

.

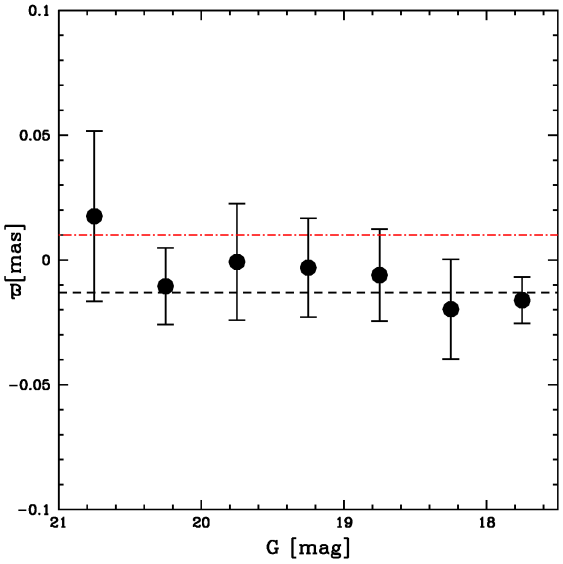


Fig. A.8. Parallax of the stars in the Carina dSph as function of their G magnitude. A clear systematic offset is apparent and significantly measured. The expected parallax (based on literature values) is indicated by the red dashed line.

where

$$a = n_x/n_z, \quad b = n_y/n_z, \tag{B.9}$$

and $n_x = \boldsymbol{x} \cdot \boldsymbol{n}$ etc are the components of $\boldsymbol{n}$ in the xyz system. These components, along with those of $\boldsymbol{l}$ and $\boldsymbol{m}$ and the values a and b are given as a function of the inclination i and the line-of-nodes position angle Ω in the main text (Eqs. 4 & 5). We now find

$$\xi = \boldsymbol{l} \cdot \boldsymbol{R} = \frac{l_x x + l_y x}{z + ax + by}$$
$$\eta = \boldsymbol{m} \cdot \boldsymbol{R} = \frac{(m_x - am_z)x + (m_y - bm_z)y}{z + ax + by} \tag{B.10}$$

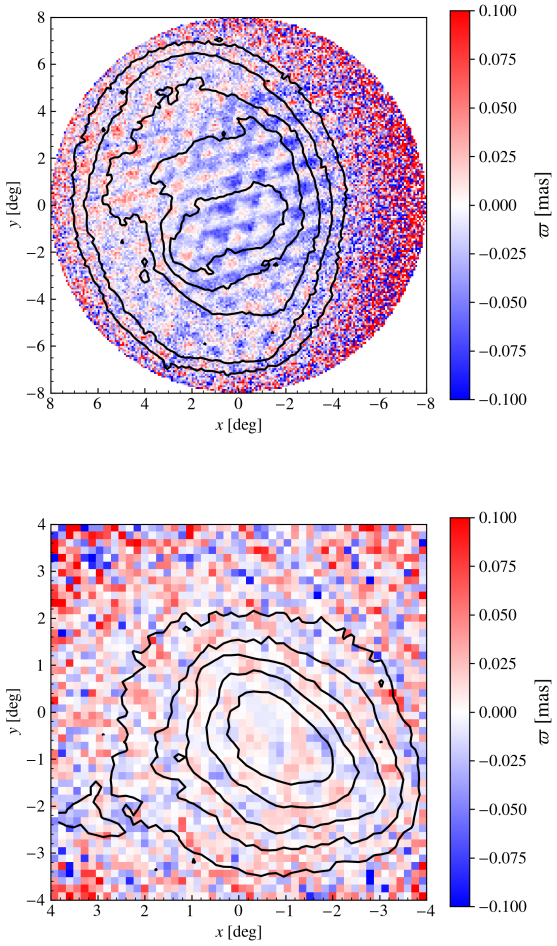


Fig. A.9. Measured parallaxes of stars in the LMC (upper) and SMC (lower). The banding associated with *Gaia*'s scanning law is clearly visible.

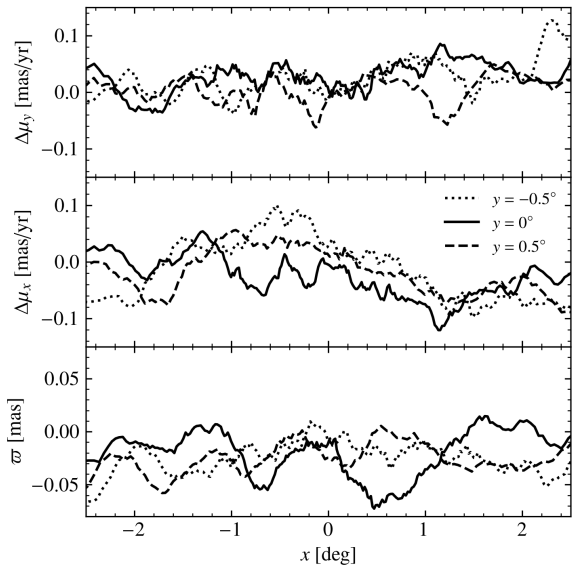


Fig. A.10. Parallaxes and residual proper motions of sources in the LMC. The lines show the median value as a function of coordinate position x for all LMC sources within 0.2° stripes centred at $y = -0.5, 0$ or 0.5°. Residual proper motions are calculated after subtraction of a model disc with parameters determined using only sources within 3° of the centre. The non-zero values are due to both the systematic errors in the *Gaia* data, and the differences between the simple disc model and the true dynamics of the LMC.

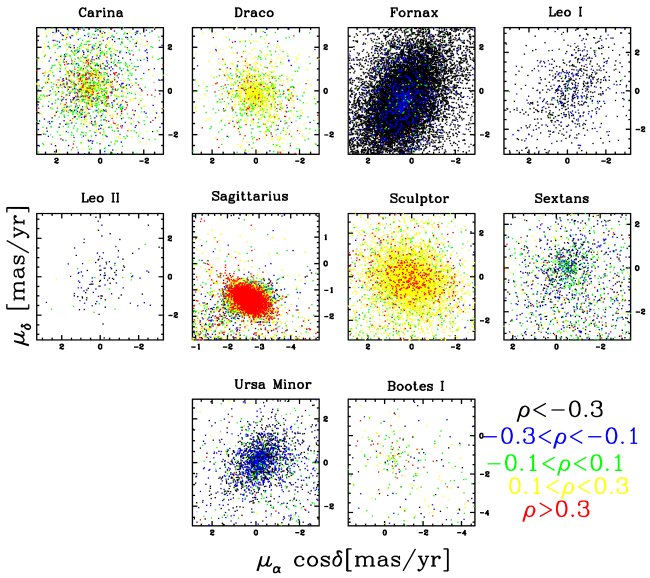


Fig. A.11. Correlations in the proper motions of the stars in the field-of-view towards the different dSph galaxies in our sample. The different colours indicate the amplitude of the correlations.

Turning now to the proper motions, we seek the corresponding relationships between $(\dot{x}, \dot{y})$ and $(\dot{\xi}, \dot{\eta})$. We know that

$$\dot{\xi} = -\eta\,\omega(R), \quad \dot{\eta} = \xi\,\omega(R). \tag{B.11}$$

The proper motion vector is

$$\dot{\boldsymbol{u}} = \frac{\mathrm{d}(\boldsymbol{s}f)}{\mathrm{d}t} = (\boldsymbol{v}_S - \boldsymbol{u}(\boldsymbol{u}\cdot\boldsymbol{v}_S))\,f\,, \tag{B.12}$$

which, using our previous results, we can rewrite as

$$\dot{\boldsymbol{u}} = (\boldsymbol{v}_C - \boldsymbol{u}(\boldsymbol{u}\cdot\boldsymbol{v}_C))\,(ax+by+z) \;+((\boldsymbol{m}-\boldsymbol{u}(\boldsymbol{u}\cdot\boldsymbol{m}))(l_x x + l_y y) - (\boldsymbol{l}-\boldsymbol{u}(\boldsymbol{u}\cdot\boldsymbol{l}))((m_x - am_z)x + (m_y - bm_z)y))\;\omega(R)\,. \tag{B.13}$$

Taking the scalar products with $\boldsymbol{x}$ and $\boldsymbol{y}$ gives explicit expressions for $\dot{x}$ and $\dot{y}$ as functions of x and y. If ω is constant, the expressions contain terms up to the third power in x and y. At C $(x = y = 0)$ we find, as expected,

$$\dot{x} = v_x, \quad \dot{y} = v_y, \tag{B.14}$$

where v_x, v_y, v_z, etc are the components of $\boldsymbol{v}_C$ in the xyz system.

Retaining only first-order terms in x and y while assuming constant ω, and then taking derivatives, we have

$$\begin{aligned}
\partial\dot{x}/\partial x &= av_x - v_z + al_x m_z\omega,\\
\partial\dot{x}/\partial y &= bv_x - n_z\omega + bl_x m_z\omega,\\
\partial\dot{y}/\partial x &= av_y + n_z\omega + al_y m_z\omega,\\
\partial\dot{y}/\partial y &= bv_y - v_z + bl_y m_z\omega,
\end{aligned} \tag{B.15}$$

which hold exactly at C if $\mathrm{d}\omega(r)/\mathrm{d}R = 0$ for $R = 0$. It is these equations (writing $\dot{x}, \dot{y}$ as μ_x, μ_y) which we have used in this study to find v_z, i, Ω, and ω.

The orientation of the LMC plane is given by the unit vector $\boldsymbol{n}$, the direction of which is conventionally given by the two angles i and Ω:

$$\boldsymbol{n} = \boldsymbol{x}\sin i\cos\Omega - \boldsymbol{y}\sin i\sin\Omega + \boldsymbol{z}\cos i\,, \tag{B.16}$$

from which (with the definition of $\boldsymbol{l}$ and $\boldsymbol{m}$) we have the components of all three of these vectors in the xyz system, as given in Eq. 4.

Appendix B.3: Estimating the kinematic parameters for fixed C and constant ω

From Eq. B.15 we see that $(\dot{x}, \dot{y})$ should vary linearly with (x, y) for constant ω. This is a reasonable approximation in the inner few degrees of the LMC. Fitting the linear relation

$$\begin{aligned}
\dot{x} &= v_x + A_x x + A_y y\\
\dot{y} &= v_y + B_x x + B_y y
\end{aligned} \tag{B.17}$$

we immediately obtain estimates of v_x, v_y, and the four gradients $\partial\dot{x}/\partial x = A_x$, etc. We can use Eqs. B.15 to express these gradients as functions of the six kinematic parameters v_x, v_y, v_z, i, Ω, and ω (assumed constant). In this study we usually then hold v_z constant, in which case we vary i, Ω, and ω to minimise the sum of the square residuals

$$S = (\partial\dot{x}/\partial x - A_x)^2 + (\partial\dot{x}/\partial y - A_y)^2 + (\partial\dot{y}/\partial x - B_x)^2 + (\partial\dot{y}/\partial y - B_y)^2 \tag{B.18}$$

where A_x etc. are measured from the data, and $\partial\dot{x}/\partial x$ are predictions of the model. We can also leave v_z free, in which case Eqs. B.15 can be directly solved to determine v_z, i, Ω, and ω.

Appendix B.4: De-projection method

The observed proper motions, or $\dot{x}$, $\dot{y}$, are the projections of the true space motions on the celestial sphere, or normal to $\boldsymbol{z}$. This projection from 3D to 2D cannot be inverted, but if we assume that the true motions are confined to the (known) plane of the LMC, it is possible to project the observed motions back to that plane. We call this de-projection.

We assume that $\boldsymbol{v}_C$, i, and Ω are known. The starting point is Eq. B.12, but with the velocity of S written as

$$\boldsymbol{v}_S = \boldsymbol{v}_C + \boldsymbol{l}\dot{\xi} + \boldsymbol{m}\dot{\eta}\,, \tag{B.19}$$

which allows arbitrary motions in the plane. We have then

$$\dot{\boldsymbol{u}} = (\boldsymbol{v}_C - \boldsymbol{u}(\boldsymbol{u}\cdot\boldsymbol{v}_C))\,f + (\boldsymbol{l} - \boldsymbol{u}(\boldsymbol{u}\cdot\boldsymbol{l}))f\dot{\xi} + (\boldsymbol{m} - \boldsymbol{u}(\boldsymbol{u}\cdot\boldsymbol{m}))f\dot{\eta}\,. \tag{B.20}$$

Taking the scalar products with $\boldsymbol{x}$ and $\boldsymbol{y}$ gives two linear equations

$$\begin{aligned}(l_x - x(l_x x + l_y y))\dot{\xi} + (m_x - x(m_x x + m_y y + m_z z))\dot{\eta} \\ = (\dot{x} - v_x + x(v_x x + v_y y + v_z z))/(ax + by + z)\end{aligned}$$

$$\begin{aligned}(l_y - y(l_x x + l_y y))\dot{\xi} + (m_y - y(m_x x + m_y y + m_z z))\dot{\eta} \\ = (\dot{y} - v_y + y(v_x x + v_y y + v_z z))/(ax + by + z)\end{aligned} \tag{B.21}$$

from which $\dot{\xi}$ and $\dot{\eta}$ can be solved. The corresponding position (ξ, η) is obtained from (B.10).

For mapping the kinematics of the LMC it is more convenient to transform the Cartesian $(\xi, \eta, \dot{\xi}, \dot{\eta})$ to polar coordinates R, ϕ and the corresponding velocity components v_R (in the direction of increasing R) and v_T (tangential velocity), as in Figure 18.

Appendix C: The globular clusters and dSph solution data

Table B.1. Parameters of LMC based on sources with angular radii from the assumed LMC centre (ρ) in various ranges (with or without binning – see Section 5.1). We show the derived parameters when we leave v_z free, or when we hold it fixed (the parameters are derived from the gradients so the gradients are the same in either case).

ρ [deg]	v_x [mas/yr]	v_y [mas/yr]	$\partial\mu_x/\partial x$ [mas/yr /rad]	$\partial\mu_x/\partial y$ [mas/yr /rad]	$\partial\mu_y/\partial x$ [mas/yr /rad]	$\partial\mu_y/\partial y$ [mas/yr /rad]	N	v_z [mas/yr]	$v_{z,\mathrm{const}}$ [mas/yr]	i [deg]	Ω [deg]	ω [mas/yr]
< 2.0	1.848	0.236	-2.256	-5.441	4.838	-0.225	2482275	1.930		61.497	-73.577	5.217
< 2.0									1.104	40.008	-68.576	5.643
< 3.0	1.850	0.234	-1.577	-4.565	4.765	-0.284	4295125	1.493		53.097	-70.263	5.095
< 3.0									1.104	33.982	-61.916	5.095
< 4.0	1.849	0.234	-1.330	-3.936	4.543	-0.420	5757649	1.407		48.038	-66.336	4.740
< 4.0									1.104	30.795	-55.251	4.604
< 5.0	1.849	0.235	-1.183	-3.493	4.337	-0.482	6610213	1.379		45.600	-62.242	4.410
< 5.0									1.104	30.018	-49.346	4.236
< 6.0	1.849	0.237	-1.046	-3.134	4.092	-0.511	7279181	1.328		44.155	-59.946	4.104
< 6.0									1.104	30.108	-45.378	3.909
Annuli												
1.0–2.0	1.847	0.230	-2.164	-5.389	4.860	-0.245	1679866	1.864		60.448	-73.439	5.259
1.0–2.0									1.104	39.175	-68.368	5.623
2.0–3.0	1.847	0.231	-1.278	-4.255	4.751	-0.302	1812850	1.308		48.064	-67.135	4.990
2.0–3.0									1.104	31.471	-55.591	4.870
3.0–4.0	1.841	0.238	-1.032	-3.429	4.297	-0.528	1462524	1.281		41.805	-60.172	4.336
3.0–4.0									1.104	28.524	-45.464	4.142
4.0–5.0	1.833	0.251	-0.941	-2.741	3.794	-0.521	852564	1.296		43.761	-58.173	3.750
4.0–5.0									1.104	30.984	-42.516	3.546
5.0–6.0	1.835	0.264	-0.701	-2.300	3.215	-0.477	668968	1.024		39.870	-64.539	3.285
5.0–6.0									1.104	31.528	-41.959	3.033
Using binned data												
< 2.0	1.850	0.219	-2.341	-5.791	5.376	-0.552		2.041		56.399	-71.686	5.807
< 2.0									1.104	35.461	-68.997	6.061
< 3.0	1.846	0.220	-1.482	-4.778	5.198	-0.349		1.449		48.161	-65.873	5.428
< 3.0									1.104	30.938	-57.200	5.359
< 4.0	1.842	0.226	-1.217	-3.924	4.701	-0.447		1.367		44.841	-61.545	4.779
< 4.0									1.104	29.534	-49.547	4.627
< 5.0	1.838	0.239	-1.058	-3.231	4.064	-0.452		1.270		45.039	-63.705	4.165
< 5.0									1.104	30.549	-48.400	3.964
< 6.0	1.837	0.255	-0.919	-2.704	3.387	-0.414		1.058		46.981	-74.732	3.686
< 6.0									1.104	32.097	-52.666	3.407

Table B.2. Parameters of SMC, with assumed v_z value.

r_{max} [deg]	v_x [mas/yr]	v_y [mas/yr]	$\partial\mu_x/\partial x$ [mas/yr /rad]	$\partial\mu_x/\partial y$ [mas/yr /rad]	$\partial\mu_y/\partial x$ [mas/yr /rad]	$\partial\mu_y/\partial y$ [mas/yr /rad]	N	$v_{z,\mathrm{const}}$ [mas/yr]	i [deg]	Ω [deg]	ω [mas/yr]
< 2.0	0.794	-1.219	1.960	0.831	-2.117	0.030	935265	0.489	73.995	-6.613	0.595
< 3.0	0.797	-1.220	2.247	0.383	-1.932	0.067	1219082	0.489	74.199	-1.682	0.643
< 4.0	0.799	-1.221	2.295	0.253	-1.948	0.176	1343140	0.489	73.678	1.257	0.610
Annuli											
1.0–2.0	0.797	-1.219	2.014	0.715	-2.269	0.094	543224	0.489	73.046	-3.293	0.497
2.0–3.0	0.810	-1.234	2.632	0.128	-1.929	-0.090	283817	0.489	75.568	-0.464	0.711
3.0–4.0	0.824	-1.235	2.455	0.150	-2.019	0.299	124058	0.489	73.549	3.676	0.591
Using binned data											
< 2.0	0.796	-1.225	2.709	0.300	-2.585	0.242		0.489	75.581	2.178	0.528
< 3.0	0.804	-1.233	2.959	-0.027	-2.329	0.340		0.489	75.895	5.386	0.609
< 4.0	0.817	-1.237	2.671	-0.054	-2.215	0.417		0.489	74.195	7.082	0.557

Table C.1. Overview of the results for globular clusters. For each cluster we list their NGC name as well as the SIMBAD identifier, as well as the derived position on the sky (α, δ), parallax ϖ, proper motions ($\mu_{\alpha*}$, μ_δ) and the elements of the covariance matrix ϵ_ϖ, $\epsilon_{\mu\alpha*}$, $\epsilon_{\mu\delta}$ and correlation coefficients C. The entry r(max)°corresponds to the maximum radius at which proper motion members have been found, nMemb is the number of members used to derive the astrometric parameters, and uwsd$_{astr}$ is the unit-weight standard deviation of the astrometric solution. Lastly Vrad, ϵ_{Vr}, uwsd$_{Vr}$, and N_{Vr} are the mean radial velocity derived from *Gaia* DR2 data, its error, the unit-weight standard deviation for the radial velocity solution and the number of stars used to derive these quantities, respectively

Name ClustId	α δ [deg]	ϖ ϵ_ϖ [mas]	$\mu_{\alpha*}$ $\epsilon_{\mu\alpha*}$ [mas yr^{-1}]	μ_δ $\epsilon_{\mu\delta}$ [mas yr^{-1}]	C$_{\varpi,\mu_\alpha}$ C$_{\varpi,\mu_\delta}$	C$_{\mu_\alpha,\mu_\delta}$ r(max)°	nMemb uwsd$_{astr}$	Vrad ϵ_{Vr} [km s^{-1}]	uwsd$_{Vr}$ N_{Vr}
NGC0104	6.0194	0.1959	5.2477	-2.5189	-0.01	-0.06	60093	-18.95	11.55
C0021-723	-72.0821	0.0002	0.0016	0.0015	-0.01	0.90	0.79	0.42	229
NGC0288	13.1879	0.1401	4.2385	-5.6470	0.15	0.25	5897	-49.06	2.87
C0050-268	-26.5858	0.0021	0.0035	0.0026	-0.13	0.33	0.99	0.32	11
NGC0362	15.8099	0.0788	6.6954	-2.5184	-0.04	-0.09	6896	226.93	6.06
C0100-711	-70.8489	0.0012	0.0045	0.0034	-0.12	0.39	1.23	0.77	19
NGC1851	78.5280	0.0298	2.1308	-0.6220	0.06	-0.09	4044	323.36	3.74
C0512-400	-40.0456	0.0011	0.0037	0.0040	-0.07	0.28	1.07	1.04	17
NGC1904	81.0463	0.0362	2.4702	-1.5603	0.05	-0.03	2363	206.43	2.94
C0522-245	-24.5255	0.0017	0.0048	0.0054	0.04	0.14	1.14	0.87	14
NGC2298	102.2464	0.0791	3.2762	-2.1913	0.08	0.07	1373	147.41	1.54
C0647-359	-36.0046	0.0019	0.0060	0.0061	-0.07	0.16	1.06	1.40	4
NGC2808	138.0071	0.0560	1.0032	0.2785	0.05	-0.08	6769	104.61	5.33
C0911-646	-64.8645	0.0006	0.0032	0.0032	-0.01	0.39	0.87	1.26	20
NGC3201	154.3987	0.1724	8.3344	-1.9895	0.04	0.12	19921	494.62	5.09
C1015-461	-46.4125	0.0006	0.0021	0.0020	-0.02	0.98	0.97	0.37	64
NGC4372	186.4587	0.1426	-6.3898	3.3266	0.03	0.01	10744	77.41	5.50
C1223-724	-72.6562	0.0006	0.0030	0.0025	0.03	0.46	0.83	0.58	42
NGC4590	189.8651	0.0664	-2.7640	1.7916	-0.00	-0.29	3338		
C1236-264	-26.7454	0.0025	0.0050	0.0039	0.13	0.24	0.99		0
NGC4833	194.8978	0.1163	-8.3147	-0.9366	0.05	0.06	6269	207.86	5.97
C1256-706	-70.8718	0.0010	0.0036	0.0029	0.11	0.19	0.93	0.57	40
NGC5024	198.2262	0.0143	-0.1466	-1.3514	-0.12	-0.28	2637	-64.33	
C1310+184	18.1661	0.0018	0.0045	0.0032	0.08	0.26	1.14		1
NGC5053	199.1124	0.0064	-0.3591	-1.2586	0.13	-0.32	918		
C1313+179	17.7008	0.0040	0.0071	0.0048	-0.17	0.13	0.90		0
NGC5139	201.7876	0.1237	-3.1925	-6.7445	-0.04	-0.03	32700	235.12	11.73
C1323-472	-47.4515	0.0011	0.0022	0.0019	0.17	1.09	0.91	0.59	88
NGC5272	205.5486	0.0265	-0.1127	-2.6274	-0.01	-0.03	12057	-146.48	5.54
C1339+286	28.3760	0.0010	0.0029	0.0022	-0.05	0.47	1.01	0.66	35
NGC5286	206.6136	0.0168	0.1836	-0.1477	-0.02	-0.01	1649	56.80	1.97
C1343-511	-51.3723	0.0025	0.0076	0.0068	0.08	0.16	1.21	1.66	7
NGC5466	211.3614	0.0210	-5.4044	-0.7907	0.04	0.07	1772	109.41	0.41
C1403+287	28.5331	0.0021	0.0042	0.0041	0.15	0.15	0.93	0.31	2
NGC5634	217.4053	0.0039	-1.7309	-1.5283	-0.06	-0.02	602		
C1427-057	-5.9773	0.0047	0.0087	0.0074	0.06	0.09	1.04		0
NGC5897	229.3515	0.0680	-5.4108	-3.4595	-0.02	-0.12	2613	99.92	1.77
C1514-208	-21.0115	0.0026	0.0053	0.0045	0.02	0.18	0.96	1.31	5
NGC5904	229.6394	0.1135	4.0613	-9.8610	-0.07	0.03	11741	54.54	7.56
C1516+022	2.0766	0.0010	0.0032	0.0029	0.09	0.56	0.98	0.86	61
NGC5927	232.0065	0.0996	-5.0470	-3.2325	-0.00	-0.08	2621		
C1524-505	-50.6694	0.0021	0.0060	0.0055	-0.01	0.15	0.92		0
NGC5946	233.8711	0.0444	-5.1909	-1.6522	-0.04	-0.10	757	131.88	
C1531-504	-50.6617	0.0047	0.0124	0.0101	-0.06	0.09	0.94		1
NGC5986	236.5211	0.0718	-4.2217	-4.5515	-0.10	-0.18	2477	98.90	2.38
C1542-376	-37.7826	0.0031	0.0084	0.0065	-0.01	0.16	1.38	1.06	11
NGC6093	244.2564	0.0558	-2.9469	-5.5613	-0.10	0.01	1927	12.01	8.34
C1614-228	-22.9723	0.0030	0.0090	0.0073	0.06	0.16	1.23	1.70	16
NGC6121	245.8976	0.5001	-12.4956	-18.9789	-0.08	0.08	19508	71.40	7.79
C1620-264	-26.5279	0.0007	0.0033	0.0030	0.03	1.13	1.02	0.30	182
NGC6144	246.8061	0.0668	-1.7646	-2.6371	-0.15	0.08	1882	195.85	1.38
C1624-259	-26.0301	0.0040	0.0085	0.0063	0.15	0.17	1.16	0.90	3
NGC6171	248.1350	0.1480	-1.9359	-5.9487	-0.13	0.03	4032	-35.01	6.94
C1629-129	-13.0570	0.0026	0.0064	0.0048	0.17	0.33	1.08	0.89	15

Continued on next page

Table C.1 – continued from previous page

Name ClustId	α δ [deg]	ϖ ϵ_ϖ [mas]	$\mu_{\alpha*}$ $\epsilon_{\mu\alpha*}$ [mas yr^{-1}]	μ_δ $\epsilon_{\mu\delta}$ [mas yr^{-1}]	C_{ϖ,μ_α} C_{ϖ,μ_δ}	$C_{\mu_\alpha,\mu_\delta}$ r(max)°	nMemb uwsd$_{astr}$	Vrad ϵ_{Vr} [km s^{-1}]	uwsd$_{Vr}$ N_{Vr}
NGC6205	250.4217	0.0801	-3.1762	-2.5876	-0.04	0.19	15634	-245.62	9.79
C1639+365	36.4596	0.0007	0.0027	0.0030	0.04	0.58	1.07	0.94	65
NGC6218	251.8101	0.1563	-0.1577	-6.7683	-0.06	0.29	10488	-41.00	5.24
C1644-018	-1.9510	0.0013	0.0040	0.0027	0.11	0.38	1.08	0.51	38
NGC6235	253.3557	0.0618	-3.9442	-7.5615	-0.18	0.25	882		
C1650-220	-22.1798	0.0078	0.0130	0.0067	0.37	0.15	1.43		0
NGC6254	254.2861	0.1511	-4.7031	-6.5285	-0.07	0.21	13005	76.76	5.89
C1654-040	-4.0981	0.0014	0.0039	0.0027	0.10	0.47	1.12	0.59	61
NGC6266	255.2821	0.2187	-5.3269	-2.9818	-0.11	0.23	3096	-74.86	3.84
C1658-300	-30.0938	0.0036	0.0082	0.0052	0.16	0.17	1.01	0.79	14
NGC6273	255.6561	0.0924	-3.2237	1.6059	-0.07	0.15	4977	141.29	2.94
C1659-262	-26.2696	0.0022	0.0069	0.0050	0.11	0.21	1.44	1.00	16
NGC6284	256.1187	0.0499	-3.1882	-2.0479	-0.16	0.20	911	30.29	1.71
C1701-246	-24.7662	0.0056	0.0112	0.0075	0.19	0.10	1.06	1.80	6
NGC6287	256.2882	0.1074	-4.8866	-1.9208	0.02	0.06	1518	-292.45	2.62
C1702-226	-22.7183	0.0049	0.0117	0.0083	0.19	0.13	1.29	0.81	3
NGC6293	257.5413	0.0696	0.8225	-4.3070	-0.10	0.20	1036	-143.65	1.70
C1707-265	-26.5799	0.0049	0.0093	0.0064	0.26	0.09	1.04	0.67	2
NGC6304	258.6370	0.1077	-3.9478	-1.1248	-0.04	0.16	1322	-111.70	5.37
C1711-294	-29.4816	0.0034	0.0095	0.0069	0.13	0.16	1.05	1.33	6
NGC6316	259.1534	0.0659	-4.8215	-4.6140	-0.19	0.23	961		
C1713-280	-28.1532	0.0094	0.0146	0.0095	0.34	0.10	1.22		0
NGC6325	259.4962	0.1431	-8.3777	-9.0067	-0.33	0.17	392		
C1714-237	-23.7668	0.0160	0.0195	0.0135	0.34	0.09	1.29		0
NGC6333	259.8021	0.0934	-2.2028	-3.2084	-0.01	0.19	3478		
C1716-184	-18.5146	0.0027	0.0075	0.0056	0.15	0.09	1.40		0
NGC6341	259.2821	0.0564	-4.9367	-0.5559	-0.04	0.11	7079	-118.81	5.56
C1715+432	43.1352	0.0008	0.0040	0.0040	-0.00	0.26	1.11	0.62	26
NGC6342	260.2983	0.0973	-2.9475	-7.0059	-0.01	0.14	1121	118.97	
C1718-195	-19.6050	0.0057	0.0112	0.0083	0.22	0.13	1.05		1
NGC6352	261.3739	0.1543	-2.1889	-4.4209	-0.12	0.22	7255	-123.25	2.80
C1721-484	-48.4270	0.0018	0.0046	0.0036	0.13	0.18	1.01	0.63	12
NGC6356	260.8898	0.0791	-3.7683	-3.3746	-0.24	0.27	2021		
C1720-177	-17.8128	0.0066	0.0096	0.0063	0.31	0.09	1.59		0
NGC6362	262.9772	0.0974	-5.5014	-4.7417	-0.06	0.06	9169		
C1725-050	-67.0492	0.0011	0.0028	0.0032	0.06	0.26	1.12		0
NGC6366	261.9393	0.2292	-0.3835	-5.1309	-0.08	0.27	7108		
C1726-670	-5.0752	0.0022	0.0054	0.0044	0.14	0.36	1.09		0
NGC6380	263.6202	0.1014	-2.0984	-3.1922	-0.25	-0.05	988		
C1731-390	-39.0694	0.0163	0.0183	0.0125	0.49	0.07	1.64		0
NGC6388	264.0654	0.0482	-1.3548	-2.7144	-0.12	0.11	3912	80.00	4.18
C1732-447	-44.7423	0.0034	0.0072	0.0061	0.18	0.11	1.51	2.49	9
NGC6397	265.1697	0.3781	3.2908	-17.5908	-0.05	0.10	22116	19.18	8.00
C1736-536	-53.6773	0.0007	0.0026	0.0025	0.07	0.76	0.96	0.46	79
NGC6401	264.6581	0.1156	-2.8193	1.4424	-0.03	0.07	484		
C1735-238	-23.9173	0.0055	0.0116	0.0095	0.15	0.11	0.94		0
NGC6402	264.3984	0.0536	-3.6146	-5.0357	-0.08	0.17	4203		
C1735-032	-3.2473	0.0027	0.0067	0.0059	0.15	0.20	1.33		0
NGC6440	267.2028	0.0958	-1.2135	-3.8830	-0.05	0.29	1033	-72.58	1.75
C1746-203	-20.3521	0.0058	0.0124	0.0096	0.15	0.09	0.97	0.69	2
NGC6441	267.5540	0.0403	-2.5394	-5.3010	-0.18	0.17	2121		
C1746-370	-37.0660	0.0037	0.0070	0.0057	0.17	0.12	1.03		0
NGC6453	267.7197	0.0425	0.0699	-5.8521	-0.11	0.14	710	-94.94	0.52
C1748-346	-34.6002	0.0077	0.0164	0.0136	0.13	0.07	1.65	1.06	2
NGC6496	269.7677	0.0803	-3.0290	-9.1971	-0.15	0.07	1860		
C1755-442	-44.2660	0.0031	0.0057	0.0050	0.17	0.13	0.87		0
NGC6517	270.4528	0.0217	-1.5209	-4.2622	-0.15	0.28	880	-32.45	
C1759-089	-8.9568	0.0072	0.0139	0.0114	0.11	0.08	1.20		1
NGC6522	270.8956	0.0697	2.5780	-6.3412	-0.02	0.12	474	-17.26	0.32
C1800-300	-30.0350	0.0050	0.0124	0.0109	0.09	0.09	1.00	0.38	2
NGC6528	271.2039	0.0746	-2.1879	-5.5718	0.04	0.11	354		
C1801-300	-30.0550	0.0074	0.0160	0.0137	0.08	0.05	0.94		0
NGC6535	270.9590	0.1294	-4.2101	-2.9461	0.10	0.10	740	-211.40	1.36
C1801-003	-0.2953	0.0047	0.0115	0.0108	-0.02	0.11	0.87	0.30	2
NGC6539	271.1924	0.0630	-6.8310	-3.4792	-0.44	0.18	1149		

Continued on next page

Table C.2. Overview of the astrometric parameters for dwarf spheroidal galaxies. For each dSph we include the derived position on the sky (α, δ), parallax ϖ, proper motions ($\mu_{\alpha*}$, μ_δ) and the elements of the covariance matrix ϵ_ϖ, $\epsilon_{\mu\alpha*}$, $\epsilon_{\mu\delta}$ and correlation coefficients C. The last two columns give respectively, the number of stars and the magnitude limit used for the determination of the astrometric parameters. Note that the (α, δ) listed here are determined from stars with 5-parameter solutions, and hence these coordinates might not provide the most accurate estimate of the centre of the dSph because of incompleteness in the spatial coverage of such solutions (see e.g. Fig. 2). Therefore for the orbital integrations in Sec. 6 we use (α, δ) sky coordinates from the literature.

Name	α [deg]	δ [deg]	ϖ [mas]	ϵ_ϖ [mas]	μ_{α^*} [mas/yr]	$\epsilon_{\mu_{\alpha^*}}$ [mas/yr]	μ_δ [mas/yr]	ϵ_{μ_δ} [mas/yr]	C_{ϖ,μ_α}	C_{ϖ,μ_δ}	$C_{\mu_\alpha,\mu_\delta}$	nMemb	G_{lim} [mag]
Fnx	39.9971	-34.4492	-0.054	0.002	0.376	0.003	-0.413	0.003	0.16	-0.46	-0.09	7722	19.9
Dra	260.0517	57.9153	-0.052	0.005	-0.019	0.009	-0.145	0.010	-0.18	0.12	-0.08	422	19.5
Car	100.4029	-50.9661	-0.015	0.005	0.495	0.015	0.143	0.014	-0.00	0.02	-0.08	257	19.1
U Min	227.2854	67.2225	-0.039	0.006	-0.182	0.010	0.074	0.008	-0.01	-0.31	-0.34	925	19.8
Sext	153.2625	-1.6147	-0.102	0.023	-0.496	0.025	0.077	0.020	0.28	-0.10	-0.45	205	19.7
Leo I	152.1171	12.3064	-0.214	0.065	-0.097	0.056	-0.091	0.047	0.29	-0.30	-0.51	174	19.9
Leo II	168.3700	22.1517	-0.001	0.037	-0.064	0.057	-0.210	0.054	-0.18	-0.24	0.05	116	20.0
Sgr	283.8313	-30.5453	0.003	0.001	-2.692	0.001	-1.359	0.001	-0.17	0.21	0.09	23109	18.0
Scl	15.0392	-33.7092	-0.013	0.004	0.082	0.005	-0.131	0.004	0.17	0.15	0.23	1592	19.5
Boo I	210.025	14.500	-0.069	0.024	-0.459	0.041	-1.064	0.029	0.01	0.11	0.16	115	19.7

Table C.1 – continued from previous page

Name ClustId	α δ [deg]	ϖ ϵ_ϖ [mas]	$\mu_{\alpha*}$ $\epsilon_{\mu\alpha*}$ [mas yr^{-1}]	μ_δ $\epsilon_{\mu\delta}$ [mas yr^{-1}]	C_{ϖ,μ_α} C_{ϖ,μ_δ}	$C_{\mu_\alpha,\mu_\delta}$ r(max)°	nMemb uwsd$_{astr}$	Vrad ϵ_{Vr} [km s^{-1}]	uwsd$_{Vr}$ N_{Vr}
C1802-075	-7.5896	0.0084	0.0106	0.0085	0.22	0.26	1.38		0
NGC6541	271.9827	0.1139	0.2762	-8.7659	-0.04	-0.03	2987	-164.64	1.97
C1804-437	-43.7144	0.0025	0.0054	0.0048	0.08	0.27	0.91	1.09	8
NGC6544	271.8438	0.3311	-2.3280	-18.5574	-0.04	0.11	3266	-27.06	7.35
C1804-250	-25.0186	0.0022	0.0089	0.0083	0.04	0.25	1.03	0.76	5
NGC6626	276.1349	0.1469	-0.4236	-8.8037	-0.15	0.07	1969	14.55	4.41
C1821-249	-24.8430	0.0033	0.0087	0.0082	0.12	0.19	1.04	0.76	17
NGC6637	277.8342	0.0746	-5.0669	-5.8017	-0.01	0.23	773	47.19	2.61
C1828-323	-32.3565	0.0032	0.0104	0.0094	-0.05	0.10	0.93	1.71	3
NGC6656	279.1048	0.2602	9.8019	-5.5643	-0.05	0.15	16261	-147.60	13.11
C1833-239	-23.9102	0.0009	0.0036	0.0034	0.02	0.85	1.01	0.57	116
NGC6681	280.8020	0.1096	1.3853	-4.7174	-0.24	0.26	1276	215.87	0.23
C1840-323	-32.2892	0.0038	0.0076	0.0065	0.10	0.08	0.99	0.35	2
NGC6752	287.7175	0.2310	-3.1908	-4.0347	-0.29	0.19	23684	-26.12	7.82
C1906-600	-59.9833	0.0011	0.0018	0.0020	0.03	0.55	1.02	0.51	82
NGC6779	289.1480	0.0702	-2.0092	1.6553	-0.05	0.03	2379	-136.67	2.56
C1914+300	30.1840	0.0015	0.0051	0.0056	-0.03	0.12	1.15	1.00	11
NGC6809	295.0046	0.1707	-3.4017	-9.2642	-0.03	0.18	13046	176.46	4.64
C1936-310	-30.9621	0.0011	0.0031	0.0028	0.00	0.28	0.90	0.57	47
NGC6838	298.4427	0.2252	-3.3842	-2.6528	-0.11	0.11	6766	-21.01	3.96
C1951+186	18.7790	0.0010	0.0027	0.0028	-0.01	0.19	0.90	0.53	22
NGC6864	301.5205	0.0208	-0.5869	-2.7839	-0.35	0.21	946	-185.33	0.72
C2003-220	-21.9213	0.0066	0.0088	0.0065	-0.22	0.05	1.46	1.51	3
NGC6981	313.3662	0.0225	-1.2488	-3.3117	-0.38	0.26	974		
C2050-127	-12.5386	0.0063	0.0089	0.0068	-0.13	0.18	1.26		0
NGC7078	322.4949	0.0568	-0.6238	-3.7960	-0.02	-0.04	4479	-105.58	5.29
C2127+119	12.1661	0.0014	0.0041	0.0039	-0.15	0.40	0.87	1.45	12
NGC7089	323.3497	0.0591	3.4911	-2.1501	-0.14	-0.04	1259	-4.79	1.42
C2130-010	-0.8177	0.0035	0.0077	0.0071	-0.14	0.20	1.03	0.27	5
NGC7099	325.0888	0.0746	-0.7017	-7.2218	-0.29	0.30	3554	-186.48	3.80
C2137-234	-23.1792	0.0040	0.0063	0.0055	-0.27	0.26	1.17	0.93	13

Table C.3. Globular clusters position and velocity from the Sun, not corrected for the Solar motion or the Local Standard of rest. Quoted values are medians, with errors which indicate uncertainties calculated from the 16th and 84th percentiles, and have been obtained from Monte Carlo sampling the (statistical and our best estimates of the systematic) errors in the observables. X is towards $l = 0$, Y is in the direction of Galactic rotation (towards $l = 90°$) and Z towards $b = 90$ (the Galactic north pole). U, V and W are the velocities in these directions.

Name	X [kpc]	Y [kpc]	Z [kpc]	U [km/s]	V [km/s]	W [km/s]
NGC0104	$1.87^{+0.04}_{-0.04}$	$-2.58^{+0.06}_{-0.06}$	$-3.18^{+0.07}_{-0.07}$	$-88.6^{+2.0}_{-2.0}$	$-80.1^{+2.1}_{-2.2}$	$38.5^{+0.8}_{-0.8}$
NGC0288	$-0.084^{+0.002}_{-0.002}$	$0.046^{+0.001}_{-0.001}$	$-8.89^{+0.21}_{-0.20}$	$-19.3^{+1.6}_{-1.5}$	$-297.3^{+7.0}_{-6.9}$	$44.0^{+0.2}_{-0.2}$
NGC0362	$3.11^{+0.07}_{-0.07}$	$-5.07^{+0.12}_{-0.11}$	$-6.21^{+0.15}_{-0.14}$	$-100.0^{+4.4}_{-4.4}$	$-344.8^{+5.1}_{-5.0}$	$-78.1^{+2.2}_{-2.2}$
NGC1851	$-4.26^{+0.10}_{-0.10}$	$-8.94^{+0.20}_{-0.20}$	$-6.95^{+0.16}_{-0.16}$	$-94.5^{+1.9}_{-2.0}$	$-319.5^{+2.4}_{-2.3}$	$-88.9^{+2.7}_{-2.8}$
NGC1904	$-7.63^{+0.17}_{-0.17}$	$-8.25^{+0.19}_{-0.19}$	$-6.32^{+0.14}_{-0.14}$	$-57.6^{+2.3}_{-2.3}$	$-266.4^{+3.5}_{-3.6}$	$-2.6^{+3.0}_{-3.0}$
NGC2298	$-4.29^{+0.10}_{-0.10}$	$-9.46^{+0.22}_{-0.22}$	$-2.98^{+0.07}_{-0.07}$	$80.5^{+3.7}_{-3.7}$	$-227.8^{+2.6}_{-2.7}$	$67.5^{+3.1}_{-3.1}$
NGC2808	$1.99^{+0.05}_{-0.05}$	$-9.20^{+0.21}_{-0.21}$	$-1.87^{+0.04}_{-0.04}$	$43.5^{+1.6}_{-1.7}$	$-101.0^{+0.8}_{-0.8}$	$21.7^{+1.9}_{-1.9}$
NGC3201	$0.61^{+0.01}_{-0.01}$	$-4.80^{+0.11}_{-0.11}$	$0.74^{+0.02}_{-0.02}$	$244.8^{+4.3}_{-4.3}$	$-450.6^{+0.8}_{-0.8}$	$143.5^{+1.8}_{-1.8}$
NGC4372	$2.94^{+0.07}_{-0.07}$	$-4.90^{+0.11}_{-0.11}$	$-1.00^{+0.02}_{-0.02}$	$-114.6^{+3.6}_{-3.7}$	$-166.6^{+2.7}_{-2.7}$	$59.7^{+1.9}_{-1.9}$
NGC4590	$4.12^{+0.10}_{-0.09}$	$-7.24^{+0.17}_{-0.17}$	$6.06^{+0.14}_{-0.14}$	$-182.5^{+3.7}_{-3.7}$	$38.2^{+1.4}_{-1.4}$	$8.6^{+2.0}_{-2.1}$
NGC4833	$3.62^{+0.08}_{-0.08}$	$-5.44^{+0.12}_{-0.12}$	$-0.92^{+0.02}_{-0.02}$	$-109.2^{+5.2}_{-5.1}$	$-307.1^{+3.4}_{-3.4}$	$-48.7^{+1.2}_{-1.2}$
NGC5024	$2.83^{+0.07}_{-0.07}$	$-1.45^{+0.03}_{-0.03}$	$17.61^{+0.41}_{-0.41}$	$44.2^{+3.1}_{-3.2}$	$-95.2^{+3.9}_{-3.7}$	$-78.9^{+0.7}_{-0.7}$
NGC5053	$3.04^{+0.07}_{-0.07}$	$-1.37^{+0.03}_{-0.03}$	$17.08^{+0.40}_{-0.39}$	$42.2^{+2.9}_{-3.1}$	$-104.7^{+3.8}_{-3.6}$	$28.9^{+0.8}_{-0.8}$
NGC5139	$3.17^{+0.07}_{-0.07}$	$-3.90^{+0.09}_{-0.09}$	$1.34^{+0.03}_{-0.03}$	$87.7^{+1.4}_{-1.4}$	$-268.7^{+2.3}_{-2.3}$	$-88.3^{+3.5}_{-3.5}$
NGC5272	$1.48^{+0.03}_{-0.03}$	$1.34^{+0.03}_{-0.03}$	$10.00^{+0.23}_{-0.23}$	$54.2^{+2.4}_{-2.5}$	$-121.5^{+2.9}_{-2.9}$	$-142.2^{+0.4}_{-0.4}$
NGC5286	$7.64^{+0.18}_{-0.18}$	$-8.60^{+0.20}_{-0.20}$	$2.15^{+0.05}_{-0.05}$	$44.9^{+1.8}_{-1.8}$	$-38.1^{+1.8}_{-1.7}$	$0.5^{+2.0}_{-1.9}$
NGC5466	$3.35^{+0.08}_{-0.08}$	$3.03^{+0.07}_{-0.07}$	$15.34^{+0.35}_{-0.35}$	$-230.9^{+6.4}_{-6.4}$	$-284.7^{+7.7}_{-7.3}$	$222.1^{+2.8}_{-2.8}$
NGC5634	$15.66^{+0.36}_{-0.36}$	$-5.02^{+0.12}_{-0.12}$	$19.09^{+0.44}_{-0.44}$	$-87.6^{+5.6}_{-5.5}$	$-259.3^{+7.8}_{-7.5}$	$-55.9^{+5.8}_{-5.8}$
NGC5897	$10.32^{+0.24}_{-0.24}$	$-3.17^{+0.07}_{-0.07}$	$6.31^{+0.14}_{-0.15}$	$-44.1^{+3.3}_{-3.3}$	$-383.0^{+8.6}_{-8.4}$	$81.1^{+2.0}_{-2.0}$
NGC5904	$5.12^{+0.12}_{-0.12}$	$0.345^{+0.008}_{-0.008}$	$5.47^{+0.13}_{-0.13}$	$290.4^{+6.1}_{-6.1}$	$-163.1^{+4.1}_{-4.1}$	$-188.8^{+5.4}_{-5.4}$
NGC5927	$6.40^{+0.15}_{-0.15}$	$-4.22^{+0.10}_{-0.10}$	$0.65^{+0.02}_{-0.01}$	$-210.2^{+3.0}_{-3.1}$	$-123.2^{+4.4}_{-4.4}$	$-2.7^{+1.3}_{-1.3}$
NGC5946	$8.92^{+0.20}_{-0.20}$	$-5.67^{+0.13}_{-0.13}$	$0.77^{+0.02}_{-0.02}$	$-36.6^{+3.7}_{-3.8}$	$-284.8^{+5.2}_{-5.1}$	$94.6^{+2.6}_{-2.7}$
NGC5986	$9.32^{+0.22}_{-0.21}$	$-3.95^{+0.09}_{-0.09}$	$2.39^{+0.06}_{-0.05}$	$-29.7^{+4.2}_{-4.2}$	$-316.8^{+6.9}_{-7.0}$	$-21.1^{+2.1}_{-2.1}$
NGC6093	$9.35^{+0.22}_{-0.22}$	$-1.20^{+0.03}_{-0.03}$	$3.33^{+0.08}_{-0.08}$	$-6.3^{+1.6}_{-1.6}$	$-290.3^{+7.0}_{-6.8}$	$-68.6^{+2.4}_{-2.3}$
NGC6121	$2.09^{+0.05}_{-0.05}$	$-0.332^{+0.007}_{-0.008}$	$0.61^{+0.01}_{-0.01}$	$40.4^{+0.7}_{-0.7}$	$-243.6^{+5.2}_{-5.5}$	$-15.9^{+0.9}_{-0.9}$
NGC6144	$8.48^{+0.19}_{-0.20}$	$-1.20^{+0.03}_{-0.03}$	$2.41^{+0.05}_{-0.06}$	$171.0^{+0.8}_{-0.8}$	$-158.1^{+3.4}_{-3.3}$	$34.8^{+1.6}_{-1.5}$
NGC6171	$5.88^{+0.13}_{-0.14}$	$0.347^{+0.008}_{-0.008}$	$2.50^{+0.06}_{-0.06}$	$3.7^{+0.9}_{-1.0}$	$-179.2^{+4.2}_{-4.2}$	$-71.2^{+1.7}_{-1.6}$
NGC6205	$2.76^{+0.06}_{-0.06}$	$4.60^{+0.11}_{-0.10}$	$4.65^{+0.11}_{-0.11}$	$-43.4^{+1.6}_{-1.6}$	$-263.1^{+2.6}_{-2.6}$	$-86.9^{+1.9}_{-1.9}$
NGC6218	$4.14^{+0.09}_{-0.10}$	$1.17^{+0.03}_{-0.03}$	$2.13^{+0.05}_{-0.05}$	$33.5^{+1.6}_{-1.7}$	$-128.6^{+2.8}_{-2.7}$	$-88.2^{+1.7}_{-1.8}$
NGC6235	$11.17^{+0.26}_{-0.26}$	$-0.211^{+0.005}_{-0.005}$	$2.69^{+0.06}_{-0.06}$	$94.4^{+3.3}_{-3.3}$	$-460.0^{+11.0}_{-10.8}$	$-55.2^{+2.8}_{-2.7}$
NGC6254	$3.91^{+0.09}_{-0.09}$	$1.06^{+0.02}_{-0.02}$	$1.73^{+0.04}_{-0.04}$	$106.2^{+1.2}_{-1.2}$	$-144.8^{+3.8}_{-3.8}$	$40.1^{+0.8}_{-0.8}$
NGC6266	$6.70^{+0.16}_{-0.15}$	$-0.76^{+0.02}_{-0.02}$	$0.87^{+0.02}_{-0.02}$	$-99.2^{+1.5}_{-1.6}$	$-170.5^{+4.3}_{-4.3}$	$68.8^{+2.1}_{-2.1}$
NGC6273	$8.67^{+0.20}_{-0.20}$	$-0.47^{+0.01}_{-0.01}$	$1.43^{+0.03}_{-0.03}$	$107.5^{+4.1}_{-4.0}$	$-32.4^{+1.6}_{-1.6}$	$167.9^{+3.8}_{-3.7}$
NGC6284	$15.07^{+0.35}_{-0.35}$	$-0.44^{+0.01}_{-0.01}$	$2.64^{+0.06}_{-0.06}$	$2.6^{+1.8}_{-1.8}$	$-256.7^{+6.4}_{-6.4}$	$102.1^{+3.4}_{-3.6}$
NGC6287	$9.23^{+0.21}_{-0.21}$	$0.021^{+0.000}_{-0.000}$	$1.80^{+0.04}_{-0.04}$	$-307.1^{+3.5}_{-3.5}$	$-197.5^{+4.9}_{-4.8}$	$69.0^{+3.4}_{-3.3}$
NGC6293	$9.40^{+0.22}_{-0.21}$	$-0.391^{+0.009}_{-0.009}$	$1.29^{+0.03}_{-0.03}$	$-130.9^{+1.8}_{-1.7}$	$-130.5^{+3.6}_{-3.5}$	$-161.8^{+3.7}_{-3.6}$
NGC6304	$5.86^{+0.14}_{-0.14}$	$-0.43^{+0.01}_{-0.01}$	$0.55^{+0.01}_{-0.01}$	$-119.8^{+3.6}_{-3.6}$	$-81.1^{+2.3}_{-2.4}$	$61.4^{+2.0}_{-2.0}$
NGC6316	$10.34^{+0.24}_{-0.24}$	$-0.51^{+0.01}_{-0.01}$	$1.04^{+0.02}_{-0.02}$	$48.7^{+8.8}_{-9.0}$	$-325.6^{+7.5}_{-7.8}$	$71.0^{+2.5}_{-2.5}$
NGC6325	$7.72^{+0.17}_{-0.18}$	$0.131^{+0.003}_{-0.003}$	$1.09^{+0.02}_{-0.02}$	$27.8^{+1.8}_{-1.8}$	$-449.5^{+10.3}_{-10.3}$	$70.9^{+2.1}_{-2.1}$
NGC6333	$7.73^{+0.18}_{-0.18}$	$0.75^{+0.02}_{-0.02}$	$1.47^{+0.03}_{-0.03}$	$237.7^{+6.8}_{-7.0}$	$-123.4^{+3.6}_{-3.6}$	$44.8^{+1.8}_{-1.9}$
NGC6341	$2.51^{+0.06}_{-0.06}$	$6.33^{+0.14}_{-0.14}$	$4.74^{+0.11}_{-0.11}$	$-36.7^{+1.4}_{-1.3}$	$-208.6^{+2.8}_{-2.8}$	$87.9^{+3.7}_{-3.7}$
NGC6342	$8.35^{+0.19}_{-0.19}$	$0.72^{+0.02}_{-0.02}$	$1.44^{+0.03}_{-0.03}$	$148.9^{+1.7}_{-1.6}$	$-289.3^{+7.0}_{-7.1}$	$-36.4^{+2.0}_{-1.9}$
NGC6352	$5.27^{+0.12}_{-0.12}$	$-1.77^{+0.04}_{-0.04}$	$-0.70^{+0.02}_{-0.02}$	$-172.2^{+1.4}_{-1.5}$	$-79.3^{+2.9}_{-3.0}$	$1.1^{+1.0}_{-1.0}$
NGC6356	$14.76^{+0.34}_{-0.34}$	$1.74^{+0.04}_{-0.04}$	$2.68^{+0.06}_{-0.06}$	$50.6^{+4.3}_{-4.3}$	$-345.8^{+8.6}_{-8.1}$	$97.9^{+3.3}_{-3.5}$
NGC6362	$5.98^{+0.14}_{-0.13}$	$-4.10^{+0.09}_{-0.10}$	$-2.29^{+0.05}_{-0.05}$	$-211.5^{+2.8}_{-2.8}$	$-151.9^{+5.1}_{-5.1}$	$124.7^{+2.4}_{-2.3}$
NGC6366	$3.19^{+0.07}_{-0.07}$	$1.06^{+0.02}_{-0.02}$	$0.97^{+0.02}_{-0.02}$	$22.1^{+1.0}_{-0.9}$	$-73.6^{+1.7}_{-1.7}$	$-39.4^{+1.0}_{-1.0}$
NGC6380	$10.72^{+0.25}_{-0.26}$	$-1.85^{+0.04}_{-0.04}$	$-0.65^{+0.02}_{-0.02}$	$-37.1^{+2.6}_{-2.6}$	$-193.9^{+5.0}_{-4.9}$	$2.5^{+2.1}_{-2.0}$
NGC6388	$9.52^{+0.22}_{-0.22}$	$-2.45^{+0.06}_{-0.06}$	$-1.16^{+0.03}_{-0.03}$	$40.2^{+1.2}_{-1.2}$	$-156.6^{+3.6}_{-3.5}$	$-22.8^{+1.7}_{-1.7}$
NGC6397	$2.09^{+0.05}_{-0.05}$	$-0.84^{+0.02}_{-0.02}$	$-0.48^{+0.01}_{-0.01}$	$-62.5^{+1.8}_{-1.9}$	$-134.7^{+3.0}_{-3.0}$	$-127.9^{+2.9}_{-2.9}$
NGC6401	$10.56^{+0.24}_{-0.24}$	$0.64^{+0.01}_{-0.01}$	$0.74^{+0.02}_{-0.02}$	$-74.9^{+8.3}_{-8.7}$	$-18.3^{+1.9}_{-1.9}$	$153.6^{+4.2}_{-4.2}$
NGC6402	$8.37^{+0.19}_{-0.19}$	$3.27^{+0.07}_{-0.08}$	$2.38^{+0.05}_{-0.05}$	$31.8^{+2.7}_{-2.8}$	$-279.0^{+6.1}_{-6.1}$	$13.0^{+1.7}_{-1.7}$
NGC6440	$8.41^{+0.19}_{-0.19}$	$1.14^{+0.03}_{-0.03}$	$0.56^{+0.01}_{-0.01}$	$-51.8^{+2.7}_{-2.8}$	$-167.9^{+4.0}_{-3.9}$	$-43.1^{+1.7}_{-1.7}$
NGC6441	$11.48^{+0.27}_{-0.26}$	$-1.30^{+0.03}_{-0.03}$	$-1.01^{+0.02}_{-0.02}$	$-22.3^{+1.4}_{-1.3}$	$-321.7^{+7.4}_{-7.7}$	$-28.9^{+2.1}_{-2.0}$

Continued on next page

Name	X [kpc]	Y [kpc]	Z [kpc]	U [km/s]	V [km/s]	W [km/s]
Fornax	$-33.1^{+2.6}_{-2.7}$	$-51.1^{+4.1}_{-4.2}$	$-134.5^{+10.8}_{-11.0}$	$34.2^{+22.5}_{-23.4}$	$-386.0^{+38.0}_{-36.9}$	$77.2^{+14.8}_{-14.3}$
Draco	$4.0^{+0.3}_{-0.3}$	$62.6^{+5.2}_{-4.5}$	$43.5^{+3.6}_{-3.1}$	$35.9^{+13.9}_{-14.8}$	$-247.6^{+7.1}_{-7.2}$	$-157.7^{+10.1}_{-10.2}$
Carina	$-16.7^{+0.9}_{-0.9}$	$-95.7^{+5.0}_{-5.3}$	$-39.7^{+2.1}_{-2.2}$	$-51.1^{+18.9}_{-18.1}$	$-298.4^{+9.8}_{-8.9}$	$151.4^{+21.1}_{-23.6}$
Ursa Minor	$-13.9^{+0.5}_{-0.6}$	$52.1^{+2.1}_{-2.0}$	$53.6^{+2.2}_{-2.0}$	$-12.8^{+12.2}_{-12.5}$	$-205.0^{+10.0}_{-10.3}$	$-153.7^{+9.7}_{-8.8}$
Sextans	$-28.4^{+1.4}_{-1.3}$	$-57.0^{+2.8}_{-2.5}$	$57.9^{+2.6}_{-2.8}$	$-253.0^{+17.8}_{-19.8}$	$-161.1^{+13.0}_{-11.0}$	$50.8^{+14.0}_{-12.9}$
Leo I	$-115.5^{+7.6}_{-7.2}$	$-119.6^{+7.9}_{-7.4}$	$192.0^{+11.9}_{-12.6}$	$-177.0^{+80.3}_{-75.9}$	$-243.0^{+61.0}_{-55.4}$	$113.2^{+44.8}_{-47.4}$
Leo II	$-69.0^{+3.9}_{-3.8}$	$-58.3^{+3.3}_{-3.2}$	$215.2^{+11.9}_{-12.3}$	$13.2^{+73.3}_{-69.1}$	$-253.9^{+73.8}_{-66.9}$	$18.9^{+27.5}_{-28.9}$
Sagittarius	$25.2^{+2.0}_{-1.8}$	$2.5^{+0.2}_{-0.2}$	$-6.4^{+0.5}_{-0.5}$	$221.3^{+7.2}_{-6.2}$	$-266.5^{+19.9}_{-22.5}$	$197.4^{+18.6}_{-17.1}$
Sculptor	$3.1^{+0.2}_{-0.2}$	$-9.8^{+0.7}_{-0.7}$	$-85.4^{+5.7}_{-6.1}$	$6.2^{+15.3}_{-14.1}$	$-74.0^{+15.6}_{-14.0}$	$-103.5^{+1.8}_{-1.8}$
Bootes I	$22.7^{+1.1}_{-1.0}$	$-0.76^{+0.03}_{-0.04}$	$61.0^{+2.8}_{-2.7}$	$124.9^{+14.1}_{-15.3}$	$-344.6^{+22.3}_{-21.6}$	$57.9^{+5.7}_{-5.1}$
LMC	$7.1^{+0.3}_{-0.3}$	$-41.0^{+2.0}_{-2.0}$	$-27.8^{+1.4}_{-1.4}$	$-68.6^{+10.2}_{-9.7}$	$-468.4^{+13.8}_{-13.5}$	$201.0^{+18.0}_{-18.8}$
SMC	$23.3^{+0.9}_{-0.9}$	$-38.1^{+1.5}_{-1.5}$	$-44.1^{+1.7}_{-1.7}$	$14.8^{+10.0}_{-10.0}$	$-425.0^{+16.0}_{-15.2}$	$167.5^{+13.0}_{-13.3}$

Table C.4. Dwarfs positions and velocities from the Sun, not corrected for the Solar motion or the Local Standard of rest. Quoted values are medians, with errors which indicate uncertainties calculated from the 16th and 84th percentiles, and have been obtained from Monte Carlo sampling the (statistical and our best estimates of the systematic) errors in the observables. The conventions are the same as for the globular clusters in Table C.3.

Table C.3 – continued from previous page

Name	X [kpc]	Y [kpc]	Z [kpc]	U [km/s]	V [km/s]	W [km/s]
NGC6453	$11.54^{+0.26}_{-0.27}$	$-0.86^{+0.02}_{-0.02}$	$-0.78^{+0.02}_{-0.02}$	$-115.1^{+8.2}_{-8.4}$	$-267.2^{+6.7}_{-6.6}$	$-160.9^{+4.4}_{-4.3}$
NGC6496	$10.89^{+0.25}_{-0.25}$	$-2.31^{+0.05}_{-0.05}$	$-1.97^{+0.05}_{-0.05}$	$-229.9^{+6.2}_{-6.2}$	$-473.4^{+11.5}_{-11.8}$	$-70.0^{+2.9}_{-2.9}$
NGC6517	$9.94^{+0.23}_{-0.23}$	$3.47^{+0.08}_{-0.08}$	$1.25^{+0.03}_{-0.03}$	$40.8^{+7.9}_{-7.7}$	$-223.3^{+5.8}_{-5.8}$	$-41.1^{+2.2}_{-2.3}$
NGC6522	$7.68^{+0.17}_{-0.18}$	$0.137^{+0.003}_{-0.003}$	$-0.53^{+0.01}_{-0.01}$	$-31.7^{+3.4}_{-3.4}$	$-156.7^{+3.9}_{-3.8}$	$-193.3^{+4.7}_{-4.6}$
NGC6528	$7.88^{+0.18}_{-0.18}$	$0.157^{+0.004}_{-0.004}$	$-0.58^{+0.01}_{-0.01}$	$208.3^{+1.4}_{-1.4}$	$-218.1^{+5.4}_{-5.3}$	$-44.7^{+1.6}_{-1.5}$
NGC6535	$5.95^{+0.14}_{-0.13}$	$3.06^{+0.07}_{-0.07}$	$1.23^{+0.03}_{-0.03}$	$-133.2^{+1.5}_{-1.5}$	$-233.8^{+3.3}_{-3.4}$	$35.9^{+2.1}_{-2.1}$
NGC6539	$7.24^{+0.17}_{-0.16}$	$2.75^{+0.06}_{-0.06}$	$0.92^{+0.02}_{-0.02}$	$94.2^{+2.2}_{-2.2}$	$-214.5^{+5.2}_{-5.3}$	$162.6^{+3.8}_{-3.8}$
NGC6541	$7.23^{+0.17}_{-0.17}$	$-1.37^{+0.03}_{-0.03}$	$-1.46^{+0.03}_{-0.03}$	$-232.4^{+2.9}_{-2.8}$	$-234.1^{+6.3}_{-6.2}$	$-116.6^{+3.7}_{-3.6}$
NGC6544	$2.98^{+0.07}_{-0.07}$	$0.305^{+0.007}_{-0.007}$	$-0.115^{+0.003}_{-0.003}$	$-5.8^{+3.8}_{-3.9}$	$-248.7^{+5.6}_{-5.6}$	$-98.1^{+2.3}_{-2.3}$
NGC6626	$5.42^{+0.12}_{-0.13}$	$0.74^{+0.02}_{-0.02}$	$-0.53^{+0.01}_{-0.01}$	$35.9^{+1.1}_{-1.1}$	$-205.8^{+5.0}_{-4.9}$	$-96.8^{+2.5}_{-2.4}$
NGC6637	$8.65^{+0.20}_{-0.20}$	$0.260^{+0.006}_{-0.006}$	$-1.57^{+0.04}_{-0.04}$	$63.8^{+2.8}_{-2.9}$	$-308.0^{+7.1}_{-7.3}$	$76.9^{+2.6}_{-2.5}$
NGC6656	$3.13^{+0.07}_{-0.07}$	$0.55^{+0.01}_{-0.01}$	$-0.421^{+0.010}_{-0.010}$	$-163.3^{+0.5}_{-0.5}$	$-38.2^{+0.6}_{-0.6}$	$-150.0^{+3.9}_{-4.0}$
NGC6681	$8.78^{+0.20}_{-0.20}$	$0.437^{+0.010}_{-0.010}$	$-1.95^{+0.04}_{-0.04}$	$193.1^{+1.1}_{-1.1}$	$-149.6^{+3.9}_{-4.0}$	$-181.3^{+3.5}_{-3.4}$
NGC6752	$3.31^{+0.08}_{-0.08}$	$-1.44^{+0.03}_{-0.03}$	$-1.73^{+0.04}_{-0.04}$	$-38.3^{+0.6}_{-0.5}$	$-77.3^{+2.1}_{-2.1}$	$52.7^{+1.1}_{-1.2}$
NGC6779	$4.27^{+0.10}_{-0.10}$	$8.26^{+0.20}_{-0.19}$	$1.36^{+0.03}_{-0.03}$	$-92.1^{+1.7}_{-1.6}$	$-121.9^{+1.1}_{-1.1}$	$92.2^{+3.0}_{-3.1}$
NGC6809	$4.90^{+0.11}_{-0.11}$	$0.76^{+0.02}_{-0.02}$	$-2.13^{+0.05}_{-0.05}$	$199.7^{+1.0}_{-1.0}$	$-224.6^{+5.8}_{-5.8}$	$-63.2^{+0.8}_{-0.8}$
NGC6838	$2.19^{+0.05}_{-0.05}$	$3.33^{+0.07}_{-0.08}$	$-0.318^{+0.007}_{-0.007}$	$52.4^{+1.6}_{-1.6}$	$-58.7^{+1.0}_{-1.0}$	$31.2^{+1.0}_{-1.0}$
NGC6864	$17.66^{+0.41}_{-0.40}$	$6.53^{+0.15}_{-0.15}$	$-9.08^{+0.21}_{-0.21}$	$-80.5^{+4.1}_{-4.0}$	$-326.9^{+7.2}_{-7.1}$	$44.0^{+3.7}_{-3.6}$
NGC6981	$11.69^{+0.27}_{-0.27}$	$8.24^{+0.19}_{-0.19}$	$-9.17^{+0.21}_{-0.21}$	$136.5^{+4.9}_{-4.8}$	$-251.9^{+6.2}_{-6.3}$	$-0.3^{+3.2}_{-3.2}$
NGC7078	$3.90^{+0.09}_{-0.09}$	$8.38^{+0.19}_{-0.19}$	$-4.77^{+0.11}_{-0.11}$	$89.9^{+3.3}_{-3.4}$	$-195.1^{+2.7}_{-2.7}$	$-35.6^{+2.5}_{-2.4}$
NGC7089	$5.57^{+0.13}_{-0.13}$	$7.49^{+0.17}_{-0.17}$	$-6.72^{+0.15}_{-0.16}$	$-86.3^{+2.8}_{-2.8}$	$-103.9^{+3.1}_{-3.0}$	$-178.2^{+4.7}_{-4.5}$
NGC7099	$4.93^{+0.11}_{-0.11}$	$2.53^{+0.06}_{-0.06}$	$-5.91^{+0.14}_{-0.13}$	$-18.3^{+2.4}_{-2.5}$	$-317.7^{+6.1}_{-6.0}$	$101.2^{+1.2}_{-1.2}$

Appendix D: On the orbital integrations

Figure D.1 compares the circular velocity curves for the three different Galactic potentials. It can be seen that the curves are quite similar between $\sim$ 3 and $\sim$ 40 kpc, but they differ substantially both in the inner as well as in the outer Galaxy. This will lead to some of the differences in the orbits as discussed in Sec. 6.

Figure D.2 shows some of these differences for the subset of globular clusters shown in Fig. 19. We plot here the orbits in cylindrical coordinates, and for a shorter period of time to show more clearly how the orbits diverge from eachother due to the differences in the gravitational potentials of the various models considered.

Figure D.3 shows the distribution of orbital parameters for the dSph in our sample, derived by drawing 1000 Monte Carlo realizations of the observables taking into account their uncertainties. The correlations seen are not all due to correlations in the errors themselves, but also reflect that orbital parameters are not really fully independent. It is important to bear this in mind when interpreting Figs. 20 and 22 where we have plotted uncorrelated error bars to make visual inspection easier.

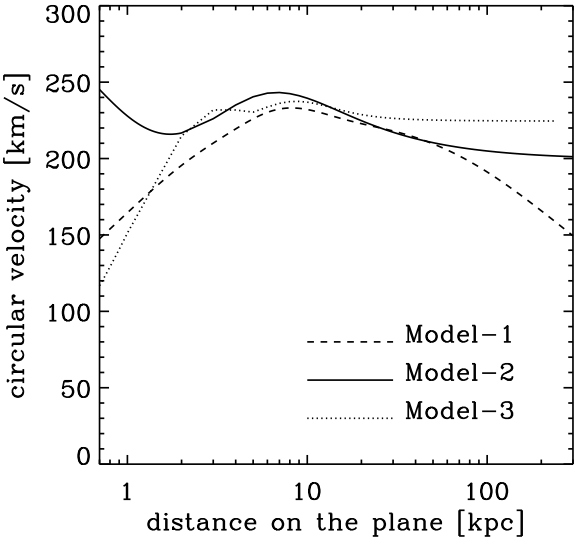


Fig. D.1. Circular velocity curves for the three Galactic potentials considered for the orbit integrations in Sec. 6.

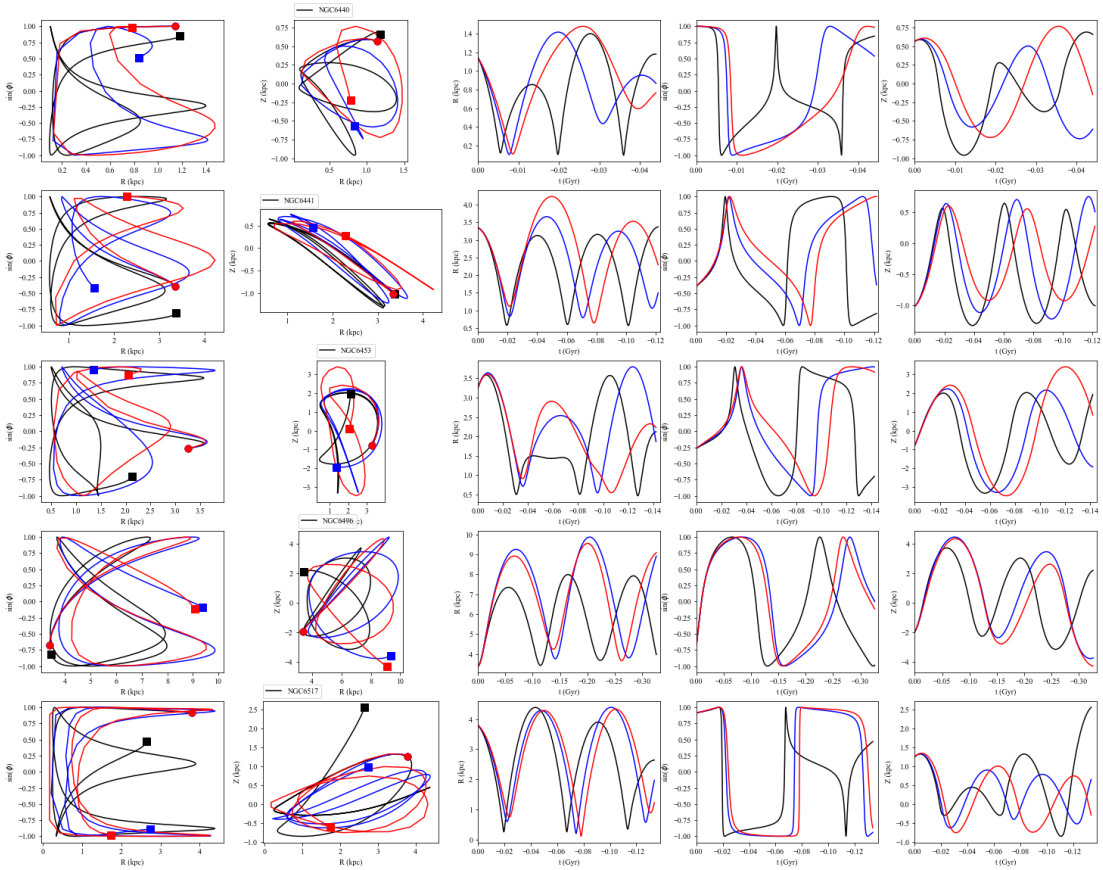


Fig. D.2. Orbits of the globular clusters shown in Fig. 19, now plotted in cylindrical coordinates and as a function of time (right panels) for shorter integration times (approximately 3 radial oscillations). The different colours correspond to the axisymmetric potentials Models 1 (blue) and 2 (black), and to the barred Model-3 (red). The solid circles in the leftmost panels denote the present-day positions, while the squares are the positions for each of the models at the end of the chosen integration time.

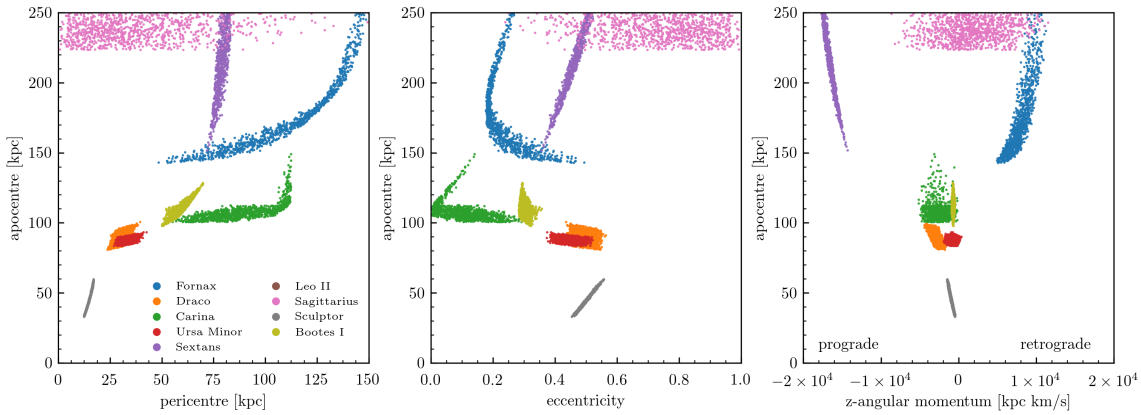


Fig. D.3. Distribution of orbital parameters for the dwarfs (in different colours) showing the results obtained from the different Monte Carlo realizations (only for those within the 1σ uncertainties on the observables), computed using the potential of Model-1.

Table D.1. Globular clusters orbital properties. We list here the median apocentre, pericentre, eccentricity, inclination of the orbital plane θ, and radial period T_r. The median and errors (defined by the 16th and 84th percentiles), have been obtained from Monte Carlo realizations sampling the errors in the observables using the full covariance matrix. For each globular cluster we quote values derived from orbits integrated for 10 Gyr in the three Galactic potentials in Sec. 6: Models 1, 2 and 3 in the first, second and third rows, respectively.

Name	apocentre [kpc]	pericentre [kpc]	eccentr.	L_z [km/s kpc]	inclin. θ [deg]	T_r [Myr]
NGC0104	$7.52^{+0.01}_{-0.01}$	$5.74^{+0.02}_{-0.02}$	$0.13^{+0.01}_{-0.01}$	$-1247.5^{+10.7}_{-11.2}$	$151.6^{+0.6}_{-0.6}$	$126.9^{+0.1}_{-0.1}$
	$7.68^{+0.01}_{-0.01}$	$5.68^{+0.03}_{-0.03}$	$0.15^{+0.01}_{-0.01}$	$-1335.8^{+10.6}_{-12.2}$	$147.6^{+0.6}_{-0.6}$	$123.5^{+0.1}_{-0.1}$
	$7.64^{+0.02}_{-0.02}$	$5.13^{+0.02}_{-0.02}$	$0.18^{+0.01}_{-0.01}$	$-1231.7^{+6.5}_{-8.8}$	$148.6^{+0.7}_{-0.8}$	$122.0^{+1.5}_{-1.9}$
NGC0288	$12.24^{+0.15}_{-0.16}$	$2.43^{+0.22}_{-0.24}$	$0.67^{+0.02}_{-0.02}$	$436.0^{+52.5}_{-60.3}$	$57.5^{+1.7}_{-1.1}$	$151.1^{+3.2}_{-3.4}$
	$12.35^{+0.15}_{-0.14}$	$1.95^{+0.23}_{-0.21}$	$0.73^{+0.02}_{-0.02}$	$371.4^{+58.8}_{-55.9}$	$64.7^{+1.6}_{-1.4}$	$144.5^{+3.0}_{-3.0}$
	$12.93^{+0.64}_{-0.42}$	$0.36^{+0.21}_{-0.21}$	$0.89^{+0.01}_{-0.02}$	$85.3^{+65.4}_{-56.6}$	$77.2^{+8.3}_{-6.7}$	$139.2^{+3.6}_{-2.8}$
NGC0362	$11.96^{+0.31}_{-0.27}$	$0.98^{+0.01}_{-0.03}$	$0.85^{+0.01}_{-0.01}$	$56.6^{+13.3}_{-13.4}$	$80.1^{+3.6}_{-5.3}$	$138.9^{+3.5}_{-3.6}$
	$11.78^{+0.21}_{-0.26}$	$0.67^{+0.06}_{-0.13}$	$0.90^{+0.02}_{-0.01}$	$29.3^{+11.8}_{-14.5}$	$80.6^{+5.2}_{-4.4}$	$129.5^{+3.0}_{-3.0}$
	$11.91^{+0.29}_{-0.13}$	$0.08^{+0.05}_{-0.03}$	$0.92^{+0.03}_{-0.02}$	$45.5^{+20.4}_{-15.2}$	$80.5^{+3.3}_{-3.0}$	$127.8^{+3.1}_{-3.9}$
NGC1851	$20.37^{+0.22}_{-0.29}$	$0.98^{+0.10}_{-0.07}$	$0.91^{+0.01}_{-0.01}$	$181.0^{+16.9}_{-20.1}$	$69.8^{+3.3}_{-3.3}$	$230.9^{+3.3}_{-3.3}$
	$20.23^{+0.26}_{-0.41}$	$0.69^{+0.11}_{-0.07}$	$0.94^{+0.01}_{-0.01}$	$82.4^{+19.0}_{-17.9}$	$71.2^{+4.1}_{-4.1}$	$224.5^{+3.5}_{-3.0}$
	$20.28^{+0.63}_{-0.18}$	$0.43^{+0.19}_{-0.15}$	$0.84^{+0.01}_{-0.01}$	$94.9^{+17.7}_{-22.4}$	$78.6^{+3.4}_{-3.4}$	$227.3^{+4.0}_{-4.1}$
NGC1904	$19.41^{+0.22}_{-0.27}$	$0.63^{+0.14}_{-0.02}$	$0.94^{+0.01}_{-0.01}$	$-48.7^{+59.0}_{-55.0}$	$96.8^{+9.1}_{-8.1}$	$217.3^{+4.1}_{-3.2}$
	$19.48^{+0.18}_{-0.22}$	$0.62^{+0.09}_{-0.09}$	$0.94^{+0.01}_{-0.01}$	$-192.4^{+56.5}_{-48.9}$	$128.1^{+8.0}_{-11.4}$	$214.0^{+3.5}_{-2.5}$
	$19.88^{+1.45}_{-0.69}$	$0.73^{+0.08}_{-0.11}$	$0.92^{+0.01}_{-0.01}$	$-355.9^{+55.1}_{-37.9}$	$134.6^{+4.4}_{-6.1}$	$208.5^{+4.7}_{-4.0}$
NGC2298	$17.71^{+0.38}_{-0.36}$	$2.08^{+0.24}_{-0.23}$	$0.79^{+0.02}_{-0.02}$	$647.0^{+79.9}_{-82.5}$	$55.2^{+2.1}_{-1.8}$	$207.0^{+5.9}_{-5.5}$
	$17.82^{+0.35}_{-0.30}$	$1.68^{+0.19}_{-0.16}$	$0.83^{+0.01}_{-0.01}$	$530.2^{+73.0}_{-67.9}$	$51.3^{+2.0}_{-1.5}$	$203.0^{+5.5}_{-4.5}$
	$17.78^{+0.93}_{-0.44}$	$0.79^{+0.13}_{-0.15}$	$0.88^{+0.02}_{-0.02}$	$360.0^{+44.6}_{-52.1}$	$49.5^{+4.6}_{-4.2}$	$190.7^{+2.5}_{-7.6}$
NGC2808	$14.14^{+0.23}_{-0.22}$	$1.05^{+0.04}_{-0.03}$	$0.86^{+0.01}_{-0.01}$	$-394.3^{+22.8}_{-23.5}$	$168.8^{+0.7}_{-0.9}$	$157.9^{+2.4}_{-2.2}$
	$14.29^{+0.23}_{-0.24}$	$1.18^{+0.04}_{-0.05}$	$0.85^{+0.01}_{-0.01}$	$-478.7^{+23.9}_{-25.6}$	$142.8^{+1.5}_{-1.0}$	$157.0^{+2.5}_{-2.5}$
	$13.90^{+0.78}_{-0.28}$	$0.64^{+0.05}_{-0.04}$	$0.88^{+0.01}_{-0.01}$	$-343.1^{+18.0}_{-19.9}$	$147.3^{+3.1}_{-4.3}$	$148.9^{+3.6}_{-3.7}$
NGC3201	$29.25^{+1.04}_{-1.06}$	$8.60^{+0.02}_{-0.07}$	$0.55^{+0.01}_{-0.01}$	$2793.7^{+37.7}_{-40.8}$	$27.5^{+0.1}_{-0.1}$	$388.8^{+11.8}_{-12.5}$
	$26.82^{+0.97}_{-0.95}$	$8.53^{+0.06}_{-0.07}$	$0.52^{+0.01}_{-0.01}$	$2762.7^{+37.1}_{-39.6}$	$27.6^{+0.1}_{-0.1}$	$365.0^{+12.0}_{-11.5}$
	$22.25^{+0.69}_{-0.64}$	$8.53^{+0.07}_{-0.07}$	$0.45^{+0.01}_{-0.01}$	$2707.1^{+37.1}_{-35.7}$	$24.4^{+0.1}_{-0.0}$	$307.1^{+6.8}_{-6.8}$
NGC4372	$7.30^{+0.03}_{-0.03}$	$3.15^{+0.10}_{-0.08}$	$0.40^{+0.01}_{-0.01}$	$-922.3^{+13.0}_{-13.1}$	$150.6^{+0.6}_{-0.5}$	$100.4^{+1.0}_{-1.1}$
	$7.40^{+0.03}_{-0.03}$	$3.14^{+0.08}_{-0.09}$	$0.40^{+0.01}_{-0.01}$	$-984.4^{+12.3}_{-13.5}$	$154.5^{+0.8}_{-0.5}$	$97.0^{+0.1}_{-1.0}$
	$7.33^{+0.11}_{-0.19}$	$1.46^{+0.86}_{-0.10}$	$0.48^{+0.01}_{-0.01}$	$-718.6^{+87.5}_{-58.8}$	$151.3^{+2.9}_{-3.7}$	$90.9^{+1.1}_{-1.4}$
NGC4590	$28.76^{+0.76}_{-0.79}$	$9.13^{+0.13}_{-0.13}$	$0.52^{+0.01}_{-0.01}$	$-2402.1^{+22.2}_{-22.8}$	$139.1^{+0.6}_{-0.5}$	$388.8^{+9.8}_{-10.0}$
	$29.57^{+0.92}_{-0.82}$	$9.10^{+0.13}_{-0.11}$	$0.53^{+0.01}_{-0.01}$	$-2492.4^{+20.7}_{-24.4}$	$138.5^{+0.5}_{-0.5}$	$403.0^{+12.0}_{-10.5}$
	$23.13^{+0.57}_{-0.49}$	$8.28^{+0.12}_{-0.10}$	$0.47^{+0.01}_{-0.01}$	$-2156.2^{+15.8}_{-15.5}$	$137.2^{+0.5}_{-0.6}$	$316.5^{+5.7}_{-7.7}$
NGC4833	$7.93^{+0.15}_{-0.16}$	$0.92^{+0.05}_{-0.08}$	$0.79^{+0.01}_{-0.01}$	$-249.8^{+30.9}_{-31.4}$	$141.8^{+3.4}_{-3.9}$	$90.7^{+1.9}_{-1.9}$
	$7.86^{+0.15}_{-0.12}$	$0.93^{+0.02}_{-0.09}$	$0.79^{+0.01}_{-0.01}$	$-282.2^{+26.2}_{-30.0}$	$133.2^{+3.4}_{-1.6}$	$86.0^{+1.5}_{-1.5}$
	$7.86^{+0.18}_{-0.07}$	$0.24^{+0.07}_{-0.08}$	$0.88^{+0.01}_{-0.01}$	$-151.4^{+25.9}_{-28.6}$	$127.4^{+4.2}_{-3.8}$	$83.8^{+3.0}_{-2.0}$
NGC5024	$21.73^{+0.39}_{-0.39}$	$8.58^{+0.02}_{-0.02}$	$0.43^{+0.01}_{-0.01}$	$-727.5^{+26.1}_{-25.0}$	$105.6^{+0.7}_{-0.7}$	$307.3^{+4.3}_{-4.3}$
	$21.95^{+0.39}_{-0.38}$	$9.05^{+0.04}_{-0.04}$	$0.42^{+0.01}_{-0.01}$	$-805.9^{+25.2}_{-26.2}$	$105.5^{+0.6}_{-0.6}$	$316.5^{+5.0}_{-5.0}$
	$21.29^{+0.44}_{-0.42}$	$8.59^{+0.05}_{-0.04}$	$0.42^{+0.01}_{-0.01}$	$-751.0^{+23.4}_{-25.5}$	$105.0^{+0.7}_{-0.6}$	$298.1^{+5.8}_{-6.1}$
NGC5053	$17.89^{+0.34}_{-0.39}$	$9.98^{+0.05}_{-0.05}$	$0.28^{+0.01}_{-0.01}$	$-652.1^{+23.5}_{-27.1}$	$103.7^{+0.7}_{-0.6}$	$279.3^{+3.6}_{-3.8}$
	$17.80^{+0.39}_{-0.33}$	$10.53^{+0.06}_{-0.06}$	$0.26^{+0.01}_{-0.01}$	$-729.1^{+27.5}_{-24.1}$	$103.7^{+0.6}_{-0.6}$	$285.0^{+4.5}_{-3.5}$
	$17.96^{+0.45}_{-0.42}$	$9.75^{+0.06}_{-0.05}$	$0.29^{+0.01}_{-0.01}$	$-677.5^{+20.9}_{-21.7}$	$103.3^{+0.6}_{-0.5}$	$272.3^{+3.9}_{-3.7}$
NGC5139	$7.12^{+0.02}_{-0.02}$	$1.60^{+0.01}_{-0.01}$	$0.63^{+0.01}_{-0.01}$	$502.8^{+12.6}_{-13.2}$	$41.4^{+0.8}_{-0.9}$	$86.7^{+0.6}_{-0.5}$
	$7.26^{+0.03}_{-0.04}$	$1.29^{+0.01}_{-0.02}$	$0.70^{+0.01}_{-0.01}$	$461.6^{+13.7}_{-14.4}$	$35.3^{+2.0}_{-1.3}$	$82.5^{+0.1}_{-0.5}$
	$7.03^{+0.13}_{-0.05}$	$1.48^{+0.03}_{-0.08}$	$0.62^{+0.01}_{-0.01}$	$519.0^{+27.3}_{-26.9}$	$26.4^{+0.9}_{-1.8}$	$81.8^{+1.8}_{-2.1}$
NGC5272	$16.03^{+0.26}_{-0.24}$	$5.29^{+0.05}_{-0.06}$	$0.50^{+0.01}_{-0.01}$	$-921.7^{+16.9}_{-15.6}$	$122.6^{+0.5}_{-0.5}$	$215.4^{+2.3}_{-2.1}$
	$16.00^{+0.24}_{-0.25}$	$5.48^{+0.05}_{-0.05}$	$0.49^{+0.01}_{-0.01}$	$-1003.6^{+15.8}_{-17.1}$	$119.9^{+0.5}_{-0.4}$	$214.5^{+2.0}_{-2.5}$
	$16.40^{+0.18}_{-0.98}$	$5.27^{+0.03}_{-0.05}$	$0.48^{+0.01}_{-0.01}$	$-963.3^{+13.0}_{-11.7}$	$120.2^{+0.2}_{-0.5}$	$204.0^{+4.5}_{-5.0}$
NGC5286	$13.67^{+0.34}_{-0.30}$	$1.15^{+0.10}_{-0.09}$	$0.85^{+0.01}_{-0.01}$	$362.3^{+52.2}_{-49.9}$	$55.4^{+3.4}_{-3.1}$	$155.3^{+4.3}_{-3.6}$
	$13.69^{+0.31}_{-0.34}$	$1.04^{+0.09}_{-0.07}$	$0.86^{+0.01}_{-0.01}$	$317.2^{+51.1}_{-50.0}$	$53.4^{+2.7}_{-2.7}$	$151.5^{+4.0}_{-4.0}$
	$13.81^{+0.25}_{-0.54}$	$0.96^{+0.20}_{-0.12}$	$0.83^{+0.01}_{-0.01}$	$401.7^{+58.3}_{-46.5}$	$46.0^{+3.6}_{-4.0}$	$145.9^{+4.2}_{-4.0}$
NGC5466	$48.10^{+3.80}_{-2.80}$	$6.17^{+0.58}_{-0.46}$	$0.77^{+0.01}_{-0.01}$	$854.1^{+67.6}_{-58.6}$	$71.8^{+0.2}_{-0.1}$	$590.1^{+51.1}_{-37.1}$

Continued on next page

Table D.1 – continued from previous page

Name	apocentre [kpc]	pericentre [kpc]	eccentr.	L_z [km/s kpc]	inclin. θ [deg]	T_r [Myr]
	$48.16^{+3.71}_{-3.04}$	$6.04^{+0.55}_{-0.51}$	$0.78^{+0.01}_{-0.01}$	$822.5^{+67.4}_{-64.8}$	$72.8^{+0.0}_{-0.0}$	$596.0^{+47.5}_{-40.0}$
	$33.96^{+1.31}_{-1.47}$	$4.24^{+0.45}_{-0.43}$	$0.78^{+0.01}_{-0.01}$	$526.8^{+60.8}_{-50.8}$	$74.4^{+0.6}_{-0.2}$	$393.5^{+22.9}_{-18.0}$
NGC5634	$22.41^{+0.52}_{-0.78}$	$3.14^{+0.66}_{-0.19}$	$0.75^{+0.02}_{-0.04}$	$-489.0^{+66.1}_{-74.8}$	$112.0^{+1.2}_{-1.4}$	$267.7^{+10.6}_{-7.7}$
	$22.09^{+0.65}_{-0.63}$	$3.19^{+0.27}_{-0.22}$	$0.75^{+0.01}_{-0.01}$	$-424.0^{+60.7}_{-70.2}$	$106.9^{+1.5}_{-1.6}$	$265.0^{+10.0}_{-8.5}$
	$22.41^{+1.56}_{-0.34}$	$1.58^{+0.06}_{-0.14}$	$0.80^{+0.01}_{-0.01}$	$-145.0^{+20.5}_{-48.0}$	$98.1^{+3.3}_{-1.2}$	$256.2^{+5.4}_{-4.9}$
NGC5897	$9.11^{+0.41}_{-0.40}$	$2.82^{+0.28}_{-0.30}$	$0.53^{+0.02}_{-0.02}$	$-395.5^{+60.8}_{-60.2}$	$119.2^{+1.0}_{-1.2}$	$120.9^{+6.5}_{-6.5}$
	$8.64^{+0.38}_{-0.35}$	$2.32^{+0.31}_{-0.25}$	$0.58^{+0.03}_{-0.03}$	$-347.4^{+53.4}_{-63.7}$	$112.3^{+1.5}_{-1.5}$	$107.0^{+6.5}_{-5.5}$
	$8.82^{+1.48}_{-0.46}$	$0.98^{+0.30}_{-0.58}$	$0.74^{+0.03}_{-0.03}$	$-243.3^{+88.0}_{-75.9}$	$113.6^{+5.2}_{-4.2}$	$105.2^{+4.5}_{-5.8}$
NGC5904	$25.35^{+1.48}_{-1.58}$	$2.69^{+0.11}_{-0.08}$	$0.81^{+0.01}_{-0.01}$	$-358.5^{+15.0}_{-18.3}$	$106.6^{+1.7}_{-1.4}$	$298.8^{+17.5}_{-18.5}$
	$23.66^{+1.50}_{-1.39}$	$2.69^{+0.06}_{-0.04}$	$0.80^{+0.01}_{-0.01}$	$-401.4^{+17.5}_{-19.0}$	$108.2^{+1.3}_{-1.4}$	$279.5^{+18.5}_{-16.0}$
	$16.06^{+1.16}_{-0.39}$	$2.76^{+0.09}_{-0.11}$	$0.66^{+0.01}_{-0.01}$	$-365.7^{+25.7}_{-42.0}$	$106.7^{+3.1}_{-1.3}$	$191.0^{+10.4}_{-7.0}$
NGC5927	$5.42^{+0.10}_{-0.09}$	$4.34^{+0.02}_{-0.01}$	$0.11^{+0.01}_{-0.01}$	$-1061.8^{+6.8}_{-8.0}$	$171.6^{+0.2}_{-0.2}$	$90.0^{+0.8}_{-0.7}$
	$5.19^{+0.09}_{-0.07}$	$4.31^{+0.04}_{-0.03}$	$0.09^{+0.01}_{-0.01}$	$-1102.7^{+5.0}_{-5.5}$	$167.2^{+0.2}_{-0.2}$	$84.0^{+0.5}_{-0.5}$
	$5.75^{+0.08}_{-0.06}$	$2.97^{+0.06}_{-0.10}$	$0.22^{+0.01}_{-0.01}$	$-892.5^{+7.6}_{-7.8}$	$166.6^{+0.3}_{-0.3}$	$84.8^{+1.8}_{-2.9}$
NGC5946	$5.93^{+0.17}_{-0.16}$	$0.85^{+0.11}_{-0.13}$	$0.75^{+0.03}_{-0.02}$	$-173.5^{+32.7}_{-36.4}$	$107.4^{+2.5}_{-2.5}$	$71.6^{+2.6}_{-2.4}$
	$5.72^{+0.19}_{-0.20}$	$0.76^{+0.09}_{-0.01}$	$0.77^{+0.02}_{-0.02}$	$-163.6^{+33.1}_{-30.3}$	$119.5^{+1.9}_{-2.3}$	$65.5^{+2.0}_{-3.0}$
	$6.41^{+0.23}_{-0.12}$	$0.07^{+0.03}_{-0.02}$	$0.73^{+0.01}_{-0.01}$	$-38.2^{+21.5}_{-25.7}$	$100.7^{+6.4}_{-6.2}$	$68.8^{+3.1}_{-2.7}$
NGC5986	$4.92^{+0.14}_{-0.16}$	$0.85^{+0.14}_{-0.10}$	$0.70^{+0.02}_{-0.03}$	$-152.2^{+32.4}_{-38.4}$	$124.1^{+3.3}_{-3.8}$	$61.7^{+2.4}_{-2.1}$
	$4.95^{+0.10}_{-0.16}$	$0.52^{+0.16}_{-0.08}$	$0.81^{+0.03}_{-0.05}$	$-133.1^{+34.1}_{-32.4}$	$124.3^{+4.1}_{-2.3}$	$55.5^{+2.0}_{-2.0}$
	$5.24^{+0.28}_{-0.24}$	$0.07^{+0.03}_{-0.02}$	$0.87^{+0.01}_{-0.01}$	$-24.0^{+53.3}_{-45.6}$	$96.6^{+10.6}_{-15.0}$	$56.6^{+2.0}_{-2.1}$
NGC6093	$3.72^{+0.13}_{-0.13}$	$1.10^{+0.14}_{-0.12}$	$0.54^{+0.03}_{-0.03}$	$-45.5^{+15.9}_{-18.6}$	$100.7^{+2.6}_{-2.6}$	$51.8^{+2.4}_{-2.3}$
	$3.89^{+0.09}_{-0.07}$	$0.60^{+0.14}_{-0.23}$	$0.74^{+0.09}_{-0.05}$	$-28.5^{+13.3}_{-15.9}$	$97.8^{+2.0}_{-1.3}$	$45.5^{+2.5}_{-1.5}$
	$4.41^{+0.16}_{-0.19}$	$0.10^{+0.04}_{-0.04}$	$0.93^{+0.01}_{-0.02}$	$7.9^{+35.8}_{-50.0}$	$88.5^{+9.9}_{-8.0}$	$50.1^{+1.0}_{-1.9}$
NGC6121	$6.00^{+0.12}_{-0.13}$	$0.39^{+0.09}_{-0.09}$	$0.88^{+0.03}_{-0.03}$	$5.0^{+33.7}_{-33.1}$	$77.2^{+70.3}_{-42.7}$	$69.2^{+0.6}_{-0.5}$
	$6.08^{+0.01}_{-0.11}$	$0.41^{+0.05}_{-0.04}$	$0.88^{+0.01}_{-0.01}$	$-49.4^{+31.9}_{-36.1}$	$110.8^{+9.1}_{-10.5}$	$65.5^{+1.0}_{-0.5}$
	$6.15^{+0.09}_{-0.06}$	$0.10^{+0.09}_{-0.05}$	$0.83^{+0.01}_{-0.02}$	$-77.5^{+48.6}_{-40.3}$	$118.9^{+13.6}_{-19.7}$	$68.7^{+2.2}_{-1.1}$
NGC6144	$3.57^{+0.04}_{-0.02}$	$2.30^{+0.09}_{-0.12}$	$0.22^{+0.02}_{-0.01}$	$243.6^{+21.1}_{-20.4}$	$64.0^{+1.9}_{-1.9}$	$57.5^{+1.2}_{-0.6}$
	$2.96^{+0.05}_{-0.02}$	$2.39^{+0.07}_{-0.09}$	$0.11^{+0.02}_{-0.01}$	$228.5^{+21.0}_{-23.7}$	$68.2^{+1.8}_{-1.5}$	$36.0^{+1.0}_{-0.5}$
	$4.14^{+0.07}_{-0.04}$	$1.97^{+0.12}_{-0.11}$	$0.18^{+0.02}_{-0.01}$	$273.8^{+25.7}_{-20.1}$	$62.8^{+1.4}_{-1.6}$	$55.6^{+2.1}_{-1.9}$
NGC6171	$3.52^{+0.03}_{-0.05}$	$1.16^{+0.06}_{-0.03}$	$0.50^{+0.01}_{-0.01}$	$-160.1^{+17.3}_{-18.4}$	$126.2^{+1.9}_{-2.0}$	$50.2^{+0.6}_{-0.8}$
	$3.74^{+0.03}_{-0.02}$	$0.94^{+0.06}_{-0.07}$	$0.60^{+0.02}_{-0.02}$	$-195.0^{+19.2}_{-19.5}$	$121.8^{+1.5}_{-1.6}$	$47.0^{+1.0}_{-0.5}$
	$3.86^{+0.16}_{-0.16}$	$1.03^{+0.10}_{-0.38}$	$0.45^{+0.01}_{-0.01}$	$-189.0^{+67.0}_{-50.8}$	$117.5^{+5.1}_{-8.3}$	$46.1^{+2.2}_{-0.7}$
NGC6205	$8.61^{+0.09}_{-0.08}$	$1.71^{+0.01}_{-0.01}$	$0.67^{+0.01}_{-0.01}$	$245.3^{+9.8}_{-9.9}$	$69.3^{+1.3}_{-1.4}$	$107.2^{+0.7}_{-0.8}$
	$8.63^{+0.09}_{-0.07}$	$1.53^{+0.02}_{-0.02}$	$0.70^{+0.01}_{-0.01}$	$199.4^{+10.5}_{-10.1}$	$72.1^{+1.1}_{-1.2}$	$101.5^{+0.5}_{-0.5}$
	$9.08^{+0.08}_{-0.37}$	$1.49^{+0.01}_{-0.03}$	$0.66^{+0.01}_{-0.01}$	$208.8^{+24.8}_{-15.5}$	$73.0^{+1.3}_{-2.6}$	$105.2^{+0.9}_{-4.7}$
NGC6218	$4.88^{+0.04}_{-0.04}$	$2.44^{+0.05}_{-0.05}$	$0.33^{+0.01}_{-0.01}$	$-526.3^{+19.5}_{-19.4}$	$141.7^{+1.0}_{-1.0}$	$73.0^{+0.8}_{-0.7}$
	$5.00^{+0.04}_{-0.04}$	$2.41^{+0.06}_{-0.05}$	$0.35^{+0.01}_{-0.01}$	$-586.1^{+21.1}_{-19.8}$	$138.1^{+1.0}_{-1.1}$	$69.5^{+0.5}_{-1.0}$
	$4.92^{+0.10}_{-0.11}$	$1.84^{+0.04}_{-0.06}$	$0.30^{+0.01}_{-0.01}$	$-508.3^{+26.8}_{-16.7}$	$138.2^{+1.7}_{-1.3}$	$70.6^{+1.2}_{-5.6}$
NGC6235	$6.19^{+0.68}_{-0.65}$	$3.35^{+0.28}_{-0.26}$	$0.30^{+0.02}_{-0.02}$	$-613.0^{+85.2}_{-91.1}$	$130.2^{+2.0}_{-2.2}$	$94.1^{+9.0}_{-8.6}$
	$5.04^{+0.55}_{-0.50}$	$3.15^{+0.27}_{-0.26}$	$0.23^{+0.01}_{-0.01}$	$-549.0^{+80.0}_{-85.4}$	$125.9^{+2.2}_{-2.4}$	$76.5^{+7.5}_{-6.5}$
	$5.79^{+0.09}_{-1.12}$	$2.12^{+0.05}_{-0.13}$	$0.28^{+0.02}_{-0.01}$	$-511.5^{+129.6}_{-11.2}$	$127.9^{+0.5}_{-4.5}$	$66.7^{+5.1}_{-5.3}$
NGC6254	$5.17^{+0.07}_{-0.07}$	$2.33^{+0.05}_{-0.05}$	$0.38^{+0.01}_{-0.01}$	$-556.8^{+20.0}_{-19.4}$	$142.7^{+1.1}_{-1.1}$	$74.4^{+1.0}_{-1.0}$
	$5.28^{+0.08}_{-0.07}$	$2.30^{+0.06}_{-0.06}$	$0.39^{+0.01}_{-0.01}$	$-614.6^{+21.8}_{-24.1}$	$142.1^{+1.2}_{-1.1}$	$71.0^{+0.1}_{-1.0}$
	$4.94^{+0.26}_{-0.11}$	$1.97^{+0.02}_{-0.05}$	$0.27^{+0.01}_{-0.01}$	$-544.5^{+8.1}_{-25.2}$	$141.1^{+2.2}_{-1.0}$	$73.7^{+3.4}_{-2.2}$
NGC6266	$2.11^{+0.13}_{-0.13}$	$0.91^{+0.01}_{-0.02}$	$0.40^{+0.02}_{-0.02}$	$-180.2^{+16.3}_{-15.3}$	$144.5^{+1.6}_{-2.0}$	$33.4^{+1.4}_{-1.4}$
	$2.36^{+0.10}_{-0.01}$	$0.69^{+0.07}_{-0.07}$	$0.55^{+0.02}_{-0.02}$	$-209.3^{+16.9}_{-18.5}$	$145.9^{+0.4}_{-0.2}$	$31.0^{+1.5}_{-1.5}$
	$2.28^{+0.27}_{-0.08}$	$0.55^{+0.12}_{-0.25}$	$0.31^{+0.01}_{-0.01}$	$-195.6^{+18.2}_{-18.2}$	$138.2^{+6.1}_{-2.5}$	$42.9^{+1.8}_{-20.1}$
NGC6273	$4.51^{+0.21}_{-0.18}$	$1.34^{+0.14}_{-0.16}$	$0.54^{+0.03}_{-0.02}$	$155.8^{+41.0}_{-43.5}$	$68.7^{+5.5}_{-4.8}$	$61.7^{+3.1}_{-3.0}$
	$3.38^{+0.20}_{-0.16}$	$1.32^{+0.09}_{-0.07}$	$0.44^{+0.01}_{-0.01}$	$115.4^{+44.1}_{-47.5}$	$75.3^{+5.6}_{-4.5}$	$47.0^{+2.5}_{-2.5}$
	$4.78^{+0.43}_{-0.23}$	$0.85^{+0.14}_{-0.17}$	$0.51^{+0.01}_{-0.01}$	$211.5^{+32.1}_{-39.9}$	$60.3^{+4.2}_{-3.2}$	$58.6^{+4.4}_{-4.2}$
NGC6284	$7.63^{+0.33}_{-0.36}$	$1.09^{+0.22}_{-0.11}$	$0.75^{+0.01}_{-0.03}$	$-68.0^{+39.4}_{-46.4}$	$95.5^{+3.1}_{-3.0}$	$92.9^{+5.1}_{-4.5}$
	$7.31^{+0.32}_{-0.39}$	$1.07^{+0.12}_{-0.10}$	$0.75^{+0.01}_{-0.01}$	$-12.0^{+40.6}_{-36.6}$	$91.6^{+4.1}_{-5.8}$	$84.5^{+4.5}_{-4.5}$
	$8.21^{+0.38}_{-0.57}$	$0.65^{+0.05}_{-0.11}$	$0.60^{+0.01}_{-0.01}$	$164.5^{+42.3}_{-50.0}$	$67.4^{+6.3}_{-6.4}$	$91.8^{+5.9}_{-5.4}$
NGC6287	$6.23^{+0.38}_{-0.36}$	$1.04^{+0.02}_{-0.04}$	$0.72^{+0.01}_{-0.01}$	$54.8^{+4.8}_{-7.5}$	$84.9^{+0.4}_{-0.2}$	$77.6^{+4.1}_{-4.0}$

Continued on next page

Table D.1 – continued from previous page

Name	apocentre [kpc]	pericentre [kpc]	eccentr.	L_z [km/s kpc]	inclin. θ [deg]	T_r [Myr]
	$4.74^{+0.33}_{-0.27}$	$1.24^{+0.05}_{-0.05}$	$0.59^{+0.01}_{-0.01}$	$52.5^{+8.0}_{-8.4}$	$83.6^{+0.8}_{-0.6}$	$59.5^{+3.5}_{-3.0}$
	$7.13^{+0.65}_{-0.40}$	$0.23^{+0.29}_{-0.14}$	$0.72^{+0.02}_{-0.01}$	$16.2^{+40.9}_{-50.7}$	$86.5^{+7.4}_{-5.6}$	$76.7^{+4.9}_{-3.3}$
NGC6293	$3.23^{+0.31}_{-0.16}$	$0.80^{+0.01}_{-0.03}$	$0.61^{+0.02}_{-0.02}$	$90.4^{+19.1}_{-19.2}$	$46.0^{+5.9}_{-1.7}$	$44.4^{+3.3}_{-2.2}$
	$2.81^{+0.47}_{-0.23}$	$0.47^{+0.11}_{-0.07}$	$0.71^{+0.07}_{-0.06}$	$76.6^{+23.6}_{-22.9}$	$64.5^{+5.0}_{-11.0}$	$34.5^{+4.0}_{-3.0}$
	$3.80^{+0.48}_{-0.29}$	$0.40^{+0.09}_{-0.26}$	$0.47^{+0.02}_{-0.02}$	$134.8^{+35.1}_{-50.1}$	$60.6^{+9.9}_{-3.5}$	$49.6^{+2.7}_{-2.4}$
NGC6304	$3.14^{+0.16}_{-0.17}$	$1.79^{+0.08}_{-0.08}$	$0.27^{+0.01}_{-0.01}$	$-433.0^{+26.3}_{-27.1}$	$160.1^{+0.8}_{-0.9}$	$49.7^{+2.1}_{-2.1}$
	$3.13^{+0.20}_{-0.20}$	$1.87^{+0.05}_{-0.04}$	$0.26^{+0.02}_{-0.04}$	$-485.0^{+25.0}_{-27.8}$	$155.5^{+1.5}_{-2.1}$	$48.0^{+1.5}_{-2.5}$
	$3.18^{+0.14}_{-0.09}$	$0.46^{+0.26}_{-0.22}$	$0.21^{+0.01}_{-0.01}$	$-314.2^{+74.0}_{-51.0}$	$152.8^{+4.1}_{-6.8}$	$46.0^{+2.9}_{-3.4}$
NGC6316	$2.96^{+0.25}_{-0.23}$	$0.63^{+0.13}_{-0.13}$	$0.65^{+0.04}_{-0.04}$	$-139.9^{+33.1}_{-36.4}$	$141.2^{+1.5}_{-1.7}$	$39.1^{+3.2}_{-2.7}$
	$2.59^{+0.22}_{-0.26}$	$0.42^{+0.11}_{-0.08}$	$0.72^{+0.03}_{-0.03}$	$-107.0^{+28.6}_{-32.0}$	$128.3^{+3.5}_{-3.4}$	$30.0^{+3.5}_{-3.0}$
	$3.30^{+0.39}_{-0.31}$	$0.12^{+0.10}_{-0.07}$	$0.60^{+0.02}_{-0.02}$	$-110.7^{+46.7}_{-39.0}$	$124.7^{+11.3}_{-12.7}$	$40.5^{+3.1}_{-3.4}$
NGC6325	$2.18^{+0.17}_{-0.16}$	$0.84^{+0.17}_{-0.13}$	$0.44^{+0.09}_{-0.11}$	$93.8^{+30.2}_{-35.7}$	$69.1^{+8.2}_{-7.1}$	$33.9^{+0.8}_{-0.5}$
	$1.35^{+0.03}_{-0.00}$	$1.15^{+0.04}_{-0.02}$	$0.08^{+0.02}_{-0.01}$	$126.7^{+26.8}_{-28.9}$	$64.2^{+6.0}_{-5.3}$	$16.5^{+0.1}_{-0.5}$
	$1.81^{+0.33}_{-0.17}$	$0.30^{+0.22}_{-0.24}$	$0.22^{+0.04}_{-0.04}$	$59.0^{+26.1}_{-38.3}$	$66.1^{+14.3}_{-9.7}$	$25.2^{+1.4}_{-1.3}$
NGC6333	$4.40^{+0.23}_{-0.22}$	$1.33^{+0.03}_{-0.03}$	$0.54^{+0.02}_{-0.02}$	$-244.8^{+17.5}_{-18.9}$	$120.6^{+1.7}_{-1.7}$	$60.0^{+2.3}_{-2.1}$
	$3.52^{+0.19}_{-0.18}$	$1.45^{+0.02}_{-0.03}$	$0.42^{+0.02}_{-0.02}$	$-272.4^{+20.7}_{-22.8}$	$123.8^{+2.3}_{-2.2}$	$49.0^{+1.5}_{-1.5}$
	$5.11^{+0.21}_{-0.23}$	$0.71^{+0.09}_{-0.14}$	$0.50^{+0.02}_{-0.02}$	$-240.0^{+36.5}_{-31.5}$	$124.8^{+3.0}_{-3.2}$	$62.6^{+2.7}_{-4.2}$
NGC6341	$10.53^{+0.15}_{-0.13}$	$1.02^{+0.01}_{-0.02}$	$0.82^{+0.01}_{-0.01}$	$-47.1^{+21.7}_{-20.7}$	$94.5^{+2.4}_{-2.2}$	$124.0^{+1.9}_{-1.9}$
	$10.61^{+0.13}_{-0.13}$	$0.98^{+0.03}_{-0.00}$	$0.83^{+0.01}_{-0.01}$	$-103.5^{+21.9}_{-21.8}$	$104.6^{+3.4}_{-3.5}$	$119.0^{+2.0}_{-1.5}$
	$10.62^{+0.41}_{-0.36}$	$0.18^{+0.10}_{-0.08}$	$0.76^{+0.01}_{-0.01}$	$-86.3^{+37.3}_{-32.5}$	$107.4^{+5.2}_{-6.8}$	$114.6^{+1.9}_{-3.2}$
NGC6342	$1.84^{+0.06}_{-0.04}$	$1.31^{+0.08}_{-0.07}$	$0.17^{+0.02}_{-0.01}$	$-120.6^{+11.3}_{-13.6}$	$116.9^{+1.2}_{-0.9}$	$23.7^{+0.8}_{-0.6}$
	$1.66^{+0.00}_{-0.00}$	$0.97^{+0.11}_{-0.09}$	$0.27^{+0.05}_{-0.05}$	$-112.4^{+8.5}_{-9.9}$	$112.7^{+0.8}_{-0.6}$	$27.0^{+0.1}_{-1.0}$
	$2.40^{+0.53}_{-0.19}$	$0.91^{+0.17}_{-0.76}$	$0.23^{+0.04}_{-0.20}$	$-145.7^{+6.0}_{-12.5}$	$119.2^{+2.9}_{-1.0}$	$30.2^{+2.2}_{-3.6}$
NGC6352	$4.44^{+0.14}_{-0.14}$	$3.15^{+0.04}_{-0.03}$	$0.17^{+0.01}_{-0.01}$	$-774.8^{+19.4}_{-20.6}$	$167.6^{+0.4}_{-0.4}$	$72.1^{+1.5}_{-1.4}$
	$4.36^{+0.15}_{-0.13}$	$3.20^{+0.04}_{-0.03}$	$0.15^{+0.01}_{-0.01}$	$-832.1^{+19.8}_{-21.7}$	$163.1^{+0.6}_{-0.5}$	$67.5^{+1.5}_{-1.0}$
	$5.71^{+0.04}_{-0.72}$	$3.06^{+0.03}_{-0.07}$	$0.12^{+0.01}_{-0.01}$	$-936.6^{+103.7}_{-5.6}$	$164.7^{+0.2}_{-0.8}$	$69.9^{+2.3}_{-3.9}$
NGC6356	$7.86^{+0.39}_{-0.38}$	$3.25^{+0.39}_{-0.37}$	$0.41^{+0.03}_{-0.03}$	$-770.8^{+85.7}_{-90.9}$	$138.0^{+1.0}_{-1.1}$	$109.2^{+7.2}_{-6.8}$
	$7.55^{+0.40}_{-0.34}$	$2.64^{+0.35}_{-0.30}$	$0.48^{+0.03}_{-0.03}$	$-688.7^{+76.6}_{-91.9}$	$134.9^{+1.2}_{-1.1}$	$96.5^{+7.0}_{-5.5}$
	$9.31^{+0.29}_{-1.17}$	$1.48^{+0.17}_{-0.24}$	$0.57^{+0.02}_{-0.02}$	$-527.7^{+129.8}_{-56.6}$	$138.4^{+2.6}_{-6.5}$	$97.8^{+4.9}_{-6.0}$
NGC6362	$7.43^{+0.16}_{-0.16}$	$5.06^{+0.01}_{-0.01}$	$0.19^{+0.01}_{-0.01}$	$-1030.3^{+5.5}_{-6.2}$	$141.4^{+0.3}_{-0.3}$	$120.8^{+1.8}_{-1.7}$
	$6.83^{+0.15}_{-0.13}$	$5.12^{+0.01}_{-0.00}$	$0.14^{+0.01}_{-0.01}$	$-1069.7^{+4.1}_{-4.9}$	$138.8^{+0.4}_{-0.3}$	$111.0^{+1.5}_{-1.5}$
	$7.13^{+0.17}_{-0.13}$	$4.21^{+0.03}_{-0.02}$	$0.21^{+0.01}_{-0.01}$	$-981.9^{+3.7}_{-4.0}$	$142.4^{+0.3}_{-0.2}$	$108.1^{+2.8}_{-1.4}$
NGC6366	$5.21^{+0.07}_{-0.06}$	$3.58^{+0.08}_{-0.07}$	$0.19^{+0.01}_{-0.01}$	$-897.4^{+18.8}_{-21.4}$	$165.2^{+0.5}_{-0.5}$	$82.7^{+1.2}_{-1.0}$
	$5.38^{+0.07}_{-0.06}$	$3.56^{+0.07}_{-0.07}$	$0.20^{+0.01}_{-0.01}$	$-973.7^{+19.7}_{-20.3}$	$161.2^{+0.6}_{-0.6}$	$80.0^{+1.0}_{-0.1}$
	$6.18^{+0.05}_{-0.12}$	$2.57^{+0.09}_{-0.04}$	$0.18^{+0.01}_{-0.01}$	$-864.4^{+52.0}_{-39.6}$	$162.5^{+1.8}_{-1.2}$	$77.0^{+2.4}_{-3.3}$
NGC6380	$3.12^{+0.22}_{-0.18}$	$0.53^{+0.01}_{-0.01}$	$0.71^{+0.01}_{-0.01}$	$80.2^{+4.2}_{-4.5}$	$12.1^{+1.4}_{-0.7}$	$39.8^{+2.3}_{-1.9}$
	$2.90^{+0.21}_{-0.22}$	$0.39^{+0.05}_{-0.03}$	$0.76^{+0.01}_{-0.02}$	$90.1^{+4.4}_{-5.4}$	$55.8^{+3.1}_{-2.7}$	$34.0^{+2.0}_{-2.0}$
	$4.13^{+0.24}_{-0.31}$	$0.27^{+0.15}_{-0.06}$	$0.67^{+0.01}_{-0.01}$	$120.8^{+11.4}_{-14.4}$	$49.6^{+2.3}_{-2.4}$	$43.5^{+4.7}_{-2.1}$
NGC6388	$3.23^{+0.12}_{-0.09}$	$0.95^{+0.08}_{-0.06}$	$0.54^{+0.02}_{-0.01}$	$241.2^{+16.5}_{-16.4}$	$31.3^{+1.9}_{-1.8}$	$44.2^{+1.5}_{-1.2}$
	$3.18^{+0.10}_{-0.10}$	$0.74^{+0.07}_{-0.10}$	$0.62^{+0.04}_{-0.02}$	$235.5^{+16.7}_{-20.5}$	$36.5^{+0.6}_{-2.5}$	$39.5^{+1.5}_{-1.0}$
	$5.46^{+1.17}_{-1.17}$	$0.20^{+0.35}_{-0.11}$	$0.37^{+0.01}_{-0.01}$	$216.9^{+69.2}_{-66.3}$	$43.2^{+18.8}_{-12.8}$	$48.6^{+3.5}_{-1.6}$
NGC6397	$6.45^{+0.02}_{-0.02}$	$2.86^{+0.05}_{-0.05}$	$0.39^{+0.01}_{-0.01}$	$-719.9^{+20.1}_{-20.5}$	$134.6^{+1.2}_{-1.2}$	$91.0^{+0.5}_{-0.5}$
	$6.59^{+0.03}_{-0.02}$	$2.90^{+0.05}_{-0.05}$	$0.39^{+0.01}_{-0.01}$	$-795.8^{+23.1}_{-22.2}$	$143.5^{+1.2}_{-1.2}$	$88.0^{+0.5}_{-0.5}$
	$7.20^{+0.11}_{-0.57}$	$1.72^{+0.92}_{-0.10}$	$0.34^{+0.01}_{-0.01}$	$-767.0^{+92.2}_{-61.2}$	$150.8^{+2.8}_{-3.8}$	$82.0^{+3.4}_{-3.1}$
NGC6401	$4.58^{+0.35}_{-0.35}$	$2.63^{+0.23}_{-0.25}$	$0.27^{+0.01}_{-0.01}$	$573.6^{+52.8}_{-56.4}$	$36.8^{+0.5}_{-0.4}$	$71.4^{+5.1}_{-5.4}$
	$3.90^{+0.35}_{-0.33}$	$2.40^{+0.26}_{-0.25}$	$0.24^{+0.01}_{-0.01}$	$546.2^{+58.8}_{-58.2}$	$39.1^{+0.3}_{-0.2}$	$59.0^{+5.5}_{-4.5}$
	$4.47^{+0.26}_{-0.26}$	$2.64^{+0.27}_{-0.30}$	$0.24^{+0.02}_{-0.02}$	$605.6^{+56.5}_{-63.0}$	$35.0^{+1.4}_{-1.0}$	$72.8^{+5.5}_{-4.9}$
NGC6402	$4.09^{+0.10}_{-0.09}$	$0.88^{+0.09}_{-0.08}$	$0.65^{+0.02}_{-0.02}$	$-147.1^{+18.9}_{-19.6}$	$129.7^{+0.8}_{-0.9}$	$53.6^{+1.6}_{-1.5}$
	$4.32^{+0.13}_{-0.12}$	$0.51^{+0.05}_{-0.04}$	$0.79^{+0.01}_{-0.02}$	$-139.4^{+13.2}_{-16.3}$	$130.3^{+3.6}_{-3.1}$	$49.0^{+1.5}_{-1.5}$
	$4.35^{+0.31}_{-0.24}$	$0.09^{+0.12}_{-0.04}$	$0.68^{+0.01}_{-0.01}$	$-65.4^{+42.0}_{-50.8}$	$110.9^{+9.1}_{-12.9}$	$51.8^{+1.4}_{-2.7}$
NGC6440	$1.34^{+0.05}_{-0.02}$	$0.41^{+0.05}_{-0.05}$	$0.53^{+0.04}_{-0.03}$	$61.7^{+14.3}_{-15.9}$	$54.4^{+7.8}_{-6.0}$	$22.0^{+0.9}_{-0.6}$
	$1.30^{+0.04}_{-0.05}$	$0.23^{+0.06}_{-0.04}$	$0.69^{+0.06}_{-0.06}$	$47.1^{+15.8}_{-20.0}$	$57.6^{+13.4}_{-4.2}$	$15.0^{+1.0}_{-0.1}$
	$1.55^{+0.09}_{-0.09}$	$0.34^{+0.14}_{-0.23}$	$0.42^{+0.09}_{-0.07}$	$70.3^{+20.1}_{-22.7}$	$58.5^{+8.0}_{-5.1}$	$31.2^{+1.5}_{-1.5}$
NGC6441	$3.64^{+0.22}_{-0.25}$	$1.12^{+0.16}_{-0.15}$	$0.53^{+0.03}_{-0.03}$	$-266.9^{+46.7}_{-47.2}$	$160.1^{+0.9}_{-1.1}$	$48.2^{+3.3}_{-3.5}$

Continued on next page

Table D.1 – continued from previous page

Name	apocentre [kpc]	pericentre [kpc]	eccentr.	L_z [km/s kpc]	inclin. θ [deg]	T_r [Myr]
	$3.43^{+0.26}_{-0.25}$	$0.80^{+0.14}_{-0.12}$	$0.62^{+0.03}_{-0.03}$	$-222.0^{+39.8}_{-45.8}$	$137.6^{+2.8}_{-2.9}$	$41.0^{+4.0}_{-3.0}$
	$4.19^{+0.24}_{-0.13}$	$0.35^{+0.14}_{-0.19}$	$0.65^{+0.01}_{-0.01}$	$-152.7^{+36.0}_{-32.0}$	$134.3^{+3.8}_{-4.9}$	$51.2^{+2.5}_{-3.4}$
NGC6453	$4.00^{+0.33}_{-0.33}$	$1.32^{+0.21}_{-0.18}$	$0.50^{+0.02}_{-0.03}$	$-163.4^{+28.7}_{-32.8}$	$105.1^{+1.4}_{-1.4}$	$56.4^{+5.0}_{-4.7}$
	$3.62^{+0.32}_{-0.32}$	$1.22^{+0.14}_{-0.12}$	$0.50^{+0.01}_{-0.01}$	$-131.8^{+25.8}_{-27.3}$	$107.5^{+1.7}_{-2.0}$	$48.5^{+4.0}_{-4.5}$
	$4.43^{+0.28}_{-0.32}$	$0.10^{+0.11}_{-0.04}$	$0.56^{+0.02}_{-0.02}$	$17.3^{+52.1}_{-47.8}$	$86.1^{+9.8}_{-9.4}$	$55.9^{+3.2}_{-4.3}$
NGC6496	$10.17^{+1.53}_{-1.18}$	$3.96^{+0.26}_{-0.23}$	$0.44^{+0.03}_{-0.03}$	$-1109.9^{+100.2}_{-119.7}$	$148.9^{+0.8}_{-0.8}$	$137.7^{+18.8}_{-14.0}$
	$8.11^{+1.10}_{-0.97}$	$3.79^{+0.25}_{-0.21}$	$0.36^{+0.03}_{-0.03}$	$-1043.0^{+101.5}_{-107.5}$	$144.9^{+1.0}_{-1.0}$	$111.0^{+13.5}_{-12.0}$
	$6.39^{+0.46}_{-0.60}$	$3.74^{+0.29}_{-1.07}$	$0.21^{+0.02}_{-0.02}$	$-903.4^{+182.7}_{-94.5}$	$145.8^{+1.2}_{-3.0}$	$91.2^{+8.4}_{-5.0}$
NGC6517	$4.16^{+0.16}_{-0.16}$	$0.68^{+0.06}_{-0.05}$	$0.72^{+0.01}_{-0.02}$	$-143.4^{+26.5}_{-25.4}$	$127.0^{+3.4}_{-4.3}$	$51.5^{+1.9}_{-1.9}$
	$4.04^{+0.19}_{-0.20}$	$0.49^{+0.05}_{-0.05}$	$0.79^{+0.02}_{-0.02}$	$-134.0^{+24.2}_{-23.5}$	$130.8^{+4.6}_{-5.0}$	$46.0^{+2.0}_{-2.0}$
	$4.56^{+0.31}_{-0.28}$	$0.05^{+0.04}_{-0.02}$	$0.93^{+0.01}_{-0.02}$	$-22.0^{+39.8}_{-37.5}$	$98.9^{+11.9}_{-16.2}$	$51.6^{+2.9}_{-2.3}$
NGC6522	$1.25^{+0.08}_{-0.04}$	$0.55^{+0.10}_{-0.08}$	$0.39^{+0.05}_{-0.05}$	$-42.7^{+15.9}_{-19.5}$	$116.0^{+1.6}_{-1.4}$	$21.0^{+1.6}_{-1.1}$
	$1.23^{+0.11}_{-0.21}$	$0.31^{+0.11}_{-0.07}$	$0.58^{+0.05}_{-0.07}$	$-68.4^{+20.5}_{-19.5}$	$121.9^{+1.3}_{-7.7}$	$15.0^{+2.5}_{-2.5}$
	$1.40^{+0.04}_{-0.07}$	$0.04^{+0.02}_{-0.02}$	$0.59^{+0.15}_{-0.14}$	$-6.7^{+21.7}_{-16.7}$	$94.3^{+7.9}_{-14.5}$	$20.6^{+1.3}_{-1.2}$
NGC6528	$1.65^{+0.13}_{-0.07}$	$0.36^{+0.00}_{-0.00}$	$0.64^{+0.03}_{-0.01}$	$-43.7^{+4.8}_{-6.5}$	$107.4^{+1.9}_{-1.4}$	$25.0^{+1.3}_{-0.7}$
	$1.03^{+0.31}_{-0.24}$	$0.39^{+0.08}_{-0.11}$	$0.45^{+0.20}_{-0.19}$	$-53.3^{+7.3}_{-8.5}$	$110.9^{+10.8}_{-3.6}$	$14.0^{+2.5}_{-2.0}$
	$2.43^{+0.14}_{-0.11}$	$0.05^{+0.03}_{-0.02}$	$0.53^{+0.04}_{-0.02}$	$-72.6^{+25.5}_{-23.8}$	$123.7^{+9.0}_{-12.9}$	$33.6^{+1.0}_{-1.1}$
NGC6535	$4.42^{+0.05}_{-0.04}$	$1.36^{+0.06}_{-0.06}$	$0.53^{+0.02}_{-0.02}$	$347.6^{+13.3}_{-14.3}$	$20.4^{+1.1}_{-1.1}$	$57.6^{+0.1}_{-0.1}$
	$4.52^{+0.05}_{-0.04}$	$1.10^{+0.04}_{-0.06}$	$0.61^{+0.02}_{-0.02}$	$323.6^{+14.7}_{-16.4}$	$38.8^{+1.2}_{-1.1}$	$53.5^{+0.5}_{-0.1}$
	$4.80^{+0.06}_{-0.06}$	$1.08^{+0.06}_{-0.07}$	$0.56^{+0.03}_{-0.03}$	$370.0^{+12.8}_{-12.6}$	$26.5^{+0.9}_{-1.0}$	$57.3^{+1.1}_{-1.6}$
NGC6539	$3.28^{+0.05}_{-0.03}$	$2.15^{+0.07}_{-0.06}$	$0.21^{+0.01}_{-0.01}$	$-320.4^{+5.2}_{-5.0}$	$122.0^{+0.6}_{-0.6}$	$54.8^{+0.7}_{-0.6}$
	$3.29^{+0.02}_{-0.02}$	$1.95^{+0.05}_{-0.04}$	$0.26^{+0.01}_{-0.01}$	$-335.3^{+5.0}_{-5.7}$	$125.4^{+0.9}_{-0.8}$	$50.5^{+0.1}_{-0.5}$
	$3.61^{+0.60}_{-0.16}$	$1.36^{+0.14}_{-0.12}$	$0.23^{+0.01}_{-0.01}$	$-294.9^{+39.2}_{-47.6}$	$126.8^{+4.2}_{-3.3}$	$48.8^{+2.3}_{-1.9}$
NGC6541	$4.08^{+0.05}_{-0.05}$	$1.58^{+0.06}_{-0.05}$	$0.44^{+0.01}_{-0.01}$	$-314.6^{+3.7}_{-4.1}$	$139.2^{+2.0}_{-1.9}$	$58.5^{+0.8}_{-0.6}$
	$3.70^{+0.07}_{-0.05}$	$1.44^{+0.07}_{-0.05}$	$0.44^{+0.02}_{-0.02}$	$-326.8^{+3.5}_{-4.0}$	$130.8^{+1.1}_{-1.1}$	$50.5^{+0.5}_{-0.5}$
	$4.28^{+0.04}_{-0.05}$	$1.52^{+0.13}_{-0.22}$	$0.38^{+0.01}_{-0.02}$	$-389.3^{+34.6}_{-8.7}$	$135.1^{+1.0}_{-1.8}$	$58.8^{+2.2}_{-1.7}$
NGC6544	$5.22^{+0.12}_{-0.14}$	$0.38^{+0.09}_{-0.08}$	$0.86^{+0.03}_{-0.03}$	$16.7^{+27.0}_{-29.2}$	$88.0^{+3.5}_{-3.2}$	$61.5^{+0.6}_{-0.6}$
	$5.23^{+0.09}_{-0.12}$	$0.39^{+0.05}_{-0.03}$	$0.86^{+0.01}_{-0.01}$	$-29.8^{+32.7}_{-34.5}$	$105.8^{+8.3}_{-18.6}$	$57.5^{+0.1}_{-1.0}$
	$5.57^{+0.14}_{-0.15}$	$0.43^{+0.06}_{-0.06}$	$0.80^{+0.02}_{-0.02}$	$-185.7^{+30.6}_{-43.7}$	$133.3^{+3.2}_{-2.7}$	$60.9^{+3.8}_{-2.1}$
NGC6626	$2.88^{+0.12}_{-0.10}$	$0.70^{+0.04}_{-0.04}$	$0.61^{+0.01}_{-0.01}$	$-144.0^{+16.6}_{-19.2}$	$117.3^{+2.7}_{-2.5}$	$39.7^{+1.5}_{-1.3}$
	$3.15^{+0.09}_{-0.16}$	$0.58^{+0.12}_{-0.06}$	$0.69^{+0.03}_{-0.06}$	$-178.3^{+20.0}_{-19.8}$	$136.7^{+5.1}_{-3.5}$	$38.5^{+1.0}_{-2.0}$
	$3.17^{+0.16}_{-0.46}$	$0.11^{+0.16}_{-0.07}$	$0.42^{+0.01}_{-0.01}$	$-160.0^{+88.1}_{-79.8}$	$132.8^{+13.2}_{-20.8}$	$40.3^{+1.5}_{-1.8}$
NGC6637	$1.68^{+0.09}_{-0.06}$	$1.03^{+0.12}_{-0.09}$	$0.24^{+0.03}_{-0.03}$	$-45.9^{+13.4}_{-19.9}$	$105.1^{+3.2}_{-2.8}$	$22.6^{+1.1}_{-0.8}$
	$1.93^{+0.12}_{-0.01}$	$0.32^{+0.04}_{-0.03}$	$0.72^{+0.03}_{-0.03}$	$-33.8^{+11.8}_{-13.3}$	$109.5^{+4.2}_{-5.1}$	$23.5^{+1.5}_{-1.5}$
	$2.14^{+0.28}_{-0.20}$	$0.45^{+0.16}_{-0.40}$	$0.44^{+0.02}_{-0.03}$	$-42.5^{+20.4}_{-17.0}$	$102.3^{+3.9}_{-6.0}$	$30.3^{+1.4}_{-2.1}$
NGC6656	$10.06^{+0.01}_{-0.01}$	$3.12^{+0.04}_{-0.04}$	$0.53^{+0.01}_{-0.01}$	$-970.8^{+18.3}_{-17.5}$	$145.7^{+0.8}_{-0.8}$	$129.2^{+0.2}_{-0.2}$
	$9.92^{+0.02}_{-0.02}$	$3.21^{+0.04}_{-0.04}$	$0.51^{+0.01}_{-0.01}$	$-1055.2^{+19.2}_{-19.6}$	$149.7^{+0.8}_{-0.9}$	$124.0^{+0.5}_{-0.5}$
	$8.60^{+0.15}_{-0.10}$	$2.71^{+0.04}_{-0.06}$	$0.48^{+0.01}_{-0.01}$	$-895.9^{+11.3}_{-19.2}$	$154.6^{+1.1}_{-0.7}$	$105.7^{+2.1}_{-2.6}$
NGC6681	$5.41^{+0.30}_{-0.26}$	$0.92^{+0.10}_{-0.06}$	$0.71^{+0.03}_{-0.04}$	$-33.9^{+14.0}_{-16.8}$	$96.1^{+2.2}_{-2.1}$	$68.6^{+2.7}_{-2.1}$
	$4.31^{+0.26}_{-0.23}$	$1.16^{+0.10}_{-0.09}$	$0.58^{+0.05}_{-0.05}$	$-49.5^{+16.7}_{-19.2}$	$96.5^{+2.1}_{-1.9}$	$54.5^{+2.0}_{-1.5}$
	$5.97^{+0.29}_{-0.19}$	$0.07^{+0.03}_{-0.02}$	$0.72^{+0.04}_{-0.03}$	$-9.1^{+20.3}_{-18.9}$	$92.2^{+5.0}_{-5.4}$	$65.8^{+3.2}_{-3.3}$
NGC6752	$5.58^{+0.04}_{-0.04}$	$3.66^{+0.08}_{-0.08}$	$0.21^{+0.01}_{-0.01}$	$-863.3^{+20.9}_{-20.2}$	$155.3^{+0.6}_{-0.6}$	$88.4^{+0.9}_{-0.9}$
	$5.72^{+0.04}_{-0.05}$	$3.64^{+0.08}_{-0.08}$	$0.22^{+0.01}_{-0.01}$	$-939.8^{+22.6}_{-22.3}$	$151.0^{+0.7}_{-0.8}$	$85.0^{+1.0}_{-1.0}$
	$6.34^{+0.15}_{-0.28}$	$2.36^{+0.07}_{-0.07}$	$0.22^{+0.01}_{-0.01}$	$-808.0^{+33.5}_{-58.8}$	$151.5^{+1.7}_{-1.0}$	$85.0^{+1.1}_{-0.8}$
NGC6779	$12.11^{+0.22}_{-0.23}$	$0.92^{+0.10}_{-0.10}$	$0.86^{+0.01}_{-0.01}$	$184.1^{+33.5}_{-33.6}$	$75.5^{+2.0}_{-1.9}$	$138.0^{+3.1}_{-3.1}$
	$12.32^{+0.24}_{-0.29}$	$0.63^{+0.08}_{-0.06}$	$0.90^{+0.01}_{-0.01}$	$125.9^{+33.7}_{-36.8}$	$62.6^{+5.6}_{-5.4}$	$133.5^{+3.0}_{-3.0}$
	$12.11^{+0.14}_{-0.10}$	$0.36^{+0.13}_{-0.10}$	$0.80^{+0.01}_{-0.01}$	$213.3^{+33.1}_{-45.8}$	$56.3^{+6.2}_{-3.8}$	$120.7^{+3.5}_{-4.5}$
NGC6809	$6.06^{+0.08}_{-0.07}$	$1.57^{+0.00}_{-0.00}$	$0.59^{+0.01}_{-0.01}$	$-228.0^{+14.5}_{-17.9}$	$109.8^{+1.6}_{-1.3}$	$79.1^{+0.8}_{-0.6}$
	$5.82^{+0.09}_{-0.11}$	$1.59^{+0.00}_{-0.00}$	$0.57^{+0.01}_{-0.01}$	$-262.5^{+19.5}_{-18.9}$	$115.3^{+1.8}_{-1.9}$	$72.5^{+0.5}_{-0.1}$
	$6.36^{+0.13}_{-0.09}$	$1.08^{+0.14}_{-0.12}$	$0.45^{+0.02}_{-0.01}$	$-324.0^{+3.9}_{-3.0}$	$121.2^{+1.0}_{-1.4}$	$77.2^{+3.9}_{-1.4}$
NGC6838	$7.14^{+0.00}_{-0.00}$	$5.00^{+0.03}_{-0.03}$	$0.18^{+0.01}_{-0.01}$	$-1336.3^{+5.2}_{-5.4}$	$168.1^{+0.3}_{-0.2}$	$111.6^{+0.2}_{-0.2}$
	$7.30^{+0.00}_{-0.00}$	$4.99^{+0.03}_{-0.03}$	$0.19^{+0.01}_{-0.01}$	$-1424.7^{+5.7}_{-5.8}$	$170.2^{+0.2}_{-0.2}$	$110.0^{+0.1}_{-0.5}$
	$7.24^{+0.01}_{-0.01}$	$4.45^{+0.03}_{-0.03}$	$0.23^{+0.01}_{-0.01}$	$-1286.8^{+5.5}_{-6.0}$	$170.9^{+0.2}_{-0.2}$	$106.0^{+2.6}_{-2.6}$
NGC6864	$16.72^{+0.64}_{-0.61}$	$1.49^{+0.23}_{-0.18}$	$0.84^{+0.01}_{-0.02}$	$-313.9^{+84.4}_{-101.6}$	$126.1^{+3.7}_{-5.0}$	$193.6^{+8.2}_{-7.6}$

Continued on next page

Table D.1 – continued from previous page

Name	apocentre [kpc]	pericentre [kpc]	eccentr.	L_z [km/s kpc]	inclin. θ [deg]	T_r [Myr]
	$16.31^{+0.62}_{-0.62}$	$1.13^{+0.22}_{-0.20}$	$0.87^{+0.02}_{-0.02}$	$-221.2^{+92.3}_{-93.8}$	$114.3^{+4.1}_{-5.2}$	$183.5^{+8.0}_{-8.0}$
	$18.05^{+0.32}_{-0.29}$	$0.11^{+0.10}_{-0.06}$	$0.88^{+0.01}_{-0.01}$	$57.0^{+43.5}_{-44.7}$	$78.9^{+8.5}_{-6.7}$	$183.5^{+5.1}_{-9.5}$
NGC6981	$12.96^{+0.39}_{-0.34}$	$6.40^{+0.44}_{-0.39}$	$0.34^{+0.02}_{-0.02}$	$-1231.9^{+75.9}_{-85.3}$	$131.9^{+0.4}_{-0.5}$	$192.1^{+8.2}_{-7.2}$
	$12.94^{+0.35}_{-0.33}$	$5.94^{+0.40}_{-0.33}$	$0.37^{+0.01}_{-0.02}$	$-1211.1^{+69.8}_{-75.1}$	$127.7^{+0.6}_{-0.6}$	$184.5^{+7.5}_{-6.5}$
	$13.37^{+0.47}_{-0.32}$	$4.40^{+0.26}_{-0.24}$	$0.50^{+0.01}_{-0.01}$	$-944.6^{+55.9}_{-62.7}$	$125.7^{+0.8}_{-0.8}$	$175.3^{+7.5}_{-7.5}$
NGC7078	$10.52^{+0.16}_{-0.17}$	$3.84^{+0.14}_{-0.14}$	$0.46^{+0.01}_{-0.01}$	$-1063.8^{+29.3}_{-29.3}$	$150.4^{+0.6}_{-0.6}$	$141.1^{+3.0}_{-2.9}$
	$10.59^{+0.16}_{-0.16}$	$3.69^{+0.13}_{-0.12}$	$0.48^{+0.01}_{-0.01}$	$-1108.7^{+27.2}_{-27.5}$	$143.9^{+0.2}_{-0.2}$	$136.5^{+2.5}_{-3.0}$
	$10.70^{+0.37}_{-0.16}$	$3.05^{+0.06}_{-0.10}$	$0.53^{+0.01}_{-0.01}$	$-944.1^{+37.6}_{-30.2}$	$142.7^{+0.4}_{-0.7}$	$127.5^{+2.6}_{-2.5}$
NGC7089	$18.41^{+0.60}_{-0.48}$	$1.09^{+0.14}_{-0.20}$	$0.89^{+0.02}_{-0.01}$	$184.4^{+57.4}_{-52.6}$	$60.6^{+3.5}_{-2.2}$	$210.1^{+7.3}_{-6.8}$
	$18.55^{+0.59}_{-0.53}$	$0.72^{+0.13}_{-0.09}$	$0.93^{+0.01}_{-0.01}$	$139.2^{+56.2}_{-56.7}$	$69.7^{+3.9}_{-4.5}$	$206.5^{+7.5}_{-7.0}$
	$17.79^{+0.42}_{-1.63}$	$0.17^{+0.12}_{-0.08}$	$0.94^{+0.01}_{-0.01}$	$66.0^{+53.9}_{-42.3}$	$78.8^{+6.9}_{-6.9}$	$176.7^{+3.5}_{-5.2}$
NGC7099	$8.32^{+0.17}_{-0.18}$	$1.83^{+0.01}_{-0.01}$	$0.64^{+0.01}_{-0.01}$	$255.7^{+5.3}_{-7.3}$	$59.0^{+1.5}_{-0.9}$	$104.9^{+1.9}_{-1.8}$
	$8.21^{+0.15}_{-0.15}$	$1.52^{+0.00}_{-0.00}$	$0.69^{+0.01}_{-0.01}$	$239.8^{+7.4}_{-9.5}$	$68.0^{+0.8}_{-0.5}$	$96.5^{+1.5}_{-1.5}$
	$8.28^{+0.16}_{-0.12}$	$1.08^{+0.08}_{-0.10}$	$0.74^{+0.01}_{-0.01}$	$177.8^{+24.8}_{-37.2}$	$73.5^{+3.1}_{-2.9}$	$91.7^{+3.0}_{-1.7}$

Table D.2. Dwarf spheroidal orbital properties. Besides the parameters listed in Table D.1, we also include the angles (θ, ϕ) of the angular momentum vector, and the time elapsed since the last apocentre and pericentre: T_a and T_p respectively. The errors indicate the 16th and 84th percentiles which have been obtained from Monte Carlo realizations sampling the (statistical and systematic) errors in the observables. For each dSph we quote values derived from orbits integrated for 10 Gyr in the Galactic potentials of Models 1, 2 and 3 in the first, second and third row respectively. Since for Model-1 there is a significant fraction of the realizations for which Leo I does not complete one radial oscillation in the 10 Gyr of integration, the values quoted here for this dSph for this model have been derived for an integration time of 100 Gyr.

Name	apocentre [kpc]	pericentre [kpc]	eccentr.	L_z [km/s kpc]	inclin. θ [deg]	ϕ [deg]	T_r [Gyr]	T_a [Gyr]	T_p [Gyr]
Fnx	$172.6^{+114.9}_{-27.3}$	$116.3^{+34.5}_{-50.4}$	$0.27^{+0.19}_{-0.08}$	$8123.6^{+2696.9}_{-2444.9}$	$70.7^{+2.9}_{-2.4}$	$172.9^{+8.7}_{-8.5}$	$3.95^{+2.91}_{-1.23}$	$0.98^{+2.01}_{-0.64}$	$2.97^{+3.44}_{-1.25}$
	$156.4^{+26.9}_{-15.1}$	$85.9^{+47.7}_{-34.4}$	$0.29^{+0.18}_{-0.12}$	$7659.9^{+2586.6}_{-2516.9}$	$70.7^{+2.9}_{-2.6}$	$172.6^{+9.4}_{-9.8}$	$2.65^{+0.77}_{-0.52}$	$0.31^{+0.04}_{-0.60}$	$1.67^{+0.40}_{-0.96}$
	$152.4^{+13.9}_{-11.9}$	$46.0^{+31.6}_{-19.6}$	$0.54^{+0.15}_{-0.18}$	$5610.0^{+2524.4}_{-1818.0}$	$69.5^{+3.4}_{-2.8}$	$168.4^{+11.0}_{-12.4}$	$2.06^{+0.44}_{-0.28}$	$0.16^{+0.08}_{-0.03}$	$1.18^{+0.30}_{-0.17}$
Dra	$90.3^{+7.7}_{-8.2}$	$30.4^{+6.1}_{-5.2}$	$0.49^{+0.05}_{-0.05}$	$-2919.2^{+954.0}_{-1030.3}$	$107.4^{+4.7}_{-5.1}$	$-170.4^{+4.2}_{-4.4}$	$1.38^{+0.18}_{-0.16}$	$0.30^{+0.06}_{-0.05}$	$0.99^{+0.15}_{-0.12}$
	$85.7^{+7.3}_{-6.9}$	$32.0^{+6.1}_{-5.3}$	$0.45^{+0.05}_{-0.05}$	$-2879.5^{+866.1}_{-977.0}$	$106.5^{+4.6}_{-4.2}$	$-170.3^{+4.4}_{-3.9}$	$1.29^{+0.15}_{-0.12}$	$0.18^{+0.04}_{-0.02}$	$0.89^{+0.09}_{-0.11}$
	$86.2^{+7.0}_{-6.2}$	$26.6^{+4.5}_{-3.5}$	$0.53^{+0.04}_{-0.04}$	$-2433.7^{+722.1}_{-912.5}$	$104.9^{+4.6}_{-3.8}$	$-172.3^{+4.1}_{-3.0}$	$1.17^{+0.11}_{-0.10}$	$0.22^{+0.03}_{-0.02}$	$0.80^{+0.08}_{-0.07}$
Car	$107.5^{+19.4}_{-6.7}$	$87.0^{+23.0}_{-24.8}$	$0.14^{+0.11}_{-0.10}$	$-2537.8^{+1837.6}_{-1882.9}$	$98.0^{+6.0}_{-5.9}$	$-162.1^{+2.6}_{-2.5}$	$2.39^{+0.68}_{-0.42}$	$0.05^{+1.55}_{-0.03}$	$1.21^{+1.64}_{-0.24}$
	$106.7^{+7.8}_{-6.3}$	$74.5^{+23.7}_{-19.5}$	$0.18^{+0.12}_{-0.10}$	$-2663.3^{+1725.2}_{-1851.0}$	$98.7^{+5.8}_{-5.8}$	$-161.5^{+2.8}_{-2.6}$	$1.96^{+0.30}_{-0.27}$	$0.08^{+0.01}_{-0.17}$	$1.06^{+0.16}_{-0.29}$
	$106.4^{+6.2}_{-6.1}$	$46.0^{+13.2}_{-11.2}$	$0.40^{+0.10}_{-0.10}$	$-2426.0^{+1538.0}_{-1451.5}$	$99.4^{+6.1}_{-5.8}$	$-161.7^{+2.8}_{-2.4}$	$1.55^{+0.19}_{-0.14}$	$1.54^{+0.19}_{-0.14}$	$0.76^{+0.09}_{-0.07}$
UMi	$88.0^{+3.7}_{-3.9}$	$33.5^{+5.6}_{-4.9}$	$0.45^{+0.05}_{-0.06}$	$-786.2^{+708.9}_{-749.9}$	$94.4^{+4.0}_{-4.0}$	$161.3^{+4.0}_{-3.7}$	$1.39^{+0.11}_{-0.09}$	$0.26^{+0.04}_{-0.03}$	$0.96^{+0.10}_{-0.08}$
	$85.3^{+3.1}_{-3.1}$	$36.1^{+5.2}_{-5.1}$	$0.40^{+0.06}_{-0.05}$	$-1008.4^{+690.8}_{-698.2}$	$95.3^{+3.7}_{-3.7}$	$162.3^{+3.9}_{-3.9}$	$1.32^{+0.08}_{-0.09}$	$0.19^{+0.01}_{-0.02}$	$0.88^{+0.07}_{-0.07}$
	$85.6^{+3.8}_{-2.9}$	$30.5^{+3.9}_{-3.8}$	$0.47^{+0.05}_{-0.04}$	$-1314.4^{+574.2}_{-583.4}$	$97.2^{+3.4}_{-3.2}$	$164.2^{+3.6}_{-3.1}$	$1.19^{+0.06}_{-0.06}$	$0.20^{+0.02}_{-0.02}$	$0.80^{+0.05}_{-0.04}$
Sext	$224.3^{+79.5}_{-51.5}$	$79.6^{+5.0}_{-5.3}$	$0.48^{+0.09}_{-0.09}$	$-16800.2^{+1592.0}_{-1720.0}$	$139.4^{+0.1}_{-0.3}$	$124.8^{+6.2}_{-6.8}$	$4.29^{+1.58}_{-0.99}$	$2.34^{+0.77}_{-0.44}$	$0.20^{+0.05}_{-0.04}$
	$164.8^{+30.8}_{-24.6}$	$80.1^{+4.6}_{-4.8}$	$0.35^{+0.05}_{-0.05}$	$-17094.0^{+1565.6}_{-1627.7}$	$139.3^{+0.1}_{-0.3}$	$126.8^{+6.2}_{-6.4}$	$2.67^{+0.43}_{-0.34}$	$1.54^{+0.19}_{-0.21}$	$0.18^{+0.02}_{-0.10}$
	$120.5^{+13.6}_{-10.3}$	$70.0^{+6.2}_{-6.4}$	$0.27^{+0.01}_{-0.00}$	$-14938.4^{+1333.5}_{-1492.2}$	$139.0^{+0.3}_{-0.7}$	$133.0^{+6.8}_{-6.5}$	$1.94^{+0.21}_{-0.17}$	$1.31^{+0.08}_{-0.06}$	$0.34^{+0.05}_{-0.05}$
Leo I	$820.0^{+920.3}_{-243.4}$	$89.5^{+55.9}_{-47.5}$	$0.83^{+0.07}_{-0.03}$	$-16313.6^{+12245.8}_{-10347.6}$	$125.9^{+5.4}_{-23.4}$	$138.4^{+55.9}_{-48.5}$	$18.35^{+28.13}_{-7.19}$	$10.30^{+13.83}_{-3.69}$	$1.01^{+0.08}_{-0.11}$
	$429.0^{+126.1}_{-60.6}$	$112.6^{+58.4}_{-60.6}$	$0.61^{+0.16}_{-0.05}$	$-21186.6^{+13321.0}_{-12256.5}$	$126.5^{+4.9}_{-15.7}$	$136.7^{+47.2}_{-50.2}$	$5.04^{+0.63}_{-0.54}$	$4.01^{+0.70}_{-1.10}$	$0.92^{+0.16}_{-0.08}$
	$388.0^{+86.9}_{-37.0}$	$86.9^{+59.2}_{-44.4}$	$0.63^{+0.16}_{-0.10}$	$-18831.8^{+9856.3}_{-11928.2}$	$127.0^{+4.5}_{-11.0}$	$140.4^{+46.0}_{-43.3}$	$4.92^{+1.34}_{-0.71}$	$3.43^{+0.67}_{-0.40}$	$0.91^{+0.06}_{-0.09}$
Leo II	$240.5^{+20.2}_{-14.5}$	$68.9^{+115.9}_{-42.5}$	$0.56^{+0.24}_{-0.33}$	$2055.2^{+7219.4}_{-6753.6}$	$82.3^{+25.3}_{-14.6}$	$-128.9^{+80.9}_{-152.5}$	$4.38^{+2.21}_{-0.73}$	$4.13^{+1.35}_{-0.68}$	$1.82^{+0.42}_{-0.29}$
	$236.4^{+14.9}_{-14.0}$	$60.1^{+75.7}_{-36.8}$	$0.60^{+0.22}_{-0.32}$	$972.6^{+6352.4}_{-6214.4}$	$86.9^{+19.9}_{-16.5}$	$-143.2^{+68.9}_{-160.3}$	$3.28^{+0.76}_{-0.34}$	$3.21^{+0.37}_{-0.57}$	$1.51^{+0.17}_{-0.25}$
	$237.7^{+15.3}_{-12.5}$	$45.8^{+48.4}_{-26.9}$	$0.68^{+0.17}_{-0.24}$	$-280.3^{+5319.4}_{-4976.1}$	$91.2^{+17.1}_{-19.5}$	$-91.7^{+171.3}_{-59.0}$	$3.01^{+0.45}_{-0.29}$	$2.90^{+0.40}_{-0.28}$	$1.39^{+0.18}_{-0.13}$
Sgr	$44.5^{+13.3}_{-10.4}$	$14.8^{+2.1}_{-2.3}$	$0.50^{+0.05}_{-0.04}$	$-927.1^{+437.9}_{-472.7}$	$100.6^{+3.1}_{-3.8}$	$90.9^{+0.9}_{-1.0}$	$0.62^{+0.18}_{-0.14}$	$0.35^{+0.09}_{-0.07}$	$0.04^{+0.00}_{-0.00}$
	$42.6^{+14.0}_{-9.7}$	$14.3^{+2.3}_{-2.3}$	$0.50^{+0.05}_{-0.03}$	$-748.7^{+399.4}_{-469.1}$	$98.8^{+3.3}_{-4.1}$	$91.6^{+1.1}_{-2.0}$	$0.61^{+0.18}_{-0.14}$	$0.34^{+0.07}_{-0.09}$	$0.05^{+0.01}_{-0.00}$
	$32.3^{+6.5}_{-5.0}$	$12.3^{+2.1}_{-2.0}$	$0.45^{+0.01}_{-0.01}$	$-222.5^{+290.1}_{-364.5}$	$93.0^{+3.6}_{-4.1}$	$84.9^{+2.1}_{-4.8}$	$0.45^{+0.09}_{-0.07}$	$0.28^{+0.05}_{-0.04}$	$0.06^{+0.00}_{-0.01}$
Scl	$111.8^{+12.4}_{-9.1}$	$59.7^{+7.7}_{-6.7}$	$0.30^{+0.03}_{-0.01}$	$-713.6^{+188.9}_{-174.0}$	$92.6^{+0.7}_{-0.7}$	$8.1^{+5.3}_{-4.5}$	$2.07^{+0.31}_{-0.21}$	$1.47^{+0.14}_{-0.12}$	$0.43^{+0.06}_{-0.06}$
	$107.1^{+8.4}_{-7.3}$	$61.7^{+6.4}_{-6.2}$	$0.27^{+0.03}_{-0.01}$	$-787.4^{+190.5}_{-173.5}$	$92.8^{+0.7}_{-0.7}$	$7.8^{+4.8}_{-4.1}$	$1.82^{+0.16}_{-0.14}$	$1.31^{+0.13}_{-0.14}$	$0.41^{+0.06}_{-0.05}$
	$100.9^{+6.5}_{-6.8}$	$54.4^{+6.1}_{-4.8}$	$0.29^{+0.04}_{-0.03}$	$-675.1^{+167.8}_{-150.6}$	$92.4^{+0.7}_{-0.6}$	$7.4^{+3.7}_{-3.8}$	$1.57^{+0.12}_{-0.11}$	$1.23^{+0.08}_{-0.09}$	$0.44^{+0.04}_{-0.04}$
Boo I	$78.2^{+7.1}_{-6.3}$	$31.7^{+7.1}_{-6.4}$	$0.42^{+0.06}_{-0.05}$	$-1334.0^{+372.0}_{-405.2}$	$97.9^{+1.3}_{-1.6}$	$-50.4^{+6.6}_{-7.6}$	$1.23^{+0.18}_{-0.16}$	$0.92^{+0.09}_{-0.09}$	$0.30^{+0.01}_{-0.01}$
	$75.2^{+5.9}_{-5.1}$	$30.1^{+7.5}_{-5.8}$	$0.43^{+0.06}_{-0.06}$	$-1177.7^{+357.3}_{-420.6}$	$97.3^{+1.4}_{-1.7}$	$-52.2^{+7.1}_{-8.1}$	$1.14^{+0.15}_{-0.11}$	$0.88^{+0.09}_{-0.09}$	$0.30^{+0.01}_{-0.01}$
	$71.6^{+3.9}_{-3.9}$	$19.8^{+4.0}_{-3.8}$	$0.57^{+0.05}_{-0.05}$	$-635.7^{+273.1}_{-351.1}$	$95.0^{+2.0}_{-1.9}$	$-65.1^{+9.2}_{-8.3}$	$0.94^{+0.08}_{-0.06}$	$0.76^{+0.06}_{-0.05}$	$0.29^{+0.02}_{-0.02}$

source_id	ra	dec	G (phot_g_mean_mag)
4689633627542489728	6.77396	-71.99619	19.378
4689634074221208320	6.48790	-72.01599	17.090
4689638128697225216	5.61038	-72.13231	19.695
4689637514491268480	5.75409	-72.11833	17.506

Table D.3. Example of part of a list of possible cluster members. Here we list the first four entries of the compilation of members of the globular cluster NGC 104. The full table for this cluster is available in electronic format, along with separate tables for each of the rest of the globular clusters in our sample, each of the 9 dSph, the Bootes I UFD, the LMC and SMC. The stars in these lists have been selected and used to determine the astrometric parameters of the corresponding objects following either the procedures described in Sec. 2.1 (for the clusters and dwarfs) or in Sec. 2.2 (for the LMC and SMC).